# MATERIAL AND ELECTROCHEMICAL PROPERTIES OF WROUGHT AND ADDITIVELY MANUFACTURED ALUMINUM ALLOYS- EFFECTS OF SURFACE PRETREATMENT AND SURFACE FINISHING

By

Jack Walton

A DISSERTATION

Submitted to
Michigan State University
in partial fulfillment of the requirements
for the degree of

Chemistry – Doctor of Philosophy

2023

# ABSTRACT

The overall objective of this dissertation is to i) illustrate the effectiveness of commercial TCP conversion coatings on wrought aluminum alloy and ii) apply commonly used surface treatments to an additively manufactured aluminum alloy. First, two TCP coatings are studied on wrought aluminum alloy AA2024-T3. One of the TCP coatings is pretreated by a degrease step followed by deoxidation before applying the coating. The other TCP coating involves a simplified pretreatment which does not require the deoxidation step. The formation and structure of the conversion coatings are compared using analytical techniques. Then, the corrosion behavior was evaluated using electrochemical methods and accelerated degradation testing. A second aim of the research was to investigate the material properties and electrochemical behavior of aluminum alloy, $AlSi_{10}Mg$, prepared by additive manufacturing using selective laser melting (SLM). Two studies of corrosion protective coatings on SLM $AlSi_{10}Mg$ are presented: i) the TCP conversion coating and ii) Type II (sulfuric acid) anodization.

# ACKNOWLEDGEMENTS

I could not have walked this path alone. Thank you, Dr. Romana, Dr. Sarah, Dr. Shruthi, Dr. Kirti, and former colleagues of the Swain group. You welcomed me as an undergraduate student and encouraged me to pursue my research at a higher level. Your dedication and kindness were an inspiration to me. You showed me what it takes to achieve such high goals and helped me realize that potential within myself as a growing scientist. I want you to know that I see you all as strong role models and good friends. I am proud to know you.

Thank you to Isuri, Shashika, Aaron, Maral, Rosemary, and all others in the Swain group during my graduate studies. Speaking with you helped me both professionally and personally. I am always happy to learn about your fascinating science efforts and share perspectives on all aspects of life as a student researcher. I see you all reaching higher, going farther, and getting closer to achieving your goals. I count myself lucky every day that I see you. You are honing your skills and persevering in your own unique life circumstances. I wish the best for you all.

Dr. Swain, your presence as a mentor and P.I. are what forged me into the scientist I am today. I want to share something that you said some years ago that has greatly impacted me. One day in a group meeting you advised your students that research should be done "efficiently, effectively, and strategically". Those words resonate with me to this day, and it has helped me stay focused and accomplish the goals of my research. My research would not be possible without your support in securing grants and including me as a research assistant. Those projects gave me invaluable experience as a researcher and gave me the time and financial security to complete my studies.

Thank you to my committee members and professors in Chemistry and CHEMS for your constructive criticism and mentorship, including Dr. Proshlyakov, Dr. Hamann, Dr. Boehlert, and

Dr. Barton. Thank you to the chemistry department and those who I served as a teaching assistant, Dr. Severin, Dr. Blanchard, Dr. Shriner, and Dr. Miller. Your classes broadened my knowledge of analytical chemistry and introduced me to the labor and joy of brewing.

Thank you to my family. Mom, I feel your love and care every time I call or text and whenever you tell me to be careful, and sharing meals together when we meet up. When I was younger, I remember watching you teach and attending Highland dance competitions with you. You lead me by example in those moments, and I believe that your character has helped me achieve where I am today. Dad, at your core you are a helper and a doer. I see you work hard to plan and act in service to others. Thank you for reaching out to me throughout my degree and working to meet up when we can. Cal, I am beyond proud of you. I am glad that I got to be a roommate with you for some of our time at MSU. Thank you to my grandparents and extended family. I can finally tell you that I have finished my degree, thank you for asking.

To my friends I met in grad school that now live in every corner of the country, Eric, Ben, Cash, Hailey, and Lizzie and Dom, thank you for staying in touch with me all these years. As busy and disarrayed our schedules are, we still find a way to come together. The time I get to spend with you is a relief and respite from our daily life. I pray that the Dice God have mercy on Nylian, Grantok, Moonie, Balasar, and Trolo. To those we outlived, Aman, Strakk, and Morr, may you rest in peace. Thistle, I hope you find your way home.

Finally, thank you to Robin, my love, my partner, and my best friend. You have seen it all-the stress, the mess, the tests, and success. I am so blessed to have you by my side. You helped me in countless ways and together we made it all the way to the end. You are forever my inspiration, and I am grateful for your time with me. I love you.

# TABLE OF CONTENTS

# CHAPTER 1 - Introduction

## 1.1 Corrosion

Corrosion is a thermodynamically favored process in which metals degrade into more stable metal oxides or soluble metal ions. Metals in cars, bridges, ships, and airplanes are all susceptible to corrosion. One study estimated that corrosion costs the United States $276 billion annually.[1] Transportation, infrastructure, and national defense account for over half of this amount. If corrosion issues are left unaddressed, corrosion will lead to shortened component serviceability and dangerous mechanical failure.[2] Fundamentally, corrosion is an electrochemical process where the oxidation reaction is the dissolution of a solid metal to produce metal ions and electrons. For corrosion to occur there must be 1) electrolyte/electronic pathway, 2) dissolved oxygen or some other reducible species, and 3) a potential gradient to drive the process forward.[3]

Aluminum and aluminum alloys are widely used throughout the automotive and aerospace industries due to their high strength and low density. Consider the corrosion of aluminum in an aqueous solution. The oxidation half-cell reaction of aluminum is shown in Eq. 1, where the metal loses three electrons and becomes a metal cation. The free electrons must be consumed by a reduction, or proton-consuming, reaction. In the case of a naturally aerated aqueous electrolyte, the primary reaction is the reduction of dissolved $O_2$. Depending on the pH, two possible reduction reactions are shown in Eq. 2 and Eq. 3.

$$\mathrm{Al} \rightarrow Al^{3+} + 3\mathrm{e}^- \tag{1}$$

$$\mathrm{O_2} + 4\mathrm{H}^+ + 4\mathrm{e}^- \rightarrow 2\mathrm{H_2O}\ \text{(acid)} \tag{2}$$

$$O_2 + 2H_2O + 4e^- \rightarrow 4OH^-\text{(neutral or alkaline)} \tag{3}$$

Corrosion can take several forms and take place through different mechanisms. A few examples are depicted in Figure 1.1.

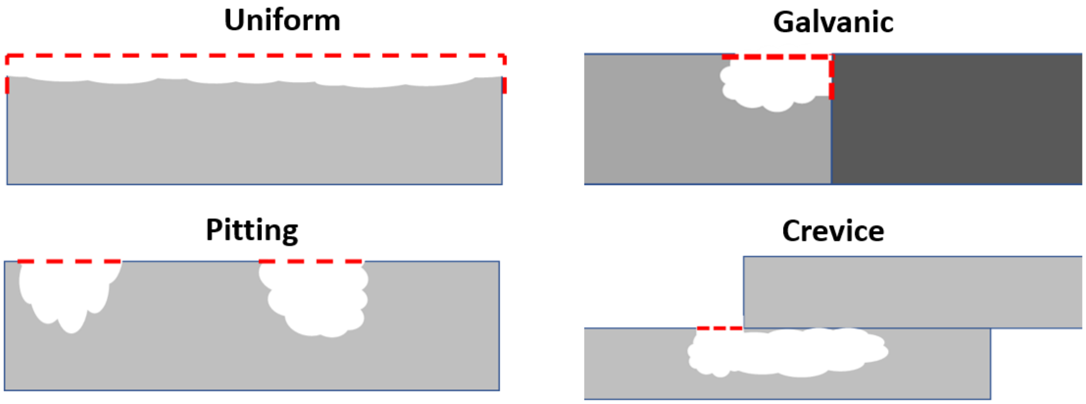

**Figure 1.1.** Cartoon of various forms of corrosion damage.

Uniform corrosion occurs when a metal is subjected to an aggressive environment such as a highly acidic or basic pH. In such conditions, both the passive oxide layer and underlying metal will readily dissolve.[4] This leads to a steady loss of material over the entire exposed area. Uniform corrosion is avoidable by selecting materials that will not corrode in the operating conditions. On the other hand, uniform corrosion can be used in a controlled manner to strip the surface of the metal. Surface pretreatments such as acid pickling and alkaline etching are founded on the principles of uniform corrosion. Typically, the metal is exposed for a short time to produce a clean, homogeneous surface. The cleaned part is ideal for additional surface treatments and finishing.

Aluminum is a very active metal and will quickly develop a thin (≈10 nm) aluminum oxide ($Al_2O_3$) layer. Because of this, aluminum is moderately protected by its natural passive film. Localized corrosion mechanisms such as galvanic corrosion, pitting corrosion, and crevice corrosion occur at specific sites on the metal surface. Unlike uniform corrosion, most of the metal surface is passivated, or protected from oxidation. Localized corrosion can occur at certain contact points and microstructural features. For example, consider an aluminum plate fastened to a carbon fiber reinforced composite. In this case, the aluminum alloy is galvanically "active" and carbon composite is more "noble". The galvanic difference between the materials creates a potential driving force for oxidation.[5] The carbon composite metal acts as the cathode, which supports the reduction reaction. In hand, the aluminum corrodes near the contact point of the two materials.[6] This is known as galvanic corrosion.

Pitting corrosion occurs when the passive oxide layer breaks down in a discrete area. This is commonly studied on aluminum alloys when subjected to a chloride ion-containing electrolyte. The negative chloride ions are attracted to the positively charged aluminum oxide. The interaction between the oxide and chloride ion can oxidize the underlying Al metal to $Al^{3+}$.[7] The oxide layer breaks down and exposes the highly reactive Al metal. The exposed metal is oxidized by two pathways, 1) Al dissolution (pit growth) and 2) Al oxide formation (repassivation). In essence, pit growth and repassivation act in opposition; When pit growth out-competes repassivation, localized corrosion will continue as stable pit growth. Otherwise, the surface is covered by a newly formed aluminum oxide layer and is repassivated. The pit size is dependent on several conditions (temperature, concentration of $Cl^{-}$ and $O_2$, local pH, etc.), and can range from < 1 μm to over 100 μm in depth and diameter. Unseen damage and microscopic weakening of materials are two major dangers of pitting corrosion. Monitoring corrosion at this scale is a practical challenge because of the small size.

Crevice corrosion can arise when an electrolyte leeches into a small gap and becomes trapped. Mechanically fabricated metal hem joints (i.e. the edges of an automobile door panel) are vulnerable to crevice corrosion. This is particularly an issue for cars driving in the winter when the joint is exposed to road salt and moisture. The trapped electrolyte can corrode the metal even dissolved $O_2$ is not available inside. The local pH can be acidified by the hydrolysis of metal ions while $O_2$ reduction occurs outside of the crevice. The degradation of mechanical joints by crevice corrosion is a major issue for industry, and protection against this corrosion is a key area of research.

Corrosion will always be a factor for scientists and engineers. By its nature, corrosion degrades the resilience and reliability of structures, machines, and tools. With the conscious use of materials, time, and energy, it is imperative to seek ways to protect the metal against corrosion. Learning and understanding the science of corrosion will guide the development of new materials and solutions to prevent their deterioration.

## 1.2 Aluminum Alloys

Aluminum has a relatively low density (2.7 g/cm$^3$) compared to that of iron (7.9 g/cm$^3$). To improve the overall strength, other metals are added to the aluminum in a process called alloying. Aluminum alloys contain small percentages of other metals including copper, manganese, magnesium, and zinc. Different compositions and combinations of metals will yield different material properties (e.g. hardness, toughness, ductility, density). As such there is a wide variety of aluminum alloys that are used for several different applications.

One alloy of interest is AA2024-T3, which is commonly used in airplane wings and fuselages.[8] 2XXX series (Al-Cu based) alloys are used for their high strength-to-weight ratio and good fatigue resistance. However, because of the galvanic difference between aluminum and copper, the alloy is prone to corrosion. Figure 1.2 shows a cartoon of corrosion on AA2024. Microscopic particles rich in Cu are present throughout the alloy. The contact between the Al matrix and Cu-rich particle creates a galvanic couple, where the Al is more active. The Al is oxidized to $Al^{3+}$ and the electrons are consumed by reduction reactions at the cathodic site (Cu-rich particle). Galvanic coupling at the microscopic scale is a well-known issue for AA2024.[9 – 11] Preventing corrosion on AA2024 is a widely-studied topic and will be discussed in greater depth later on.

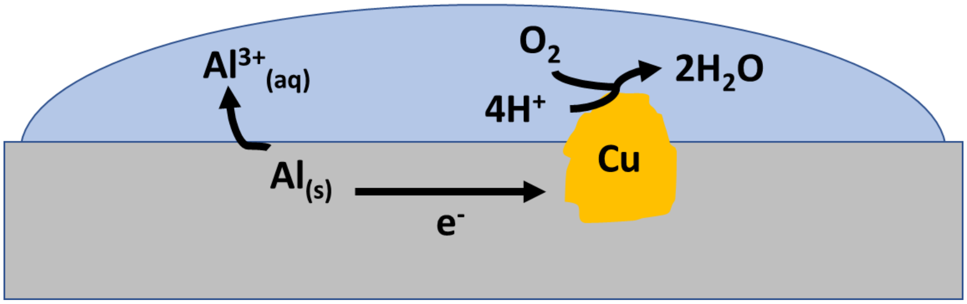

**Figure 1.2.** Corrosion of Al near a Cu-rich particle.

## 1.3 Wrought and Selective Laser Melted Aluminum Fabrication

Wrought aluminum alloys are formed by mechanically working the metal into a desired shape through extrusion, rolling, and forging. The 2XXX series alloys are desirable for wrought processing because they are easily worked into shape. The part can be subsequently hardened by heat treatment, or precipitation hardening.[12] The machining of Al-Cu alloys has been used for several decades and has become a reliable and universal process.

While the creation and machining of wrought aluminum alloys is industrially standardized, new methods of aluminum manufacturing are a key topic for research and development. New technologies can improve the efficiency and ease of fabrication, reduce waste, and increase process control. At the forefront of the next generation of fabrication is a process called metal additive manufacturing (MAM).[13] In essence, MAM fabrication creates metal parts through building from the ground-up, rather than sculpting a piece by machining (wrought) and milling (subtractive manufacturing). In other words, the part is 3D-printed into the desired shape without the need for additional downstream machining. MAM is composed of several different 3D printing techniques. Selective laser melting (SLM) of aluminum[14] will be discussed in the focus of this work. The SLM process involves melting and fusing metallic powder particles together with a high-power laser beam scanned across the build surface, depicted in Figure 1.3**.** Once a layer of solid metal is created, the tray holding the specimen is lowered and powder is layered over the top. This is followed by the laser-assisted melting and fusing of the particles to form the new layer.

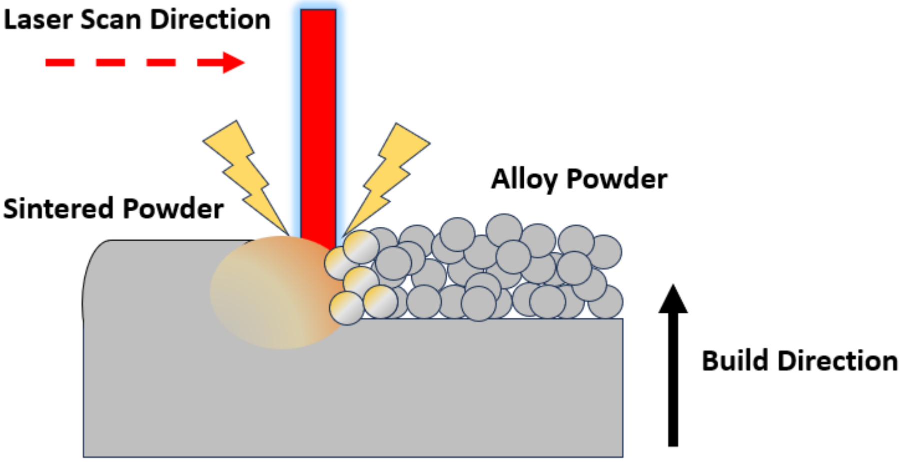

**Figure 1.3.** Cartoon of selective laser melting fabrication.

## 1.4 Corrosion Protection

Whether the metal is formed through a historically reliable method or at the forefront of the next generation of fabrication techniques, corrosion protection is a key factor for a long-lasting material. Coating systems are ubiquitous in corrosion inhibition technologies. Paints and other coatings are used across automotive, aerospace, and marine applications. Coating the metal with multiple layers of primers and paints blocks electrolyte from interacting with the metal surface, which prevents corrosion initiation.

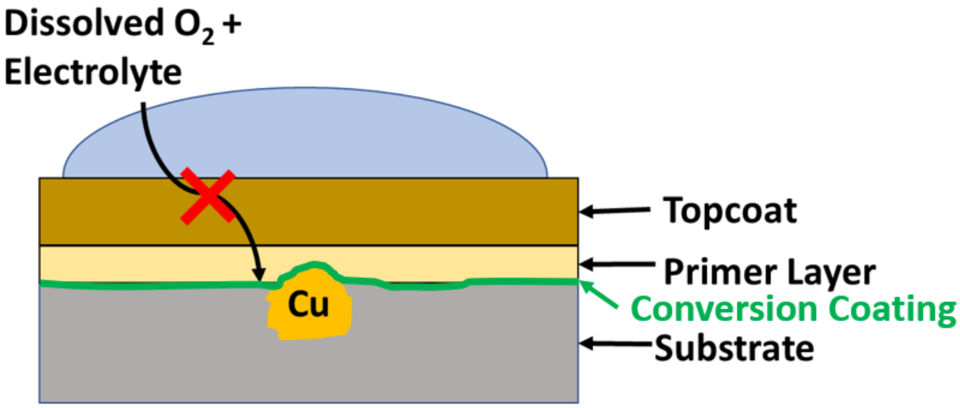

**Figure 1.4.** Diagram of a multilayer coating system used on an Al-Cu alloy for corrosion mitigation.

The conversion coating is the first layer a multilayer coating system. This layer is applied to the substrate surface before the primer layer and are typically less than 100 nm thick.[15] The conversion coating should improve the corrosion resistance of the metal and promote adhesion to the primer layer and any additional paint coats. Adhesion of the primer layer is very important in the function of the coating system. If adhesion is not promoted by the conversion coating, the subsequent layers could delaminate, and expose the underlying metal. It is equally important is the corrosion protection afforded by the conversion coating. Ideally this layer is continuous over the surface, impervious, inert, and bond readily to the substrate.[16]

Historically, the best corrosion inhibiting conversion coatings were made with hexavalent chromium, called chromate conversion coatings, which is a known carcinogen. Environmental toxicity and governmental regulations of hexavalent chromium have driven efforts to develop non-chromate replacement.[7] One of the leading replacements is a trivalent chromium-based conversion coating, called a trivalent chromium process (TCP) coating. Presently, there are multiple commercial TCP products available, each with slightly different proprietary formulations. The bath will generally contain $ZrF_6^{2-}$, $Cr^{3+}$, and $SO_4^{2-}$ and have an acidic pH (3.8-4.0). Specimens are immersed in the bath and the coating deposits onto the surface.

First, the aluminum oxide layer is dissolved, and the surface is activated by the formation of fluoroaluminate species, shown in Eq. 4 and Eq. 5.

$$Al_2O_3 + 2xF^- + 6H^+ \rightarrow 2AlF_x^{(3-x)} + 3H_2O \qquad (4)$$

$$Al^{3+} + 3F^- \rightarrow AlF_{3(s)} \qquad (5)$$

At the Al interface, the local pH increases due to proton consumption (Eq. 4) and hydroxide production (Eq. 6).

$$2Al_{(s)} + 6H_2O \rightarrow 2Al^{3+} + 6OH^- + 3H_2 \qquad (6)$$

This gradient leads to the precipitation of zirconium and chromium oxides and hydroxides (Eq. 7 and Eq. 8, respectively).

$$ZrF_6^{2-} + 4OH^- \rightarrow ZrO_2 \cdot nH_2O + 6F^- \qquad (7)$$

$$Cr^{3+} + 3OH^- \rightarrow Cr(OH)_3 \qquad (8)$$

The dissolution of the passive film and initial nucleation of metal oxides and hydroxides are both rapid steps, both occurring in the first 60 seconds of coating bath immersion. The substrate is typically immersed for 5-10 minutes to produce a fully formed conversion coating with a thickness on the order of dozens of nanometers. A cartoon of the process is shown below in Figure 1.5. The coating has an inner and outer layer, with the inner layer formed by the fluoride attack on the thin passive film.[17-21] Further away from the substrate surface, the fluoride concentration is minimal and is dominated by the chromium and zirconium oxides.

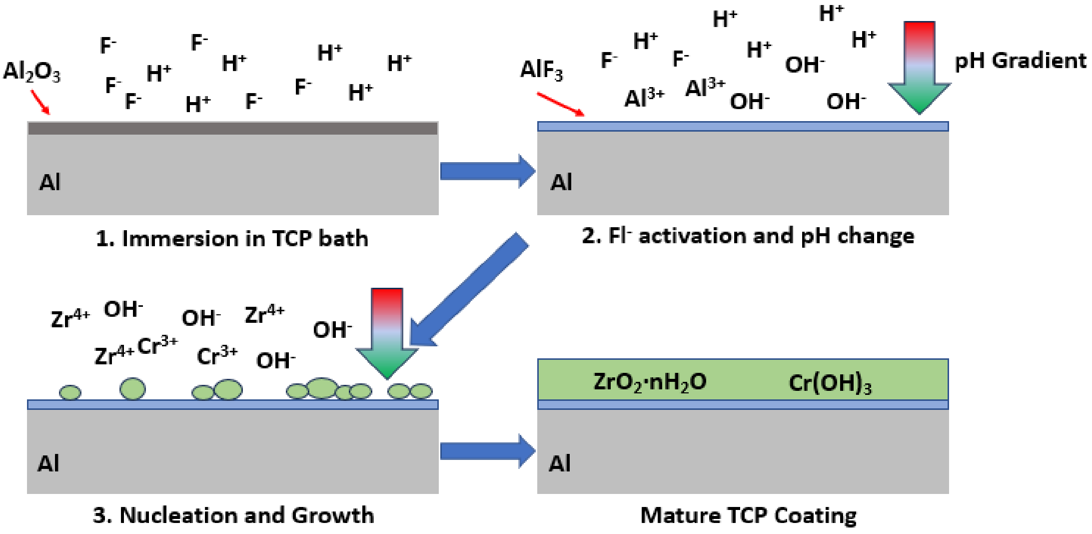

**Figure 1.5.** Steps in the formation of TCP conversion coating on aluminum during immersion**.**

A properly formed TCP coating will passivate the bulk surface of the metal. Dissolved oxygen and electrolyte are blocked from interacting with the metal substrate (See Figure 1.4). The cathodic reaction ($O_2$ reduction) is inhibited. In turn, the anodic reaction (aluminum oxidation) cannot occur, and corrosion is successfully mitigated. The coating, however, contains intrinsic defects; hydrated channels tunnel through the TCP layer to the substrate.[22] These pores account for a very small area of the surface but allow for electrochemically active species to reach the surface. Pitting corrosion can occur in these areas, and then spread outward as the pit grows. Pits on TCP coated specimens can grow to cover hundreds of microns in diameter and burrow dozens of microns into the surface.[23]

## 1.5 Aluminum Anodizing

Another method to protect the metal from corrosion is called anodizing. Anodizing is a process that electrochemically oxidizes the metal in a solution of acid to grow a thick layer of $Al_2O_3$ on the surface. An anodized surface will have superior corrosion protection and improved wear resistance.[24] The formation of the oxide layer depends on the anodizing voltage or current density, acid, and operating temperature. For this work an acid bath of $H_2SO_4$ (Type II) at room temperature will be demonstrated. The structure of the anodized coating is depicted in Figure 1.6.

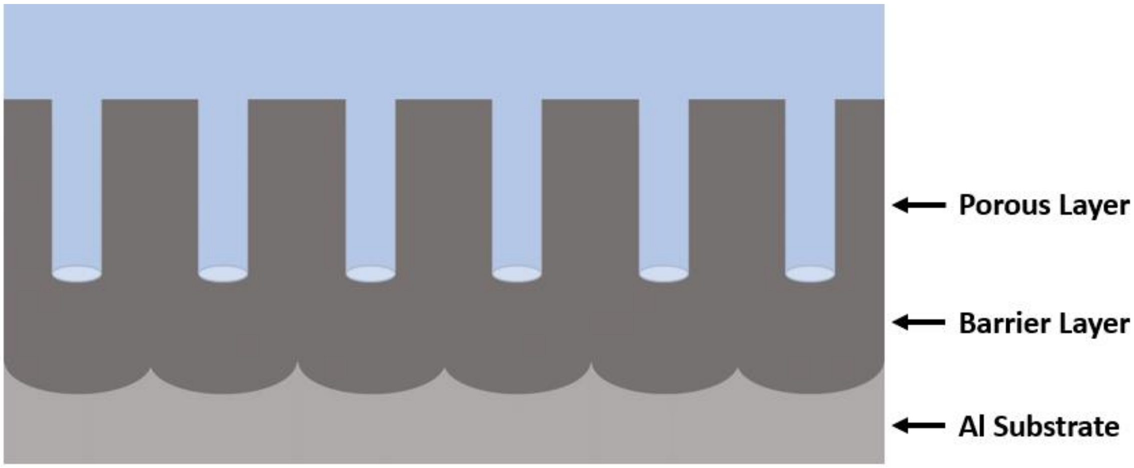

**Figure 1.6.** Morphological structure of an anodic coating formed on aluminum by electrochemical anodization.

The oxide has two sections: a very thin barrier layer and a porous outer layer. The barrier layer is a densely packed aluminum oxide of about 10 nm in thickness.[25] The anodizing voltage affects the thickness of the barrier layer. Atop the barrier layer is the porous layer. The porous layer is thicker than the barrier layer and measured on the scale of $> 1$ μm. The thickness of the porous layer is dependent on the anodizing time.[26] A desirable coating thickness is about 5 μm, or a coating weight of at least 1000 mg/ft$^2$. In practice, after anodizing, the oxide layer is "sealed" by a chemical soak, or hot water bath.[27] This closes off the pores and blocks electrolyte from accessing the barrier layer and the underlying metal.

## 1.6 Surface Preparation

Ideally, conversion coatings must have good adhesion to the substrate and no defects. In practice, however, conversion coatings will have defects and other non-homogeneities that allow electrolyte, chloride, and reducible species to interact with the metal surface. These defects can cause the coating system to fail. The underlying metal would be exposed to electrolyte and oxygen and any the coating system would be rendered useless. This is the importance of surface pretreatment: the surface of the metal must be reliably prepared for the best possible coverage of the conversion coating. Ultimately, surface pretreatment will minimize the defects and non-homogeneities on the metal surface. To achieve this, the metal should be morphologically and chemically uniform.

During storage and handling, the metal surface will accumulate small amounts of soil and grease. These contaminants can block the conversion coating from contacting the surface and the coating will not form properly. To remove these contaminants, the first pretreatment step of use is called “degreasing”. Degreasing the surface removes organic contaminants and soil. The metal surface may also have oxidized in some areas. The buildup of corrosion product, so-called “smut”, is typically non-homogeneous and can inhibit coating formation. For the next pretreatment, the metal is “deoxidized”, or de-smutted. Deoxidizing is typically done in a highly acidic pH, also referred to as “pickling”. The deoxidation dissolves the corrosion product and metal surface alike, so it is important to understand the effects of the pretreatment on the surface to choose the optimal working conditions to minimize the damage to the surface. The process parameters and pretreatment compositions are all dependent on the alloy and its intended application. For this work, the pretreatment steps are a non-etching alkaline degrease followed by an acidic deoxidation before conversion coating or anodizing.

## 1.7 Motivation for Work

At present, the corrosion behavior of wrought AA2024 is well understood. While the alloy possesses useful material properties for manufacturing and engineering purposes, Cu-rich particles make the alloy more susceptible to corrosion. Solutions to the corrosion problem include (i) anodic protection – slowing the kinetics of the aluminum oxidation reaction, (ii) cathodic protection – slowing the kinetics of the cathodic (generally oxygen reduction) reaction and (iii) slowing both the anodic and cathodic reaction rates. Coating systems provide corrosion mitigation by one or more of these mechanisms. Coating systems can serve as a barrier layer to the environment thereby reducing both the rates of the anodic and cathodic reaction. To achieve good corrosion resistance, the coating system must form uniformly on a surface and consist of few defects. Optimally formed coating systems require proper alloy surface pretreatment to prepare the alloy for coating formation. Wet chemical pretreatment and environmentally friendly conversion coating systems for AA2024, and other aluminum alloys, is an important area of current research. One of aim of this research was to study and understand the formation, chemical composition, and electrochemical corrosion resistance of a new trivalent chromium process (TCP) conversion coating that requires a simplified surface pretreatment process. The TCP coating was investigated standalone when formed by immersion on AA2024 and when used as a sealant for the same alloy anodized in sulfuric acid.

A second aim of the research was to investigate the material properties and electrochemical behavior of aluminum alloy, $AlSi_{10}Mg$, prepared by additive manufacturing using selective laser melting (SLM). Metal 3D printing is a metal alloy fabrication process that is attracting great interest because of the bottom-up fabrication and reduced material waste. Research was conducted to learn about the material microstructure, chemistry, mechanical properties (hardness) and electrochemical corrosion resistance. SLM $AlSi_{10}Mg$ alloy was used to study the effect of two surface treatments: (i) coating with a TCP conversion coating and (ii) sulfuric acid anodization.

# REFERENCES

1. G.H. Koch, M.P.H. Brongers, N.G. Thompson, Y.P. Virmany, and J.H. Payer, Corrosion Cost and Prevenntive Strategies in the United States, *Federal Highway Administration*, Report No. FHWA-RD-01-156, (2002).

2. El-Meligi, A. A., *Recent Pat. Corro. Sci.*, **2**, 22–33, (2010).

3. Harb, J. N., *Electrochemical Engineering*, Wiley, Hoboken, NJ, (2018).

4. Huang, I.-W.; Hurley, B. L.; Yang, F.; Buchheit, R. G, Dependence on Temperature, pH, and $Cl^-$ in the Uniform Corrosion of Aluminum Alloys 2024-T3, 6061-T6, and 7075-T6, *Electrochim. Acta*, **199**, 242–253, (2016).

5. S. Li, H.A. Khan, L.H. Hihara, H. Cong, J. Li, Corrosion Behavior of Friction Stir Blind Riveted Al/CFRP and Mg/CFRP Joints Exposed to a Marine Environment, *Corros. Sci.***132**, 300–309 (2018).

6. Z. Feng, J. Boerstler, G.S. Frankel, C.A. Matzdorf, Effect of Surface Pretreatment on Galvanic Attack of Coated Al Alloy Panels, *Corrosion*, **71**, 771–783, (2015).

7. P.M. Natishan, Perspectives on Cloride Interactions with Passive Oxides and Oxide Film Breakdown, *Corrosion*, **74**, 263–275, (2017).

8. R. Lumley, *Fundamentals of Aluminium Metallurgy: Production, Processing and Applications*; Woodhead Publishing Ltd.: Cambridge, UK, (2011).

9. A. Boag, A.E. Hughes, A.M. Glenn, T.H. Muster, D. McCulloch, Corrosion of AA2024-T3 Part I: Localised Corrosion of Isolated IM Particles, *Corros. Sci.*, **53**, 17–26, (2011).

10. A.E. Hughes, A. Boag, A.M. Glenn, D. McCulloch, T.H. Muster, C. Ryan, C. Luo, X. Zhou, G.E. Thompson, Corrosion of AA2024-T3 Part II: Co-operative Corrosion, *Corros. Sci.*, **53**, 27–39 (2011).

11. A.M. Glenn, T.H. Muster, C. Luo, X. Zhou, G.E. Thompson, A. Boag, A.E. Hughes, Corrosion of AA2024-T3 Part II: Propagation, *Corros. Sci.*, **53**, 40–50, (2011).

12. J.G. Kaufman, *Introduction to Aluminum Alloys and Tempers*, ASM International, Materials Park, OH, (2000).

13. D. Herzog, V. Seyda, E. Wycisk, C. Emmelmann, Additive Manufacturing of Metals, *Acta Mater.*, **117**, 371–392, (2016).

14. N.T. Aboulkhair, M. Simonelli, L. Parry, I. Ashcroft, C. Tuck, R. Hague, 3D Printing of Aluminium Alloys: Additive Manufacturing of Alumnium Alloys Using Selective Laser Melting, *Prog. Mater. Sci.*, **106**, 100578, (2019).

15. R. Twite, G. Bierwagen, Review of Alternatives to Chromate for Corrosion Protection of Aluminum Aerospace Alloys, *Prog, Org. Coat.*, **33**, 91-100, (1998).

16. Wernick; Pinner; Sheasby, *The Surface Treatment and Finishing of Aluminium and its Alloys*, ASM International and Finishing Publications Ltd, England, (1987).

17. J.T. Qi, T. Hashimoto, J.R. Walton, X. Zhou, P. Skeldon, G.E. Thompson, Trivalent Chromium Conversion Coating Formation on Aluminium, *Surf. Coat. Tech.*, **280**, 317-329, (2015).

18. X. Verdalet-Guardiola, B. Fori, J.P. Bonino, S. Duluard, C. Blanc, Nucleation and Growth Mechanisms of Trivalent Chromium Conversion Coatings on 2024-T3 Aluminium Alloy, *Corros. Sci.*, **155**, 109-120, (2019).

19. L. Li, G.P. Swain, A. Howell, D. Woodbury, D.; G.M. Swain, The Formation, Structure, Electrochemical Properties and Stability of Trivalent Chrome Process (TCP) Coatings on AA2024, *J. Electrochem. Soc.*, **158**, C274-C283, (2011).

20. Y. Guo, G.S. Frankel, Characterization of Trivalent Chromium Process Coating on AA2024-T3, *Surf. Coat. Tech.*, **206**, 3895-3902, (2012).

21. J. Walton, T.K. Shruthi, D. Yancey, P. Vlasak, S. Westre, G.M. Swain, Evaluation of a Trivalent Chromium Process (TCP) Conversion Coating on AA2024-T3 that Requires No Surface Pretreatment, *J. Electrochem. Soc*., **166**, C589-C599, (2019).

22. L. Li, G.M. Swain, Effects of Aging Temperature and Time on the Corrosion Protection Provided by Trivalent Chromium Process Coatings on AA2024-T3. *ACS Appl. Mater. Inter.*, **5**, 7923-7930, (2013).

23. C.A. Munson, S.A. McFall-Boegeman, G.M. Swain, Cross Comparison of TCP Conversion Coating Performance on Aluminum Alloys During Neutral Salt-Spray and Thin-Layer Mist Accelerated Degradation Testing, *Electrochim. Acta*, **282**, 171-184, (2018).

24. S.A. Abdel-Gawad, W.M. Osman, A.M. Fekry, Characterization and Corrosion Behavior of Anodized Aluminum Alloys for Military Industries Applicatios in Artificial Seawater, *Surf. Interfaces*, **14**, 314–323 (2019).

25. D. Veys-Renaux, N. Chahboun, and E. Rocca, Anodizing of Multiphase Aluminium Alloys in Sulfuric Acid: In-Situ Electrochemical Behaviour and Oxide Properties, *Electrochim. Acta*, **211**, 1056–1065 (2016).

26. Z. Wu, C. Richter, and L. Menon, A Study of Anodization Process During Pore Formation in Nanopourous Alumina Templates, *J. Electrochem. Soc.*, **154**, E8-E12 (2007).

27. Y. Zuo, P.-H. Zhao, and J.M. Zhao, The Influences of Sealing Methods on Corrosion Behavior of Anodized Aluminum Alloys in NaCl Solutions, *Surf. Coat. Tech.*, **166**, 237–242 (2003).

# CHAPTER 2 - Materials and Methods

## 2.1 Materials

### *Reagents*

Sodium sulfate ($Na_2SO_4$), sulfuric acid ($H_2SO_4$) and sodium chloride (NaCl) and potassium permanganate ($KMnO_4$) were purchased from Sigma-Aldrich (St. Louis, MO). Nitric acid ($HNO_3$) was purchased from Fisher Scientific (Hampton, NH). Sodium hydroxide was purchased from Spectrum (New Brunswick, NJ). All chemicals were analytical grade quality, or better, and were used without additional purification. All solutions were prepared with ultrapure water (Barnstead E-Pure) having a resistivity of >17 MΩ-cm.

For the studies in Chapter 3 Cleaner 1000, TCP-1 (TCP-NP), and TCP-2 (TCP-HF) baths were obtained from CHEMEON Surface Technology (Minden, NV). The TCP-1 bath was prepared by mixing two components in ultrapure water at concentrations of 0.5 % (v/v) for part A and 5 % (v/v) for part B. The TCP-2 bath concentrate was diluted with ultrapure water to 30 vol. % prior to use. In Chapters 4 and 5 Turco 6849 (20% v/v, Henkel Corp., Madison Heights, MI) was the commercial degreasing solution used. Turco Liquid Smut-Go (20% v/v, Henkel Corp., Madison Heights, MI) served as the deoxidizing solution. Bonderite T-5900 RTU (Henkel Corp., Madison Heights, MI) was the commercial TCP coating bath studied. All solutions were prepared using ultrapure water (Barnstead) with a resistivity greater than 17 MΩ-cm. No filtration was applied to remove solid particulates from the bath prior to use.

### *Aluminum Specimens*

In Chapter 3 aluminum alloy 2024-T3 was procured as a 2 mm-thick sheet (12" × 12", www.metalsonline.com) that was cut into 1 $in^2$ specimens. In Chapter 4 and 5 the aluminum alloy A360 ($AlSi_{10}Mg$) specimens used were fabricated at Honeywell FM&T (KCNSC) by selective laser melting using a SLM®500 industrial 3D printer (SLM Solutions, Germany). The specimens were printed from an $AlSi_{10}Mg$ source alloy powder, explained in more detail later. The specimens used in this work were fabricated with two dimensions: 2.54 cm × 2.54 cm × 0.635 cm (thickness) and 5.08 cm × 5.08 cm × 0.635 cm (thickness). such that the large face (length × height) is the XZ plane orthogonal to the build plane. The following parameters were used for part fabrication: laser power = 350 W, hatch spacing = 130 μm, powder layer thickness = 30 μm, and laser scan velocity = 1650 mm/s. These parameters were selected based on prior work at KCNSC.

## 2.2 Surface Preparation

*Polishing*

The specimens were mechanically abraded using 1500 grit wet aluminum oxide paper. This was followed by a fine polish by hand using 0.3 μm alumina grit (Buehler) slurry with ultrapure water on a felt polishing pad. A 20-min ultrasonic cleaning in ultrapure water was performed after each polishing step.

*Pretreatment and TCP coating*

The polished specimens were then degreased in Cleaner 1000 (45 g/L, CHEMEON) at 55°C for 10 min followed by a 2-min ultrapure water rinse. The degreased and $N_2$-dried specimens were then either immersion coated (TCP-1) or deoxidized in 30 wt.% $HNO_3$ for 2 min at room temperature followed by a 2-min ultrapure water rinse before being immersion coated (TCP-2). Both TCP coatings were applied at room temperature for 10 min. The pH of both TCP baths was adjusted to 3.85 using 0.25 M NaOH or 0.5 M $H_2SO_4$, as required. The coated specimens were rinsed by immersion in city tap water for 2 min with no agitation. This was followed by air drying overnight in a covered dish before further testing.

Post-fabrication treatment was performed internally according to KCNSC standard practice in a spray booth. This consisted of five steps: (i) high pressure spray with detergent and rinse with water, (ii) ultrasonication in detergent followed by a water rinse, (iii) ultrasonication in detergent followed by a water rinse and then drying with a stream of nitrogen gas, (iv) vacuum oven drying, and (v) packaging the cooled specimens into nylon bag for shipment to MSU. Throughout the manuscript, we refer to these specimens as "as-prepared." As-prepared A360 alloy specimens were pretreated prior to the electrochemical testing and microscopy measurements by solution processing in two steps. The specimens were first cleaned by immersion in an alkaline degreaser (Henkel Turco 6849) for 10 min at 55 °C followed by a 2-min flowing city tap water rinse. The degreased specimens were then deoxidized (Henkel Turco Liquid Smut-Go NC) by immersion for 2 min at room temperature. The samples were rinsed again in flowing city tap water for 2 min, dried with a low pressure nitrogen gas flow, and tested immediately thereafter. For the conversion coating with TCP, the A360 specimens were first cleaned and deoxidized, as described above. The specimens were then immersion coated in a TCP bath (Bonderite T-5900 RTU) for 10, 15, or 20 min at room temperature. After immersion coating, the specimens were immersed in city tap water for 2 min followed by a 30 s immersion rinse in ultrapure water (>17 MΩ-cm).

## 2.3 Anodizing

Specimens were anodized in 9.8 vol% $H_2SO_4$. A DC power supply (Tenma) was used to control the applied voltage for anodization. The positive terminal was connected to the $AlSi_{10}Mg$ specimen (anode) with a wire and alligator clip. The cathode was a piece of SS304L plate with dimensions of 2.5 cm × 1.7 cm and a 0.1 cm thickness. The electrodes were placed parallel at a fixed distance of 5.7 cm using a clamp secured to a ring stand shown in Figure 2.1. Anodization was performed in a 400 mL beaker filled with 9.8 vol.% $H_2SO_4$. The electrodes were lowered into the bath such that approximately 1.9 cm (about 3/4 of the sample height) of each was immersed. The anodizing process began at 0 V ramping to 15 V at a rate of 5 V/min in 1 V steps. After the 3-min ramp, the voltage was held at 15 V for 20 min. The anodized specimen was removed from the beaker and rinsed with ultrapure water. To fully remove slowly dissolving anodization smut, the specimen was immersed in ultrapure water for at least 20 min with periodic agitation. Finally, the specimen was then dried with a stream of $N_2$ and stored in a covered petri dish in the lab atmosphere for at least 24 h before further testing. The oxide weight after anodization was determined by an acid stripping method, as described in ASTM B137 (measurement of coating mass per unit area on anodically coated aluminum), described later.

**Figure 2.1.** Photograph of anodization setup.

## 2.4 Electrochemical Testing

All electrochemical measurements were conducted in a 1 $cm^2$ flat cell using a computer-controlled electrochemical workstation (Gamry Instruments, Inc, Reference 600, Warminster, PA). The alloy specimen was mounted in the cell against a Viton O-ring that defined the exposed geometric area, 1 $cm^2$. All currents reported herein, are normalized to the geometric area. The counter electrode was Pt (flag or mesh) and the reference was a home-made Ag/AgCl electrode (4 M KCl, $E^0$ = +0.197 V vs. NHE) that was housed in a Luggin capillary with a cracked glass tip. The following electrochemical measurements were made on all specimens: (i) open circuit potential (OCP) measurement, (ii) electrochemical impedance spectroscopy (EIS) from $10^6$ Hz to $10^{-2}$ Hz at the OCP using a 10 mV rms sine wave, and (iii) potentiodynamic polarization curves from the OCP. All measurements were made on three or more specimens to enable statistical analysis. The electrolyte used in all the measurements was naturally aerated 0.5 M $Na_2SO_4$ + 0.01 M NaCl at room temperature.

### *Scanning Electron Microscopy - Energy Dispersive X-ray Spectroscopy (SEM - EDS)*

Scanning electron microscopy was performed using a JEOL 6610 and a JEOL 7500F electron microscope (JEOL Ltd, Tokyo, Japan) both housed in the Center for Advanced Microscopy (MSU). Energy dispersive X-ray spectra (EDXS) were recorded using an AZtec detection system (Oxford Instruments, UK) attached to the SEM. The data were analyzed using the associated software (version 3.1). The measurements were performed to assess the elemental composition across the alloy surface and the location of TCP coating elements, and the oxide layer thickness and composition.

*Digital optical microscopy*

The surface texture of the specimens was assessed using a Keyence VHX-6000 digital optical microscope. Low resolution images were collected with a 20–200× zoom lens (VH-Z20). Images of different regions and focal planes were stitched together to produce a 3D profile of the entire specimen surface. High resolution images were collected with a 500–5000× zoom lens (VH-Z500) and used to quantitatively assess the surface texture and other structural features. The topographical data were analyzed to calculate the surface roughness and maximum peak-to-valley distance. For this analysis, five spots were randomly selected on any one specimen in a grid pattern. At least five different as-prepared specimens were used in the measurements.

*XPS analysis*

Surface and depth elemental composition were assessed by X-ray photoelectron spectroscopy (XPS). Conversion-coated alloy specimens were attached to an analysis platen with copper tape. Data were collected on a VersaProbe II Microprobe XPS operating in the high-power mode (Dow Chemical Company). A 100 μm X-ray spot set at 100 W was rastered over a 1 mm line to reduce damage to the sample as well as the X-ray anode, while still providing maximal signal-to-noise. The pass energy was 23.5 eV, the step size was 0.1 eV/step, and the dwell time was adjusted from element to element in order to achieve suitable signal-to-noise. Elemental regions that were collected were Na 1s, Cu 2p, F 1s, Cr 2p, O 1s, C 1s, Zr 2p, S 2p, P 2p and Al 2p and 2s. Data analysis was performed using CasaXPS software. Relative sensitivity factors (RSFs) for the elements of interest were taken from the instrument manufacturer. For depth profile analysis, a pass energy of 58.7 eV was used with a step size of 0.125 eV/step. The analysis spot size was 200 μm. Data were collected between 60 second Ar ion sputtering cycles. The sputtering conditions used Ar ions with an accelerating voltage of 2 kV. A beam raster size of 1 mm × 1 mm was used with a target ion current of ~2.5 μA. The average sputter rate through the TCP coating was determined to be 0.08 nm/s or ~5 nm/min. The rate was obtained by measuring the total crater depth with a KLA Tencor P-17 stylus profilometer. The profilometer has ~1 nm depth resolution and ~10 μm lateral resolution. The depth of the crater was then divided by the sputter time to give that average sputter rate.

## 2.5 Accelerated Degradation

*14 day full immersion*

Uncoated and TCP-coated AA2024-T3 specimens were fully immersed in 3.5 wt.% NaCl at 55°C for 14 days in a polycarbonate container. A hole was drilled in the lid of the container to minimize water evaporation and allow for natural aeration of the salt solution.

*Neutral salt spray test*

The uncoated and TCP-coated A360 specimens were exposed to a continuous salt spray for 14 days according to ASTM B117 (Standard Practice for Operating Salt Spray (Fog) Apparatus). A 5 wt% NaCl salt solution was continuously sprayed in the test chamber to create a saturated fog at 35 ± 1 °C. The specimens were positioned at an angle of 20° relative to the normal axis. The specimens were subjected to fog for up to 14 days, or until surface pitting was visually observed. Specimens were inspected visually each day for corrosion damage. The specimens were weighed prior to salt fog exposure. After the test, the specimens were ultrasonically cleaned in ultrapure $H_2O$ for 30 min to remove salt deposits. They were then ultrasonically cleaned in concentrated $HNO_3$ for 10 min to dissolve corrosion product, dried thoroughly with nitrogen gas, and reweighed once again. Ultrasonic cleaning in $HNO_3$ was then repeated in 1-min increments until the mass change of a specimen was negligible (≤0.002 g).

*Corrosion evaluation*

The following scale, developed by the U.S. Army Material Command, was used to grade the specimens after the neutral salt-spray exposure: Stage 0—shows no visible corrosion; Stage 1—sample discoloration and staining; Stage 2—loose isolated rust or corrosion product and early stage pitting of the surface along with minor etching; Stage 3—more extensive rust or corrosion product, minor etching, pitting and more extensive surface damage; Stage 4—extensive rust or corrosion product formation, extensive etching, blistering, deadhesion, and pitting that has progressed to the point where the life of the specimen has been affected.

## 2.6 Vickers Microhardness

The microhardness test was performed according to ASTM E384–17 (Standard Test Method for Microindentation Hardness of Materials). A diamond pyramid tip indenter was used to apply indentations at five different spots across a representative specimen using a load of 0.5 kg. The indentation time was 15 s. Each indentation was evaluated for symmetry and defects. The diagonals of the indentation were measured, and the hardness was calculated.

# CHAPTER 3 - Evaluation of a Trivalent Chromium Process (TCP) Conversion Coating on AA2024-T3 That Requires No Surface Pretreatment

Chapter adapted from *J. Electrochem. Soc.*, **166** (15) C589-C599 (2019), Copyright 2019, The Electrochemical Society

*Article: Jack Walton, T. K. Shruthi, David Yancey, Paul Vlasak, Sjon Westre, and Greg M. Swain- Evaluation of a Trivalent Chromium Process (TCP) Conversion Coating on AA2024-T3 That Requires No Surface Pretreatment*

## 3.1 Abstract

We report on the study of a new commercial trivalent chromium process (TCP) conversion coating, TCP-1, that requires no deoxidation or etching surface preparation of the aluminum alloy for optimum performance. The corrosion resistance provided by TCP-1 and a comparable conversion coating, TCP-2, both formed by immersion on AA2024-T3, were evaluated using scanning electron microscopy and energy dispersive X-ray analysis, digital microscopy, XPS depth profiling, electrochemical impedance spectroscopy and potentiodynamic polarization techniques. Accelerated degradation testing was also performed to determine how the laboratory electrochemical data correlate with the coating's corrosion protection during neutral salt-spray exposure and full-immersion testing. The results indicate that TCP-1 produces a protective coating on the metal that minimizes corrosion to an equivalent degree as TCP-2; a conversion coating that requires a conventional deoxidation step prior to application. Electrochemical data revealed that both TCP coatings increase the polarization resistance by ∼100x and suppress anodic and cathodic currents by ∼10–100x, as compared to the uncoated alloy. Specimens coated with either TCP coating exhibited little degradation, discoloration or corrosion during a 14-day neutral salt-spray (ASTM B117) exposure and a 14-day full

immersion in 3.5 wt.% NaCl at 55°C. In summary, the stand-alone corrosion protection provided by TCP-1 to this alloy is as good as the protection provided by a standard TCP coating.

## 3.2 Introduction

Aluminum alloys are used extensively in the aerospace industry because of their light weight, high strength, low thermal expansion and good wear resistance.[1–4] These alloys have a complex microstructure with dispersed intermetallic phases making them susceptible to localized corrosion.[5–7] Chromate conversion coatings (CCC) have been used effectively for decades in the aerospace industry, generally as part of a multilayer coating system, to inhibit corrosion of aluminum alloys.[8–13] Even so, the high toxicity of Cr(VI) and increasingly strict governmental restrictions on its use in surface finishes has forced the aerospace industry to seek alternate, more eco-friendly coatings to replace CCC.[14–16] Several non-chromate and non-chromium alternatives have been studied including titanium, zirconium, cerium and trivalent chromium-based conversion coatings.[17–23] The leading replacement alternative in the aerospace industry is presently the trivalent chromium process (TCP) conversion coating.

Researchers have reported on the formation, chemical composition and corrosion protection of various commercial versions of TCP formed by immersion and spray on aluminum alloys.[24–49] The TCP bath consists primarily of hexafluorozirconic acid and a Cr (III) salt at a pH of 3.5–3.8. The coating, when formed by a 10-min immersion, is generally a 150–200 nm thick metal oxyhydroxide layer composed of an outer hydrated zirconia layer rich in Cr (~10 at. %) and a hexafluoroaluminate interfacial layer.[28–33,41–44] Electrochemical data are available for all the commercial versions of TCP. The results indicate the coating provides both anodic and cathodic protection.[29,33,34,41,42,44] The anodic protection arises from the physical barrier layer the coating provides that reduces alloy contact with the environment. The coating also forms with greater coverage on and around exposed cathodic intermetallic phases. The cathodic protection results from the coating (i) serving as a diffusional barrier to dissolved oxygen and (ii) blocking O2 chemisorption sites on the intermetallic particles, thus reducing the rate of oxygen reduction.[28–33,40–44]

TCP is typically formed by immersion or spray on alloy surfaces pretreated by cleaning/degreasing and deoxidation/etching.[27–45] In this work, experiments were conducted to compare two commercial TCP coatings, a traditional one that requires a deoxidation step (TCP-2)[44] and a new conversion coating that requires no conventional deoxidation or etching surface pretreatment (TCP-1). The deoxidation is a processing step that removes smut and oxide layers from the alloy surface. Removal of these layers is necessary for electrochemical reactions (e.g., dissolved oxygen reduction) to occur at a significant rate under the open circuit conditions to increase in the local solution pH near the surface. This more alkaline solution environment causes the precipitation of the conversion coating constituents, hydrated zirconia and chromium (III) hydroxide.[27,28,30,32–35,41–45]

The practical benefits of this new conversion coating (TCP-1) are (i) no need for a separate deoxidation surface pretreatment step thus eliminating a process tank, (ii) a reduction in the volume of hazardous waste generated that must be monitored and disposed of and (iii) a reduction in the overall specimen processing time. Studies were conducted to compare the corrosion resistance of TCP-1 with a comparable coating, TCP-2, that requires typical deoxidation surface pretreatment prior to application. Electrochemical and material characterization data are reported for aluminum alloy, AA2024-T3, coated by immersion with both conversion coatings. Results are also presented that reveal the corrosion protection afforded by both coatings during 14-day (i) neutral salt-spray exposure and (ii) full-immersion.

## 3.3 Experimental

*Reagents*

All chemicals were analytical grade quality, or better, and were used without additional purification. Sodium sulfate ($Na_2SO_4$), sulfuric acid ($H_2SO_4$) and sodium chloride (NaCl) were purchased from Sigma-Aldrich (St. Louis, MO). Nitric acid ($HNO_3$) was purchased from Fisher Scientific (Hampton, NH). Sodium hydroxide was purchased from Spectrum (New Brunswick, NJ). Cleaner 1000, and the TCP-1 (TCP-NP) and TCP-2 (TCP-HF) baths were obtained from CHEMEON Surface Technology (Minden, NV). All solutions were prepared using ultrapure water (Barnstead) with a resistivity greater than 17 MΩ-cm. No filtration was applied to remove solid particulates from the bath prior to use.

*Specimen Preparation*

Aluminum alloy 2024-T3 was procured as a 2 mm-thick sheet (12" × 12", www.metalsonline.com) that was cut into 1 $in^2$ specimens. The specimens were mechanically abraded using 1500 grit wet aluminum oxide paper. This was followed by a fine polish by hand using 0.3 μm alumina grit (Buehler) slurry with ultrapure water on a felt polishing pad. A 20-min ultrasonic cleaning in ultrapure water was performed after each polishing step. The polished specimens were then degreased in Cleaner 1000 (45 g/L, CHEMEON) at 55°C for 10 min followed by a 2-min ultrapure water rinse. This cleaner/degreaser is a non-silicate and non-etching alkaline cleaner for aluminum with a pH between 9 and 10. The cleaner is approximately 30 wt.% sodium borate (borax).

The degreased and $N_2$-dried specimens were then either immersion coated (TCP-1) or deoxidized in 30 wt.% $HNO_3$ for 2 min at room temperature followed by a 2-min ultrapure water rinse before being immersion coated (TCP-2). Both TCP coatings were applied at room temperature for 10 min. The TCP-1 bath was prepared by mixing two components in ultrapure water at concentrations of 0.5 % (v/v) for part A and 5 % (v/v) for part B. The combination of these two components produce a solution of chromium (III) sulfate, potassium fluorozirconate, and a phosphate compound. The TCP-2 bath concentrate was diluted with ultrapure water to 30 vol. % prior to use. The pH of both TCP baths was adjusted to 3.85 using 0.25 M NaOH or 0.5 M $H_2SO_4$, as required. The coated specimens were rinsed by immersion in city tap water for 2 min with no agitation. This was followed by air drying overnight in a covered dish before further testing.

### *Neutral salt spray test (ASTM B117)*

The TCP-coated AA2024-T3 specimens were exposed to a 14-day neutral salt spray (NSS) (5 wt% NaCl and 35 ± 1°C) in a commercial 4 $ft^3$ salt-spray chamber (MX 9204, Associated Environmental Systems), as per MIL-DTL-81706B. The test was conducted according to the standard practice (ASTM B117). The salt solution in the chamber was refilled daily. Polished, degreased and deoxidized specimens were used as uncoated controls.

### *14-day full immersion test*

Uncoated and TCP-coated AA2024-T3 specimens were fully immersed in 3.5 wt.% NaCl at 55°C for 14 days in a polycarbonate container. A hole was drilled in the lid of the container to minimize water evaporation and allow for natural aeration of the salt solution.

*Weight loss measurements*

Weights of uncoated and TCP-coated AA2024-T3 specimens were measured before and after the 14-day NSS test to determine the amount of material loss. Specimen weights were recorded 30 min before the start of the test. After 14 days, the specimens were subjected to a 30-min ultrasonic cleaning in ultrapure water followed by a 10-min ultrasonic cleaning in 20 wt.% $HNO_3$ to remove excess salt and corrosion product from the surface. The specimens were then rinsed with flowing ultrapure water and dried with $N_2$ before recording the final weight. The acid cleaning step was repeated until a final constant specimen weight was obtained (±0.5 mg).

*Electrochemical measurements*

All electrochemical measurements were conducted in a 1 $cm^2$ flat cell using a computer-controlled electrochemical workstation (Gamry Instruments, Inc, Reference 600, Warminster, PA). The alloy specimen was mounted in the cell against a Viton O-ring that defined the exposed geometric area, 1 $cm^2$. All currents reported herein, are normalized to the geometric area. The counter electrode was a Pt flag and the reference was a home-made Ag/AgCl electrode (4 M KCl, $E^0 = +0.197$ V vs. NHE) that was housed in a Luggin capillary with a cracked glass tip. All measurements were made in naturally-aerated 0.5 M $Na_2SO_4$ + 0.01 M NaCl at room temperature (23 ± 2°C). The following electrochemical measurements were made on all specimens: (i) 30-min open circuit potential (OCP) measurement, (ii) electrochemical impedance spectroscopy (EIS) from $10^6$ Hz to $10^{-2}$ Hz at the OCP using a 10 mV rms sine wave, and (iii) potentiodynamic polarization curves from the OCP to 0.5 V (anodic) or −1.2 V (cathodic) vs. Ag/AgCl. All measurements were made on three or more specimens to enable statistical analysis.

For the polarization curves, the cathodic scan was recorded first followed by the anodic scan on the same specimen.

### *SEM and EDXS analysis*

Scanning electron microscopy was performed using a JEOL 6610 electron microscope (JEOL Ltd, Tokyo, Japan) housed in the Center for Advanced Microscopy (MSU). Energy dispersive X-ray spectra (EDXS) were recorded using an AZtec detection system (Oxford Instruments, UK) attached to the SEM. The data were analyzed using the associated software (version 3.1). Spectra were recorded using a 15 keV accelerating voltage. A digital optical microscope (Keyence VHX 6000) was used to obtain 3-dimensional surface topographic profiles of the alloy specimens before and after the salt-spray exposure. The depth resolution was ca. 0.2 μm.

### *XPS analysis*

Surface and depth elemental composition were assessed by X-ray photoelectron spectroscopy (XPS). Conversion-coated alloy specimens were attached to an analysis platen with copper tape. Data were collected on a VersaProbe II Microprobe XPS operating in the high-power mode (Dow Chemical Company). A 100 μm X-ray spot set at 100 W was rastered over a 1 mm line to reduce damage to the sample as well as the X-ray anode, while still providing maximal signal-to-noise. The pass energy was 23.5 eV, the step size was 0.1 eV/step, and the dwell time was adjusted from element to element in order to achieve suitable signal-to-noise. Elemental regions that were collected were Na 1s, Cu 2p, F 1s, Cr 2p, O 1s, C 1s, Zr 2p, S 2p, P 2p and Al 2p and 2s. Data analysis was performed using CasaXPS software. Relative sensitivity factors (RSFs) for the elements of interest were taken from the instrument manufacturer. For depth profile analysis, a pass energy of 58.7 eV was used with a step size of 0.125 eV/step. The analysis spot size was 200 μm. Data were collected between 60 second Ar ion sputtering cycles. The sputtering conditions used Ar ions with an accelerating voltage of 2 kV. A beam raster size of 1 mm × 1 mm was used with a target ion current of ~2.5 μA. The average sputter rate through the TCP coating was determined to be 0.08 nm/s or ~5 nm/min. The rate was obtained by measuring the total crater depth with a KLA Tencor P-17 stylus profilometer. The profilometer has ~1 nm depth resolution and ~10 μm lateral resolution. The depth of the crater was then divided by the sputter time to give that average sputter rate.

## 3.4 Results

Figure 3.1 shows open circuit potential (OCP) vs. time curves for AA2024-T3 specimens during the immersion coating of TCP-1 and TCP-2. Nearly identical time-dependent potential profiles are seen for both coatings. Even without any deoxidation surface pretreatment, the TCP-1 coating bath contains chemical constituents that rapidly dissolve the native oxide and expose the underlying aluminum. This activity is reflected by the rapid decrease of potential to −1.1 V during the first ~60 s.[33,42,45] Once the oxide is dissolved away, aluminum dissolution occurs at a higher rate and this is compensated for by a counterbalancing cathodic reaction (e.g., oxygen reduction) at an equivalent rate. Oxygen reduction and hydrogen evolution are likely both occurring at ~−1.1 V; a potential that is established 100 s into the immersion. Both reactions consume protons, and this leads to a pH increase in the electrolyte solution near the alloy surface. It is this pH increase that drives the conversion of soluble Zr and Cr coating bath precursors to form weakly soluble zirconia ($ZrO_2$•$nH_2O$) and chromium hydroxide ($Cr(OH)_3$) that deposit on the alloy surface to form the coating.[27–38,41–45] The native aluminum oxide ($Al_2O_3$) that passivates the metal surface, even after deoxidation, is dissolved by $F^-$ that is present in both coating baths. The fluoride concentrations in the different commercial TCP coating baths were determined by potentiometry and reported previously, including for TCP-2.[44] Values were 20–25 ppm for all the coating baths. A single measurement of TCP-1 yielded a value of ~10 ppm. This dissolution exposes the underlying metal and produces hexafluoroaluminate species that constitute the interfacial layer of the TCP coating as this is the first step of the process.[27–38,41–45] Dissolution of the oxide under acidic conditions also consumes protons and contributes to an increase in the pH of the nearby solution. The presumed reactions are shown below.[26,32,33]

$$\mathrm{Al_2O_3 + 6HF \rightarrow 2AlF_3 + 3H_2O}\ \text{(interface)}$$

$$\mathrm{ZrF_6^{2-} + 4OH^- \rightarrow ZrO_2 \cdot 2H_2O + 6F^-}\ \text{(coating)}$$

$$\mathrm{Cr^{3+} + 3OH^- \rightarrow Cr(OH)_3}\ \text{(coating)}$$

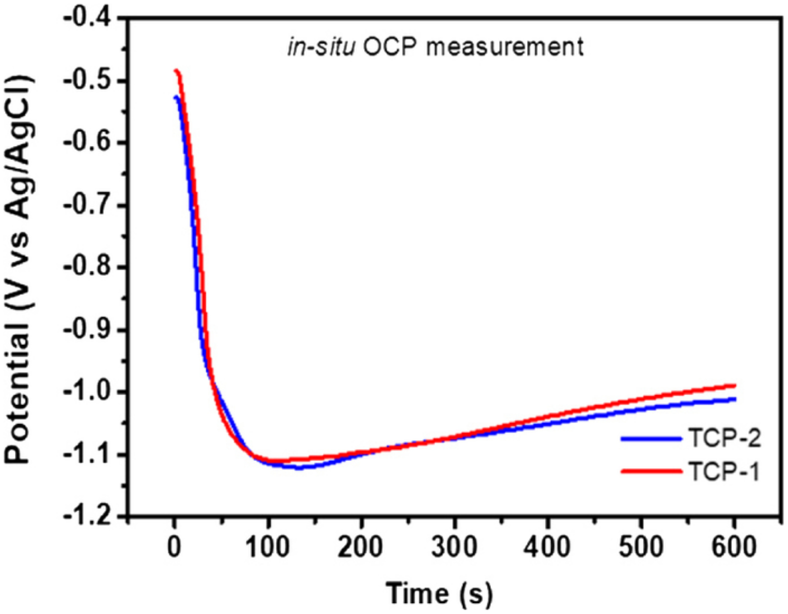

**Figure 3.1.** Open circuit potential (OCP) vs. time curves for AA2024-T3 specimens recorded during the 10-min immersion coating of TCP-1 and TCP-2 at room temperature.

Figure 3.2 shows plan view scanning electron micrographs of TCP-1 (A and B) and TCP-2 (C and D) immersion-coated AA2024-T3 specimens. The micrographs reveal that both conversion coatings form over all areas of the alloy, as evidenced by the presence of precipitate particles across the surface. This is further confirmed by the EDXS data for the primary coating elements, Zr and Cr, presented below. The small white precipitate particles are coating aggregates that serve as indicators of the coating's presence.[29,32–35,41,42,44] These are likely present in the coating bath and end up depositing on the surface as no bath solution filtration was performed prior to immersion coating. These precipitate particles range in size from < 1 to 10 μm and are commonly observed on alloy specimens coated with all the different commercial versions of TCP.[29,32–35,41,42,44] Clearly, these particulates are not totally removed or dissolved by the washing process. Higher magnification images shown in Figures 2B and 2D reveal small cracks in both conversion coatings. Our own experiments, and published work by others,[30] have shown these cracks result from coating dehydration and corresponding structural changes in the vacuum of the SEM (so-called mud cracking). Importantly, the cracking is not a result of the coating formation process. For example, an experiment was performed using specimens coated with TCP-1 and 2. The coated surfaces were investigated by digital microscopy right after coating, after drying overnight in the laboratory air and then after exposure to the vacuum of the SEM. Cracks were only detected on specimens exposed to the vacuum conditions.

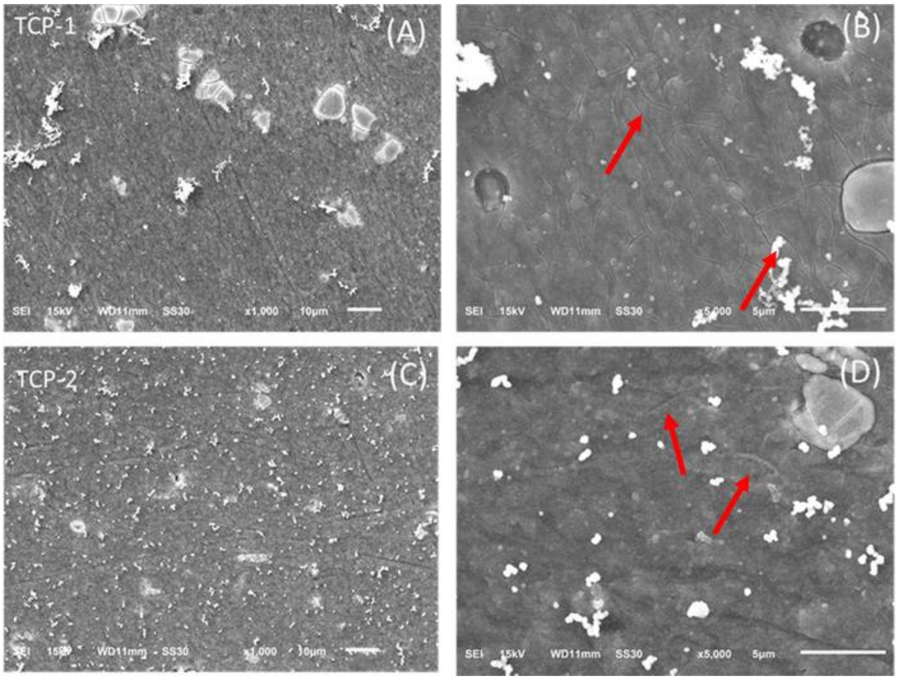

**Figure 3.2.** Plan view scanning electron micrographs showing the surface of AA2024-T3 immersion coated with (A and B) TCP-1 and (C and D) TCP-2. Arrows indicated the cracks seen in the coatings upon exposure to the vacuum. Micrographs are presented at two different magnifications.

Figure 3.3 shows plan view scanning electron micrographs of AA2024-T3 specimens coated with (A) TCP-1 and (B) TCP-2, and the corresponding EDXS elemental maps for Al, Zr and Cr across each coated alloy surface. Zr is present over the entire surface as is Cr but the intensity for the latter element is much lower consistent with a reduced atomic percentage in the coating. The data reveal that the coating precipitate particles also consist of Zr and Cr. The large feature at the right center of the micrograph for TCP-1 is an exposed intermetallic particle. Interestingly, it can be seen that the X-ray signal intensities are greater for Zr and Cr on and around the intermetallic particle, as compared to the surrounding surface. This is a very common observation for TCP coatings.[29,32–35,41,42,44] The increased coating coverage on and around intermetallic particles likely results because of a more alkaline solution environment that develops around the particle as compared to the surrounding solution contacting the aluminum. The more alkaline pH is caused by a higher rate of proton-consuming, oxygen reduction at the cathodically active intermetallics.

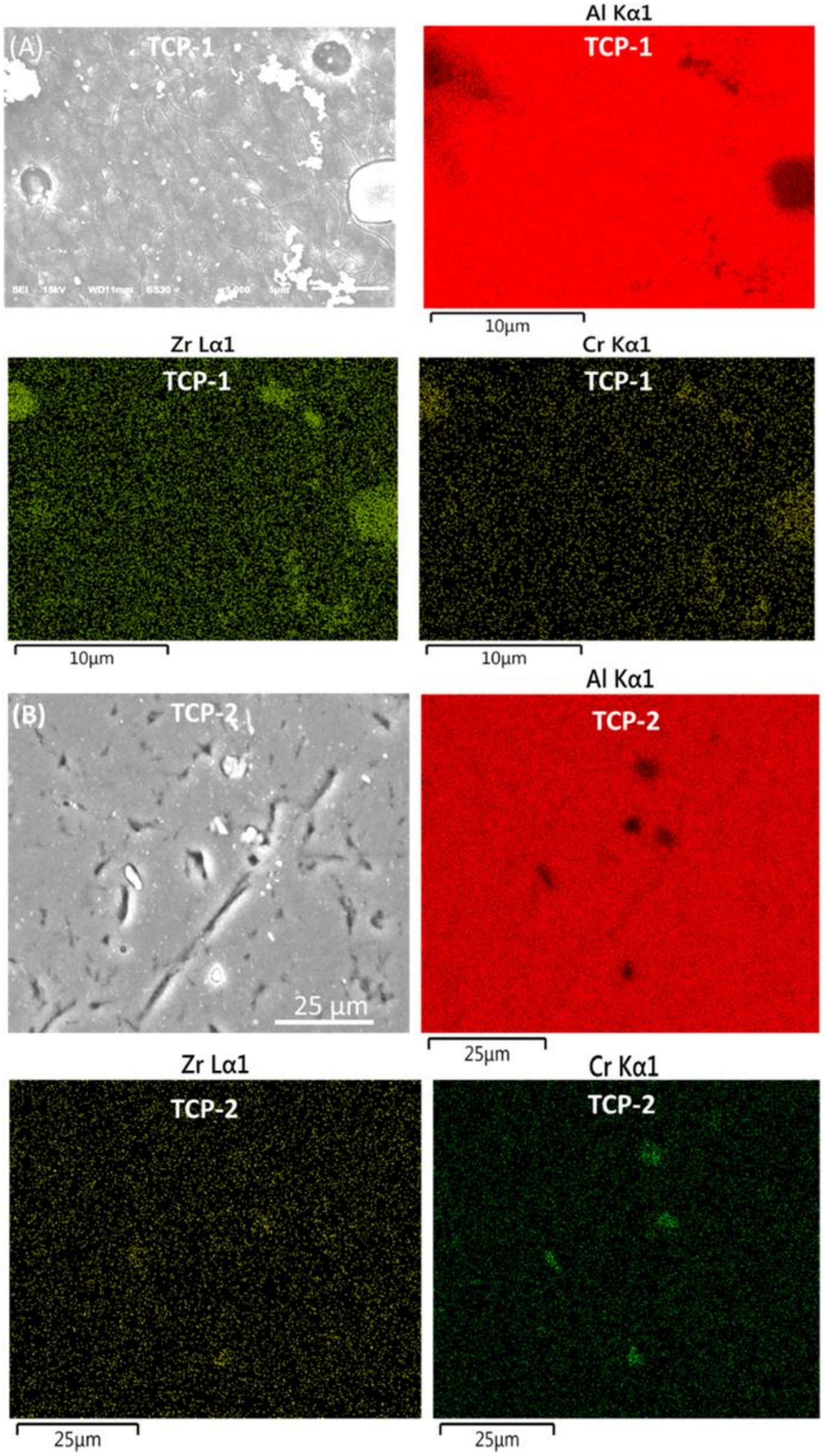

**Figure 3.3.** Plan view scanning electron micrographs and corresponding energy dispersive X-ray spectroscopy elemental maps for Al, Zr and Cr across the surface of (A) TCP-1-coated and (B) TCP-2-coated AA2024-T3. Cracking is evident in the SEM micrographs for both conversion

**Figure 3.3 (cont'd)**

coatings but is more pronounced for TCP-2. Note the difference in scale bar dimensions for the EDXS elemental maps for TCP-1 (10 μm) and TCP-2 (25 μm).

Figure 3.4 presents XPS depth profiles recorded through (A and B) TCP-1 and (C and D) TCP-2 on AA2024-T3. Signals for the primary elements (Zr, Cr and F) are detected in both coatings up to 2000 s of sputter time for TCP-1 and 2500 s for TCP-2. Using an apparent sputter rate of 0.08 nm/s, the coating thicknesses are estimated to be 160 and 200 nm, respectively, for TCP-1 and TCP-2. The elemental distributions for Zr, Cr and F with depth in both coatings reflect the biphasic composition expected for TCP coatings, as has been reported previously.[29,30,31,33–35,41,42,44] For TCP-1, the Zr and Cr concentrations reach a maximum of 24 and 6 at. %, respectively, at short sputter times (∼500 s or ∼40 nm) before decaying with depth into the coating. The F concentration increases progressively with depth into the coating before reaching a maximum of 14 at. % at longer sputter times (∼700 s) and then decreasing as the alloy surface is approached. The signal for F (fluoride sequestration) persists for about 1000 s of sputter time and this corresponds to ∼80 nm. This 80 nm represents the interfacial region between the alloy and the conversion coating. Zr and Cr are present in this interfacial region, but their concentrations decrease with distance into the coating. The Al signal is present in this interfacial region as well. The largest concentration of F is in the interfacial region of the coating. The F may exist as potassium hexafluoroaluminate ($K_3AlF_6$) in this region.

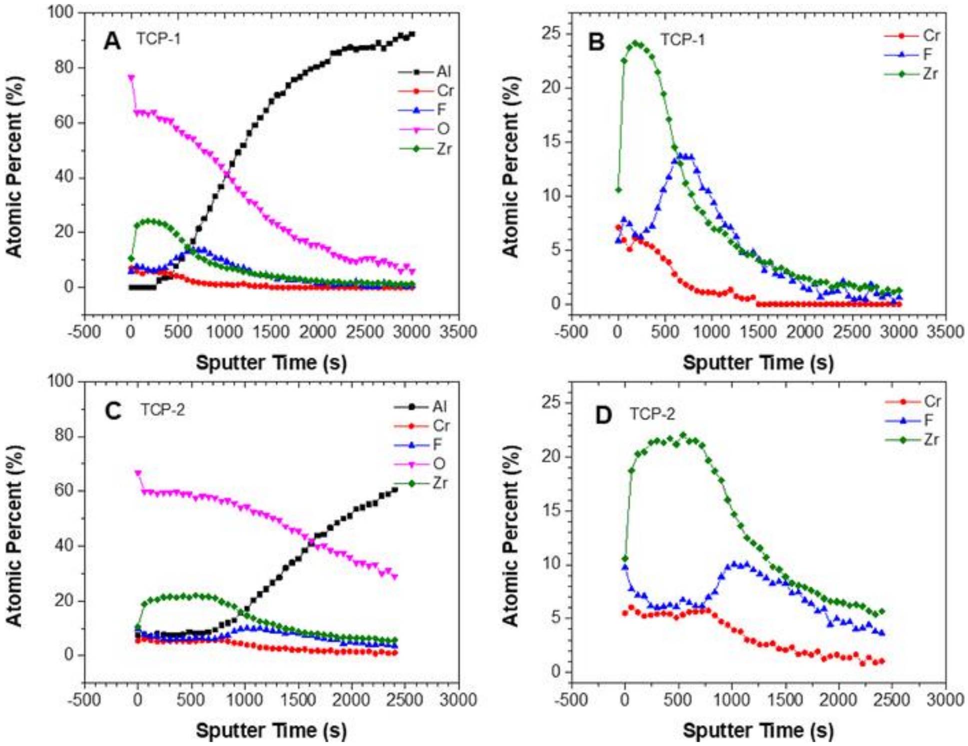

**Figure 3.4.** XPS depth profiles through (A and B) TCP-1 and (C and D) TCP-2 coatings formed on AA2024-T3 during a 10-min immersion.

For TCP-2, Zr and Cr are present in the outer region of the coating at maximum concentrations of 21 and 6 at. %, respectively. The maximum concentrations of these two coating elements extend deeper into TCP-2 than TCP-1, as the signals for both Zr and Cr are present up to 1000 s of sputter time or ~80 nm of depth. The maximum concentration of F is again seen in the interfacial region at 10 at. %. The apparent coating thicknesses of 160 and 200 nm are consistent with ellipsometry measurements of other commercial TCP coatings formed on aluminum alloys during a 10-min immersion.[27,28,42,44]

*Electrochemical characterization*

Measurements were performed to determine the electrochemical properties of the uncoated and TCP-coated alloys. Figure 3.5 shows electrochemical data for uncoated (polished, degreased and deoxidized) and TCP-coated AA2024-T3 specimens. All measurements were made in naturally-aerated 0.5 M $Na_2SO_4$ + 0.01 M NaCl. Figure 3.5A shows OCP vs. time profiles recorded upon initial immersion in the electrolyte solution. The OCP for this particular uncoated alloy drifts negatively during the first 1000 s before stabilizing at ca. −0.56 V. The OCP for this TCP-2 coated alloy changes little during the period stabilizing at ca. −0.49 V. The OCP for this TCP-1 coated alloy drifts positively over time, requiring about 3000 s to stabilize at ca. −0.42 V. Nominal OCP data for multiple specimens of each type are presented in Table 3.1. The data indicate that the mean OCP values for the TCP-coated and uncoated specimens are statistically similar.

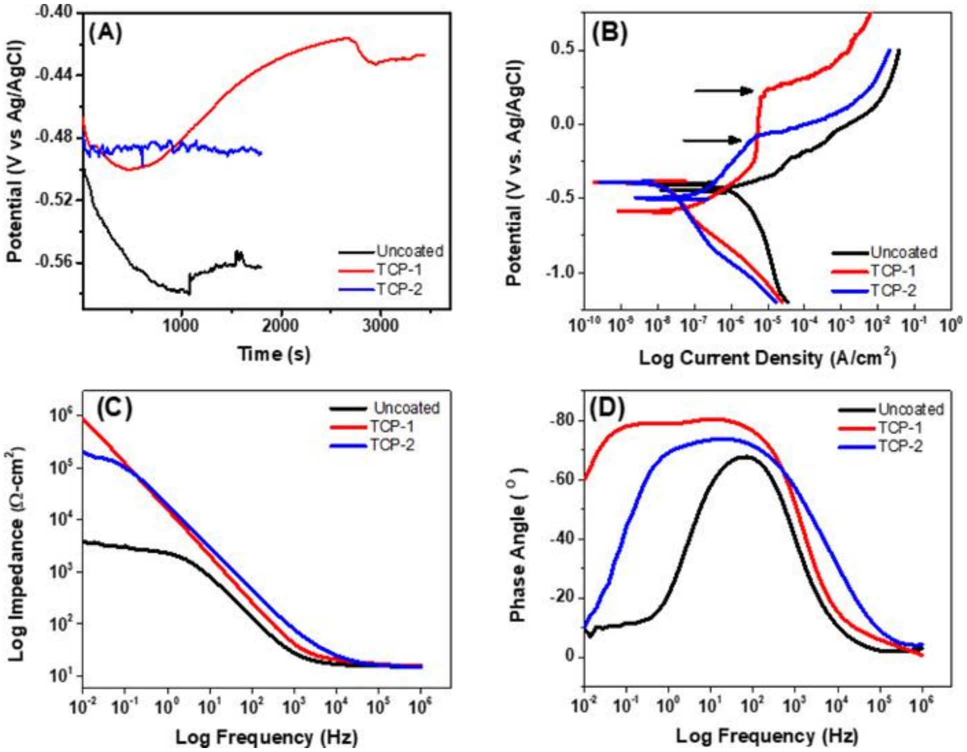

**Figure 3.5.** (A) Open circuit potential, (B) Slow scan potentiodynamic polarization curves, (C) Bode plots and (D) Phase angle vs. frequency plots for uncoated and TCP-coated AA2024-T3 specimens. All data are for the same three specimens. Measurements were made in naturally-aerated 0.5 M Nas$_2$SO$_4$ + 0.01 M NaCl at room temperature. The arrows in Figure 3.5B indicate the apparent pitting potential, $E_{pit}$.

**Table 3.1.** Summary of electrochemical parameters for uncoated and TCP-coated AA2024-T3 specimens. Mean ± std. dev. (n = 3 specimens of each type). No std. dev is reported for $E_{pit}$ (TCP-1) because only one sample showed stable pitting below 0.5 V, which was the positive potential limit of the polarization scan. *Indicates statistically significant difference in the mean values from uncoated controls ($p \leq 0.05$). Analysis performed by Student's T-test.

| | OCP (V vs. Ag/AgCl) | $E_{pit}$ (V vs. Ag/AgCl) | Current Density at −0.2 V (μA/cm$^2$) | Current Density at −0.8 V (μA/cm$^2$) | Z at 0.01 Hz (kΩ-cm$^2$) |
|---|---|---|---|---|---|
| Uncoated | −0.46 ±0.13 | Near OCP | 127 ± 40 | 6 ± 2 | 4.4 ± 0.8 |
| TCP-1 | −0.45 ±0.08 | >0.5 V | 1.7 ± 2.5* | 0.6 ± 0.1* | 894 ± 175* |
| TCP-2 | −0.43 ±0.09 | −0.13 ± 0.07 | 0.9 ± 0.7* | 0.3 ± 0.2* | 496 ± 378* |

The potentiodynamic polarization curves presented in Figure 3.5B reveal that both TCP coatings produce anodic and cathodic current suppression relative to the current levels for the uncoated specimen. The current suppression ranges from 10–100x at potentials around the OCP and is similar for both coatings. The pitting potential, $E_{pit}$, is shifted to more noble potentials because of the TCP coating. In this chloride containing electrolyte, $E_{pit}$ is close to the OCP for the uncoated specimen, which is why the current increases significantly during the positive-going scan at potentials just slightly more noble of the OCP. For TCP-1, a passivation region can be seen in the anodic curve extending out to the apparent $E_{pit}$ of 0.25 V. For TCP-2, the apparent $E_{pit}$ is less positive at −0.10 V. The more noble $E_{pit}$ for TCP-1 is consistent with the more noble OCP seen in Figure 3.5A. It was observed that about 30% of the TCP-1-coated specimens exhibited polarization curves with a well-defined $E_{pit}$ less positive of 0.5 V. The remaining specimens showed no signs of stable pit formation below this potential. The suppressed anodic current is due to the presence of the TCP coating acting as a physical barrier preventing alloy contact with the electrolyte solution. This reduces the alloy area in contact with the electrolyte solution, which lowers the rate of aluminum dissolution. The observed cathodic current suppression is due to a combination of the TCP functioning as a diffusional barrier to dissolved oxygen and a blocker of $O_2$ chemisorption on exposed intermetallic sites, which are kinetically active for oxygen reduction. $Cr(OH)_3$ formed on exposed intermetallic phases seems to be key for the site blocking effect.[40] Prior work and results presented herein (see Figure 3.3) revealed that there is greater conversion coating formation on and around intermetallic phases.[29,32–35,41,42,44]

Figure 3.5C and 5D show impedance magnitude and phase angle plots as a function of frequency, respectively, for uncoated and TCP-coated AA2024-T3 specimens in the same naturally-aerated electrolyte. The measurements were made at the OCP. The high frequency impedance arises from the ohmic resistance of the electrolyte solution, the TCP coating and the alloy, which is similar for all three specimens, as expected. The low frequency impedance at 0.01 Hz ($Z_{0.01Hz}$) reflects the polarization resistance; this is the resistance to the flow of current due to anodic and cathodic redox reactions occurring at the OCP. In Figure 3.5C, it can be observed that both TCP coatings increase $Z_{0.01\ Hz}$ by a factor of 10–100× as compared to the uncoated specimen. The low frequency impedance for TCP-1 is 2× greater than for TCP-2. The $Z_{0.01Hz}$ values seen here, $10^5$ to $10^6$ $\Omega$-cm$^2$, are 100x greater than the values seen for the uncoated alloy, $10^3$ to $10^4$ $\Omega$-cm$^2$. Table 3.1 presents nominal values for $Z_{0.01\ Hz}$. It can be seen that $Z_{0.01\ Hz}$ is

100× greater for TCP-2 and 200× greater for TCP-1. However, there is no statistically significant difference in the nominal values for the two TCP-coated specimens given the large standard deviation, particularly for TCP-2. Figure 3.5D shows that both TCP coatings exhibit more capacitive-like behavior at low frequencies, as compared to the uncoated specimen, based on the phase angles being in the −60 to −80-degree range.

Table 3.1 provides a summary of the measured electrochemical parameters for uncoated and both TCP-coated AA2024-T3 specimens. All values are reported as mean ± std. dev. ($n = 3$ specimens of each type). The nominal cathodic current density at −0.8 V (diffusion limited $O_2$ reduction) is 10× lower for TCP-1 and 20× lower for TCP-2, however statistically there is no difference between the two mean values given the standard deviation for TCP-2. The nominal anodic current density at −0.2 V (metal dissolution) is 60× lower for TCP-1 and 100× lower for TCP-2, as compared to the uncoated control. Both nominal current densities for the two TCP-coated specimens are statistically lower than the values for the uncoated alloy. The OCP and $Za_{0.01\ Hz}$ data were discussed above. The reason for the large variability in the TCP-2 data is unknown but may be related to the fact that a 10-min immersion period was used even though the supplier's recommended time for TCP-2 is 5 min. It could be that there is some coating degradation, mediated by species in the coating bath, that occurs at the longer immersion time. There is also the possibility that applying the TCP coating to dry rather than wet substrate surfaces contributes to the variability. Taken together, all the electrochemical parameters indicate that both the new and traditional TCP conversion coatings provide equivalent barrier-layer protection to the alloy and function as both an anodic and cathodic inhibitor. Importantly, the electrochemical data, with the exception of the more noble $E_{pit}$ for TCP-1, are similar for the two TCP coatings indicating an equivalent level of corrosion protection is provided by both.

*Salt-spray exposure*

The electrochemical data are only predictive of the corrosion resistance provided by the conversion coatings. Therefore, accelerated degradation testing was also performed to evaluate how the two TCP coatings inhibit corrosion. Neutral salt-spray (NSS) testing (ASTM B117) was performed to accomplish this. The test was for 14 days or 336 h in a 5 wt.% NaCl fog at 35°C. The testing followed guidelines in MIL-DTL-81706B, Chemical Conversion Materials for Coating Aluminum and Aluminum Alloys. Both TCP-coated specimens showed no visible corrosion damage (dissolution, pitting, or discoloration) after 14 days. Figure 3.6 presents photographs of TCP-coated AA2024-T3 specimens before and after the 14-day exposure. Photographs are also shown for the uncoated specimen before and after just 3 days of exposure due to widespread corrosion damage that developed. The absence of corrosion during this test period is consistent with the predictions of the electrochemical data for the TCP-coated specimens (i.e., suppressed currents and increased $Z_{0.01\ \mathrm{Hz}}$ values). Both TCP conversion coatings provided excellent stand-alone protection during this accelerated degradation test.

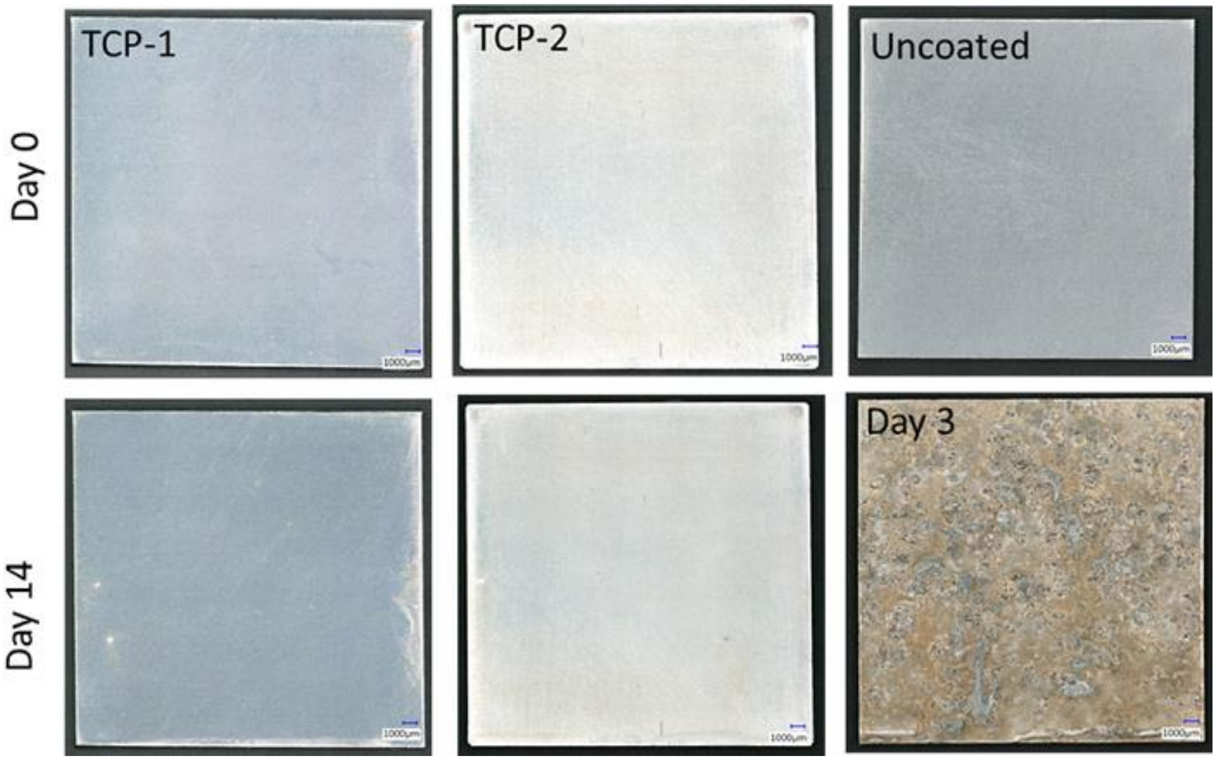

**Figure 3.6.** Photographs of TCP-1 (left), TCP-2 (middle) and uncoated (right) AA2024-T3 specimens before (top) and after (bottom) a 14-day neutral salt-spray (NSS) exposure. Photographs are shown for an uncoated AA2024 specimen after just 3 days of exposure as widespread corrosion damage developed. Full specimen and photograph dimensions are 1 in$^2$.

Post-mortem analysis of the salt-spray exposed specimens was performed by recording the weight loss and using digital optical microscopy to probe for material loss and corrosion damage across the surface. Table 3.2 presents data for weight loss, and pit depth and pit number for the three specimen types. The latter two parameters were determined by microscopy. There is an equivalent level of minor weight loss for the two TCP-coated specimen types after 14 days. This weight loss, however, is primarily due to dissolved alloy around the exposed edges as no corrosion damage was visible on the coated panel surfaces away from the edges. The edges were not masked off during the salt-spray exposure. The percentage weight loss for both coated specimens after 14 days is 10x lower than the loss observed for the uncoated specimen after just 3 days. These results are consistent with published data for the stand-alone corrosion resistance of aluminum alloys coated with other commercial TCP coatings.[44]

**Table 3.2.** Weight loss, pit depth and pit number density for TCP-coated AA2024-T3 specimens after a 14-day neutral salt-spray (NSS) exposure. Data are presented for the uncoated specimens after just a 3-day exposure. Data are presented as mean ± std. dev. (n = 3 specimens of each type). Digital optical microscopy was used to determine the pit depth and density. The weight loss for the coated specimens is mainly from the exposed edges. *Indicates statistically significant difference in the mean values from uncoated controls ($p \leq 0.05$). Analysis performed by Student's T-test.

| | TCP-1 | TCP-2 | Uncoated |
|---|---|---|---|
| Weight loss (%) | 0.01 ± 0.01* | 0.02 ± 0.01* | 0.3 ± 0.1 |
| Pit depth (μm) | 19 ± 16 | 51 ± 30 | 40 ± 18 |
| Pits (number/in$^2$) | 12 ± 4 | 13 ± 5 | Fully corroded |

All TCP-coated panels visually passed the 14-day NSS accelerated degradation test, as per MIL-DTL-81706B. Alloys protected with both the new and traditional TCP conversion coating were not corroded or discolored. However, digital optical microscopy revealed some minor microscopic pitting across the TCP-coated alloys after the salt-spray exposure. Table 3.2 presents nominal pit depth and the pit number measured across 1 in$^2$ specimens. Identifying small pits by digital microscopy is challenging. Pits, as do intermetallic particles, show up as dark spots in the optical micrographs due to their reflectivity differences as compared to the surrounding alloy. The values presented in the table for pit number are all the dark spots detectable in a micrograph over a 1 in$^2$ area. A very low number (ca. 10) of dark spots were detected on both of the TCP-coated specimens after the 14-day NSS. It is likely that some of these some of these spots (i.e., pits) were present on the alloy prior to coating and NSS exposure. The nominal pit depth is greater for TCP-2 than for TCP-1 but statistically there is no difference in the values due to the larger variability of the TCP-2 data. Again, this larger variability might be due to the fact that a 10-min immersion period was used rather than the recommended 5-min period. On the other hand, the uncoated specimen was severely corroded over the entire surface after just 3 days. The pit depths were determined by stitching together images recorded at different focal points.

An interesting observation was made on specimens many days after coating and exposure to the vacuum of the SEM and XPS instruments. Figure 3.7 presents SEM electron micrographs for (A) TCP-1 (10k magnification, 5 μm scale bar) and (B) TCP-2 (5k magnification, 10 μm scale bar) coated AA2024-T3 specimens. The immersion time for both coatings was 10 min. The micrograph for the TCP-1 coated specimen reveals the white coating precipitates (aggregates) decorating the surface with a pit in the center of the imaged area. With the exception of a few locations where cracking is observed, the TCP-1 conversion coating is intact and adhering to the alloy surface. In contrast, TCP-2 has more cracking and coating detachment from the surface. Larger segments of the coating are seen to be peeling away from the alloy. This needs to be explored further but could indicate superior adhesion and lower defect formation for the new TCP conversion coating.

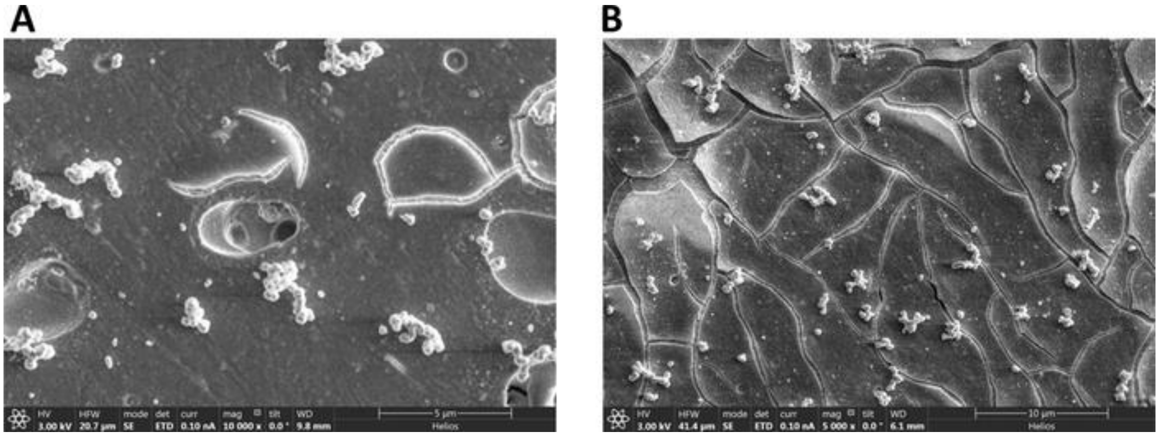

**Figure 3.7.** SEM micrographs of AA2024-T3 specimens coated with (A) TCP-1 and (B) TCP-2 after many days**.**

In the few places where pits were located on the TCP-coated specimens, digital optical microscopy was used to profile the surface topography around the defect. Figure 3.8 shows the color-coded 2D contour maps for selected regions on the uncoated and TCP-coated AA2024-T3 specimens before and after the NSS test. The test period for the TCP-coated specimens was 14 days while the period for the uncoated specimen was 3 days. The difference in height across the surface was recorded with zero being the deepest location. In other words, the circular blue spots in the "after" maps for TCP-1 and 2 are pits that formed during the exposure. In the two maps for the isolated pits found on the TCP-1 and TCP-2 coated specimens, the pit dimension in the lateral direction is 20–40 µm and in the vertical or depth dimension is on the order of 30 µm.

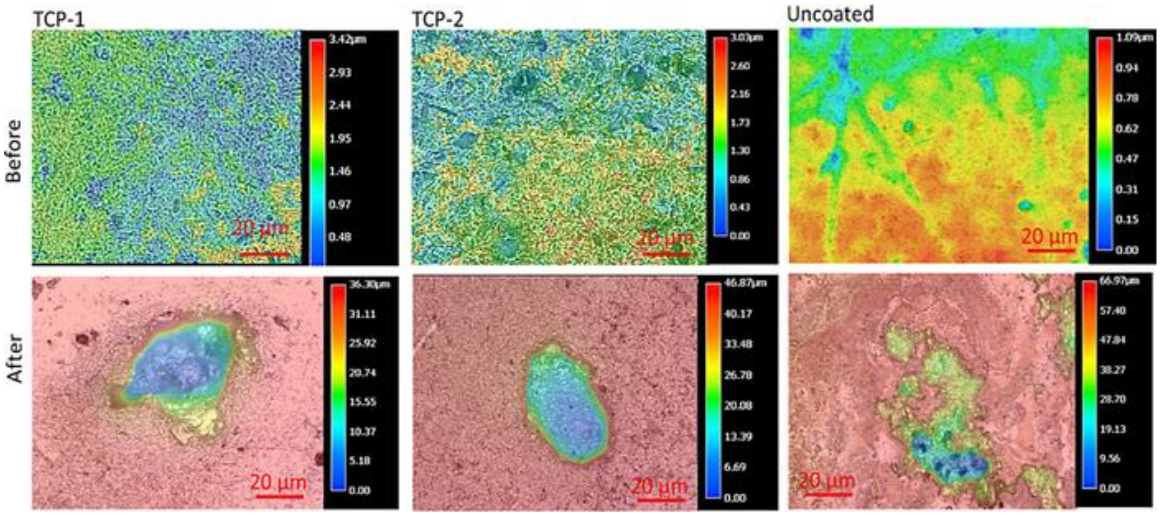

**Figure 3.8.** Color-coded surface contour maps of selected regions of TCP-1 coated (left), TCP-2 coated (center) and uncoated (right) AA2024-T3 specimens before (top) and after (bottom) neutral salt-spray (NSS) exposure. The exposure period for the TCP-coated specimens was 14 days while the period for the uncoated specimen was 3 days. A pit was located on each TCP-coated specimen and was profiled as shown in the "after" maps. The uncoated specimen was damaged all across the surface.

Figure 3.9 shows 3D plots of the surface topography around two small isolated pits detected on the two TCP-coated specimens after the 14-day NSS and around a more damaged region of the uncoated specimen, which was uniformly corroded after just 3 days. The uncoated specimen (right) has more extensive damage caused by the growth and coalescence of multiple pits.

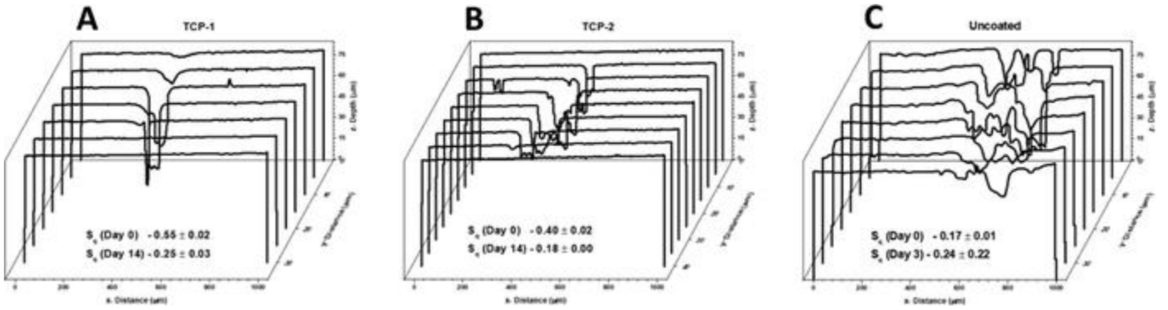

**Figure 3.9.** 3D plots showing the surface topography around two isolated pits on (A) TCP-1 coated, (B) TCP-2 coated and (C) uncoated AA2024-T3 specimens after the 14-day neutral salt-spray (NSS) exposure, and around a more damaged area of an uncoated specimen (right) after just 3 days of NSS. Surface roughness values ($S_q$), mean ± std. dev. (n = 5 areas of each type) recorded over a 50 µm × 1000 µm area, are reported in each map for Day 0 and 14.

The surface roughness ($S_q$, µm) for the specimen surfaces is included within the maps. Roughness was measured across a 50 µm × 1000 µm area on the specimen surface. Data from five areas on each specimen were pooled to produce the surface roughness values (mean ± std. dev.). The roughness decreased for both TCP-coated specimens after NSS exposure (0.55 to 0.25 µm for TCP-1, and 0.40 to 0.18 µm for TCP-2). This is due, in part, to the dissolution of coating particulates from the surface. In contrast, there is clearly increased surface roughness on the uncoated alloy after just 3 days of NSS exposure. The 3D plots show greater aluminum dissolution from the damaged area on the uncoated alloy than on the two TCP-coated alloys. It is clear that the pits are few in number but narrow and deep on the TCP-coated alloys with more lateral corrosion damage on the uncoated alloy – much more resembling uniform corrosion.

*Full immersion testing*

A second accelerated degradation test was performed to assess the corrosion protection provided by the two TCP coatings. Full immersion testing was performed on uncoated, TCP-1 and TCP-2 coated AA2024-T3 specimens for 14 days at 55°C in 3.5 wt% NaCl. Figure 3.10 shows camera photographs at Day 0 (a,d,g), 7 (b,e,h) and 14 (c,f,i) for the three specimens. There is no visible damage on either of the TCP-coated specimens indicative of an equivalent level of corrosion protection under these conditions. In contrast, there are large pitted regions and significant surface roughening on the uncoated specimen that develops within the first 7 days and becomes more severe after 14 days. Visual inspection revealed no signs of coating discoloration or corrosion damage of any kind on the TCP-coated specimens. The absence of corrosion during this test period is consistent with the predictions of the electrochemical data for the TCP-coated specimens (e.g., suppressed currents and increased $Z_{0.01\ \mathrm{Hz}}$ values). The results indicate that both TCP conversion coatings provide an equivalent level of protection during this accelerated degradation test as was the case during the 14-day NSS exposure.

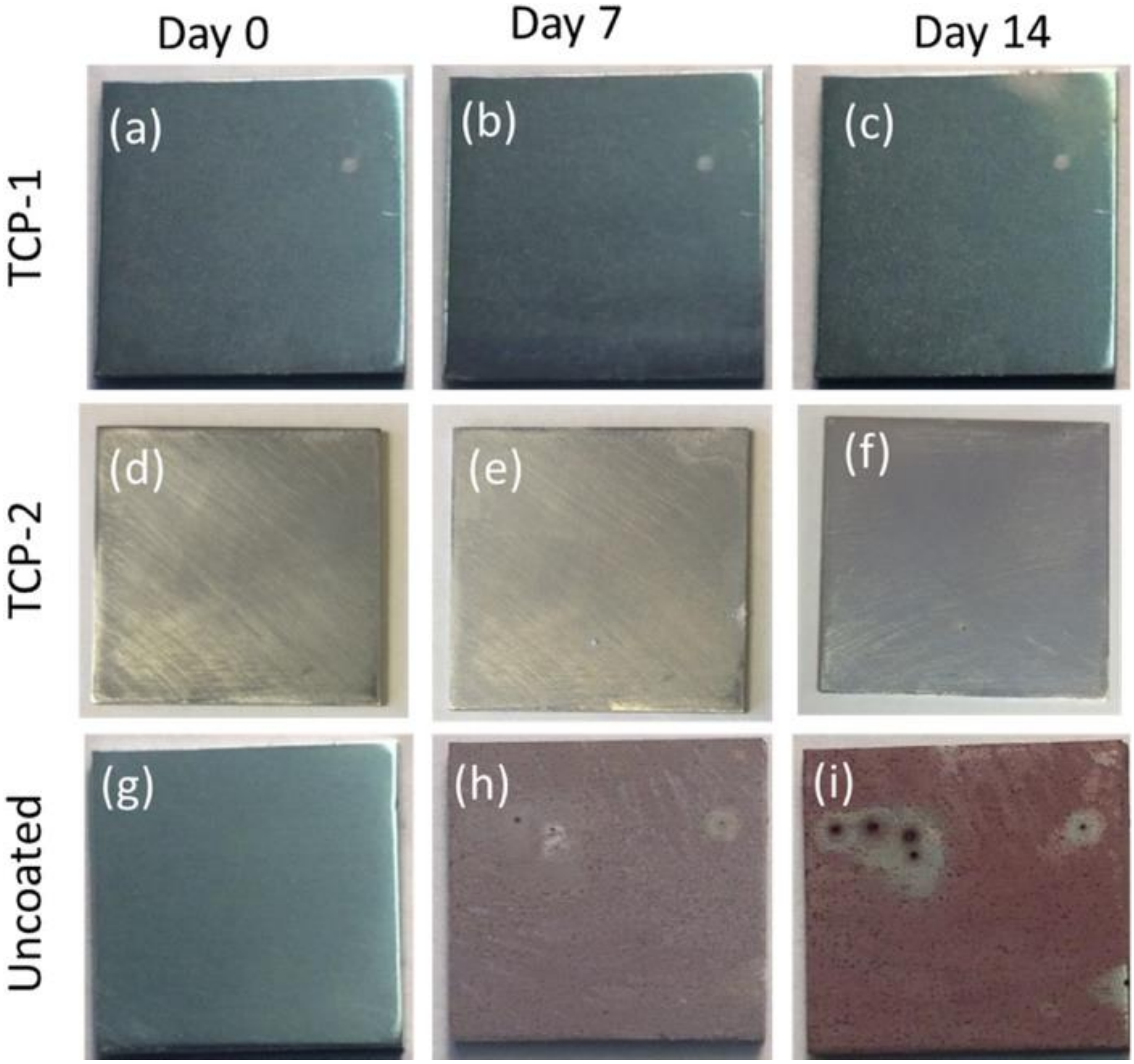

**Figure 3.10.** Camera photographs at Day 0, 7, and 14 for a TCP-1-coated AA2024-T3 specimen (first row, a-c), a TCP-2-coated specimen (middle row, d-f) and an uncoated (degreased and deoxidized) specimen (lower row, g-i) after 14 days of full immersion in 3.5 wt% NaCl at 55°C. The dimensions of the specimens were 1cm$^2$.

Figure 3.11 shows digital optical micrographs of TCP-coated (left and middle) and uncoated (right) AA2024-T3 specimens after 14 days of full immersion in 3.5 wt% NaCl at 55°C. There is no detectable damage on either of the TCP-coated specimens after this immersion period, whereas there is significant pitting (dark spots) and roughening of the uncoated specimen. These data indicate that TCP-1 and TCP-2 provide equivalent stand-alone corrosion protection to this alloy during this full immersion test.

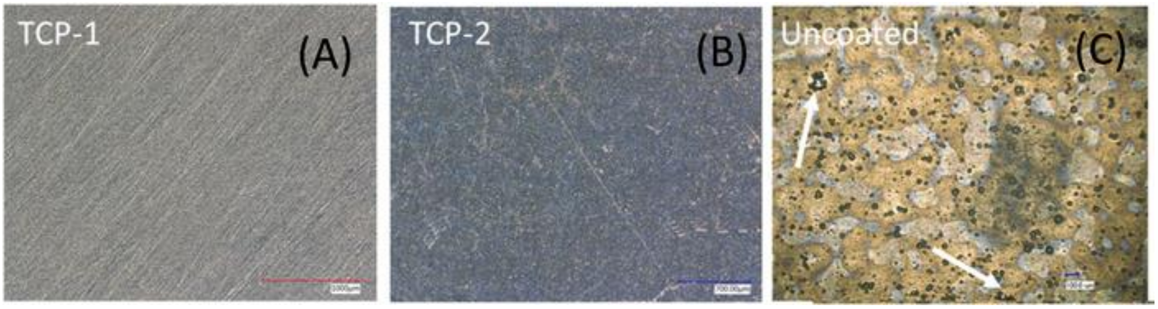

**Figure 3.11.** Digital optical micrographs of (A) TCP-1-coated, (B) TCP-2-coated and (C) an uncoated AA2024-T3 specimen after 14 days of full immersion in 3.5 wt% NaCl at 55°C. The arrows on (C) indicate pits formed on the uncoated alloy during the test. The scale bars and micrograph dimensions are (A) 1000 µm and 0.30 × 0.37 $cm^2$, (B) 700 µm and 0.30 × 0.38 $cm^2$, and (C) 100 µm and 0.22 × 0.27 $cm^2$.

The data presented herein so far have all been for specimens prepared and conversion coated in our laboratory. It is important to verify that the results seen for specimens coated in-house are in agreement with the results for specimens prepared by a professional coater. Figure 3.12 shows camera photographs of 3 in. × 10 in. AA2024-T3 specimens immersion coated by CHEMEON with TCP-1 for (A) 5, (B) 10 and (C) 20 min after exposure to a 14-day NSS. None of the specimens showed any visible pitting or other corrosion damage. The results validate the quality of the coatings applied in our laboratory. In fact, we have compared the performance of our coated alloy specimens with alloys coated by several certified coating houses. In all cases, no differences have been observed in the corrosion resistance and coating performance.

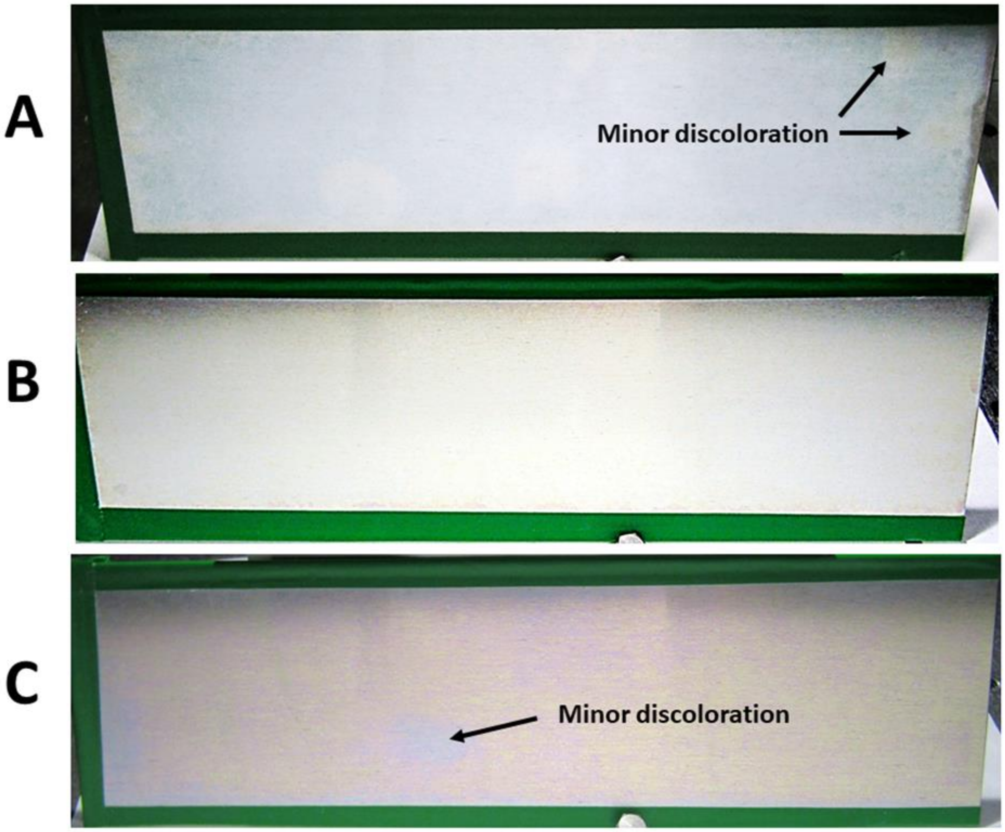

**Figure 3.12.** Camera photographs of TCP-1 coated AA2024-T3 panels immersion coated for (A) 5, (B) 10 and (C) 20 min after exposure to a 14-day neutral salt-spray according to ASTM B117. The panel dimensions are 3 in. x 10 in.. The edges were masked off with corrosion-resistant tape during the salt spray exposure.

Experiments were performed to study how the two TCP conversion coatings protect the underlying aluminum alloy when an artificial defect is introduced. The defect was introduced in the form of scribes in an "X" pattern across the specimen. The scribes were 100 μm wide by about 50 μm deep and were introduced after immersion coating the AA2024-T3 alloy with both TCP coatings. Figure 3.13 presents camera photographs of scribed areas before and after a 7-day NSS test. As was the case for the unscribed specimens, there was no damage observed across the panel outside of the scribes. This indicates good coating adhesion and corrosion protection.

Inspection of the scribed regions indicates little scribe creep or undercutting of the coating. For both TCP conversion coatings, there was little corrosion damage in and around the scribes. In a couple of places; however, some minor pitting in the scribe and scribe widening were observed. These locations are demarcated in the photographs.

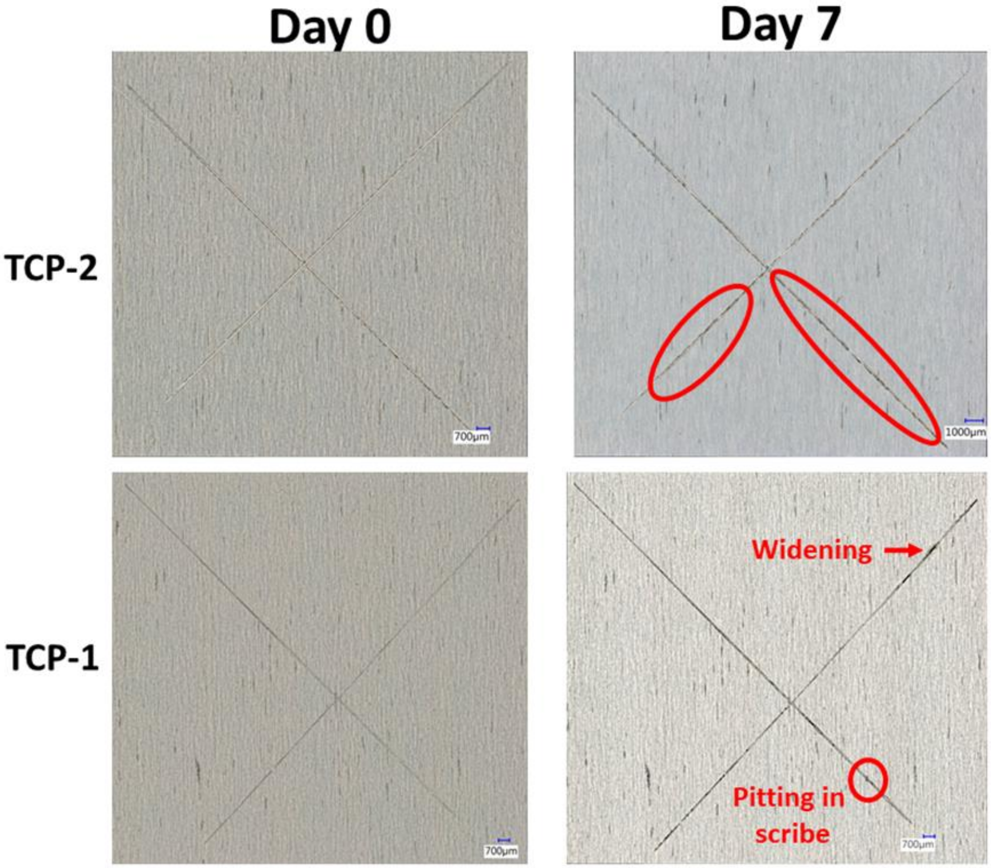

**Figure 3.13.** Camera photographs of AA2024-T3 specimens immersion coated with TCP-1 (bottom panels) and TCP-2 (upper panels) before and after exposure to a 7-day neutral salt spray according to ASTM B117. The micrographs are *ca.* 1.6 cm x 1.6 cm. The scale bar in each micrograph is 700 µm.

Figure 3.14 shows a higher magnification digital micrograph of a scribed section on an AA2024-T3 specimen immersion coated with TCP-1 after a 7-day NSS exposure. This scribed area is representative of most areas on the exposed coated specimens. Along the outer edges of the scribe, one can see the residual alloy (i.e., raised features) associated with the scribing process. The scribe width is 100 μm and there is no evidence for any significant scribe creep or undercutting of the coating due to corrosion along the scribe wall. There is some corrosion product formation in the base of the scribe as indicated by the darker and lighter blue regions. In summary, both TCP coatings commercially applied, like the in-house coatings, provide excellent stand-alone corrosion protection to the underlying aluminum alloy around artificially induced defects.

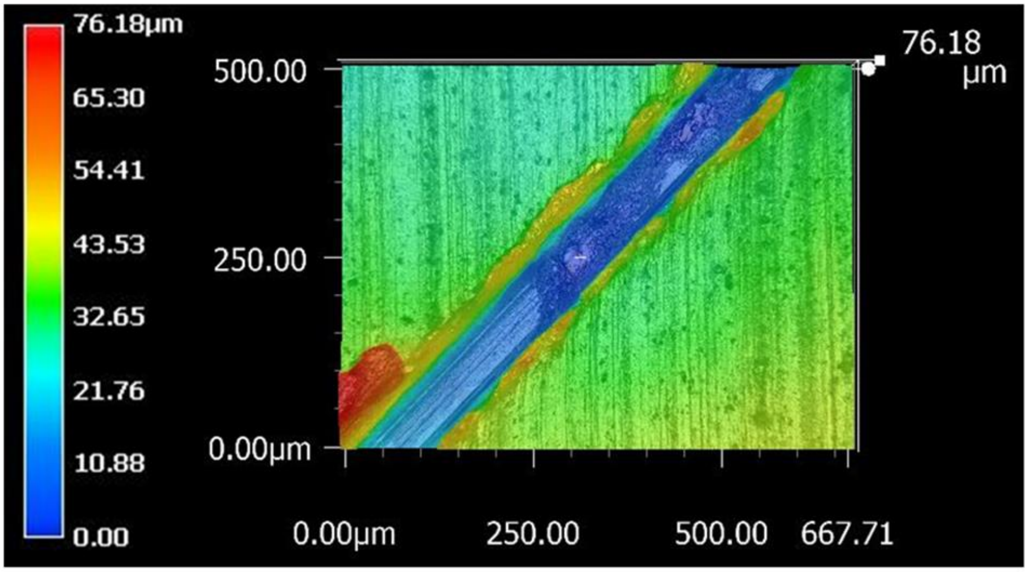

**Figure 3.14.** Digital micrograph of a scribe on AA2024-T3 coated with TCP-1 after exposure to a 7-day neutral salt spray according to ASTM B117.

## 3.5 Discussion

The results from this research are important scientifically because they demonstrate that this new trivalent chromium process coating, TCP-1 (TCP-NP), that requires no conventional deoxidation or etching surface pretreatment of the aluminum alloy prior to application, provides an equivalent level of corrosion protection as compared to standard TCPs that are commercially available. The practical benefits of TCP-1 are (i) no need for a separate deoxidation step thus eliminating the need for a process tank, (ii) a reduction in the volume of hazardous waste that must be monitored and disposed of and (iii) a reduction in the overall component processing time. The work reported on herein is the first comprehensive comparison study of the new TCP-1 with an existing commercial TCP coating, TCP-2 (TCP-HF).

TCP-1 coatings formed by immersion deposit over all areas of the aluminum alloy surface with some coating enrichment or increased coverage on and around intermetallic phases. XPS depth profiling data indicates that the TCP-1 coating has a biphasic structure with an outer hydrated zirconia and chromium hydrated layer and chromium hydroxide layer and a fluoride-rich interfacial layer. The maximum chromium content is ca. 6 at. % and the maximum fluoride concentration is ca. 13 at. %. The overall coating thickness for a 10 min immersion at room temperature is estimated to be 160 nm. This composition with depth and coating thickness are similar to TCP-2 and other commercial TCP coatings.[41,42,44]

The electrochemical data indicate that the new TCP-1 coating provides both anodic and cathodic protection to the alloy. Nominal OCP values are unchanged relative to uncoated controls. Anodic and cathodic currents are suppressed 10–100× by the coating as compared to uncoated controls. $E_{pit}$ values are shifted considerably positive and the low frequency impedance, $Z_{0.01\ Hz}$, is 200× higher than for uncoated controls. The electrochemical data for TCP-1 are very consistent with other commercial TCP variants.[41,42,44] TCP, originally developed by NAVAIR (U.S. Naval Air Systems Command), is the leading replacement candidate for the legacy chromate conversion coating. There are several commercial variants of TCP available, all of which have slightly different chemical compositions. Therefore, in our opinion, each TCP should be treated as an individual coating system and studied independently.

Accelerated degradation testing, both 14-day NSS and full immersion, revealed that TCP-1 and TCP-2 both provide excellent stand-alone corrosion protection to AA2024-T3. Visual observations of the panels and the weight loss data confirm that the laboratory electrochemical measurement data are good predictors of how the TCP coating will perform during these accelerated degradation tests. Finally, another important finding from the work is the fact that the performance of our in-house coated samples is equivalent to the performance of coatings applied by commercial entities.

## 3.6 Conclusions

Material characterization, electrochemical and accelerated degradation test data are reported on for a non-traditional (TCP-1) and a conventional (TCP-2) trivalent chromium process conversion coating. The performance of the two commercial coatings was compared on AA2024-T3. Key findings from the work are summarized below.

1. TCP-2, formed by immersion on degreased and deoxidized AA2024-T3, and TCP- 1, formed on degreased-only specimens, cover all regions of the alloy surface. The mechanism of formation and the time dependence of the coating formation is similar for both conversion coatings based on the alloy OCP vs. time profiles recorded during the immersion.
2. XPS depth profiles revealed similar chemical compositions of the two conversion coatings with depth. The apparent thickness of TCP-2 (~200 nm) is greater than the thickness of TCP-1 (~160 nm). Both conversion coatings consist of a biphasic structure with the outer 40–80 nm of the coating consisting of hydrated $ZrO_2$ and $Cr(OH)_3$ at concentrations of 20–25 at. % for Zr and 6 at. % for Cr. The interfacial region is a fluoride-rich fluoroaluminate layer that is ca. 100 nm thick.

3. Anodic current for alloy dissolution and cathodic current for dissolved oxygen reduction were equivalently suppressed by a factor of 10–100× by both TCP coatings, as compared to the uncoated alloy in naturally aerated 0.5 M $Na_2SO_4$ + 0.01 M NaCl. $E_{pit}$ for AA2024-T3 alloys coated with both TCP coatings was shifted significantly more positive as compared to the value for the uncoated alloy, which undergoes stable pit formation at potentials near the OCP. $E_{pit}$ for TCP-2 coated specimens was $\sim -0.2$V while most of the TCP-1 coated specimens showed no stable pit formation below 0.5 V.
4. The nominal low frequency impedance values, $Z_{0.01\ Hz}$ (i.e., polarization resistance), in naturally aerated 0.5 M $Na_2SO_4$ + 0.01 M NaCl was 200× greater for TCP-1 and 100× greater for TCP-2-coated alloys, as compared to the uncoated control.
5. A 14-day continuous NSS exposure produced no corrosion damage on alloys coated with both TCP-1 and 2. Both TCP conversion coatings provided equivalent levels of stand-alone corrosion resistance under these test conditions. In contrast, the uncoated alloy experienced severe corrosion over the entire surface after just 3 days. Weight loss data and digital optical micrograph analysis confirm the corrosion resistance.
6. Both TCP coatings provided excellent corrosion resistance to AA2024-T3 during a 14-day full immersion test in 3.5 wt% NaCl at 55°C. Weight loss data confirmed the corrosion resistance. The accelerated degradation test results are consistent with the predictions from laboratory electrochemical data.

### 3.7 Acknowledgments

We acknowledge Craig Matzdorf (NAVAIR) for his comments and suggestions regarding the work. The authors would like to thank CHEMEON Surface Technology for providing funding for this research. Some aspects of this work were also supported by a grant from the Office of Naval Research, Sea-Based Aviation Program, #N00014-15-1-2005. Program Manager: William Nickerson.

# REFERENCES

1. A. Heinz, A. Haszler, C. Keidel, S. Moldenhauer, R. Benedictus, and W. S. Miller, Recent Development in Alumininium Alloys for Aerospace Applications, *Mater. Sci. Eng.*, 280, 102 (2000).

2. M. Nakai and T. Eto, New Aspect of Development of High Strength Aluminum Alloys for Aerospace Applications, *Mater. Sci. Eng.*, 285, 62 (2000).

3. J. C. Williams and E. A. Starke Jr., Progress in Structural Materials for Aerospace Systems, *Acta Materialia*, 51, 5775 (2003).

4. R. L. Twite and G. P. Bierwagen, Review of Alternatives to Chromate for Corrosion Protection of Aluminum Aerospace Alloys, *Progress in Organic Coatings*, 33, 91 (1998).

5. R. G. Buchheit Jr, J. P. Moran, and G. E. Stoner, Localized Corrosion Behavior of Alloy 2090- The Role of Microstructureal Heterogeneity, *Corrosion*, 46, 610 (1990).

6. P. Campestrini, E. P. M. van Westing, H. W. van Rooijen, and J. H. W. de Wit, Relation Between Microstructural Aspects of AA2024 and its Corrosion Behaviour Investigated Using AFM Scanning Potential Technique, *Corrosion*, 42, 1853 (2000).

7. Q. Meng and G. S. Frankel, Effect of Cu Content on Corrosion Behavior of 7xxx Series Aluminum Alloys, *J. Electrochem. Soc.*, 151, B271 (2004).

8. Q. J. Meng and G. S. Frankel, Characterization of Chromate Conversion Coating on AA7075-T6 Aluminum Alloy, *Surf. Int. Anal.*, 36, 30 (2004).

9. M. W. Kendig, A. J. Davenport, and H. S. Isaacs, The Mechanism of Corrosion Inhibition by Chromate Conversion Coatings from X-ray Absorption Near Edge Spectroscopy (Xanes), *Corros. Sci.*, 34, 41 (1993).

10. J. Zhao, G.S. Frankel, and R. L. McCreery, Corrosion Protection of Untreated AA-2024-T3 in Chloride Solution by a Chromate Conversion Coating Monitored with Raman Spectroscopy, *J. Electrochem, Soc.*, 145, 2258 (1998).

11. O. Lunder, J. C. Walmsley, P. Mack, and K. Nisancioglu, Formation and Characterization of a Chromate Conversion Coating on AA6060 Aluminium, *Corros. Sci.*, 47, 1604 (2005).

12. L. Xia and R. L. McCreery, Chemistry of a Chromate Conversion Coating on Aluminum Alloy AA2024-T3 Probed by Vibrational Spectroscopy, *J. Electrochem. Soc.*, 145, 3083 (1998).

13. E. Akiyama, A. J. Markworth, J. K. McCoy, G. S. Frankel, L. Xia, and R. L. McCreery, Storage and Release of Soluble Hexavalent Chromium from Chromate Conversion Coatings on Al Alloys: Kinetics of Release, *J. Electrochem. Soc.*, 150, B83 (2003).

14. J. LaScala, "Non-chromate/No-VOC coating systems for DoD applications", (WP-1521), Final Report, SERDP, 2009.

15. M. Costa, Toxicity and Carcinogenicity of Cr(VI) in Animal Models and Humans, *Critical Rev. Toxicol.*, 27, 431 (1997).

16. S. Mishra and R. N. Bharagava, Toxic and Genotoxic Effects of Hexavalent Chromium in Environment and its Bioremediation Strategies, *J. Environ. Sci. Health C. Environ. Carcinog. Ecotoxicol. Rev.*, 34, 1 (2016).

17. N. N. Voevodin, N. T. Grebasch, W. S. Soto, L. S. Kasten, J. T. Grant, F. E. Arnold, and M. S. Donley, An Organically Modified Zirconate Film as a Corrosion-Resistant Treatment for Aluminum 2024-T3, *Progress in Organic Coatings*, 41, 287 (2001).

18. P. Campestrini, H. Terryn, A. Hovestad, and J. H. W. de Wit, Formation of a Cerium-Based Conversion Coating of AA2024: Relationship with the Microstructure, *Surf. Coat. Technol.*, 176, 365 (2004).

19. S. Adhikari, K. A. Unocic, Y. Zhai, G. S. Frankel, J. Zimmerman, and W. Fristad, Hexafluorozirconic Acid Based Surface Pretreatments: Characterization and Performance Assessment, *Electrochim. Acta*, 56, 1912 (2011).

20. F. O. George, P. Skeldon, and G. E. Thompson, Formation of Zirconium-Based Conversion Coatings on Aluminium and Al-Cu Alloys, *Corr. Sci.*, 65, 231 (2012).

21. L. L. Li, B. W. Whitman, and G. M. Swain, Characterization and Performance of a Zr/Ti Pretreatment Conversion Coating on AA2024-T3, *J. Electrochem. Soc.*, 162, C279 (2015).

22. P. S. Coloma, U. Izagirre, Y. Belaustegi, J. B. Jorcin, F. J. Cano, and N. Lapeña, Chromium-free Conversion Coatings based on Inorganic Salts (Zr/Ti/Mn/Mo) for Aluminum Alloys Used in Aircraft Applications, *Appl. Surf. Sci.*, 345, 24 (2015).

23. L. L. Li, B. W. Whitman, C. A. Munson, R. Estrada, C. A. Matzdorf, and G. M. Swain, Structure and Corrosion Performance of a Non-Chromium Process (NCP) Zr/Zn Pretreatment Conversion Coating on Aluminum Alloys, *J. Electrochem. Soc.*, 163, C718 (2016).

24. C. A. Matzdorf, W. C. Nickerson, E. N. Beck, A. S. Schwartz, and J. L. Green, U.S. Pat. Application Publication, *Non-Chromium Coatings for Aluminum*, US2007/0095436 A1, May 3, 2007.

25. S. L. Suib, J. LaScala, W. Nickerson, A. Fowler, and N. Zaki, Determination of Hexavalent Chromium in NAVAIR Trivalent Chromium Process (TCP) Coatings and Process Solutions, *Metal Finishing*, 107, 28 (2009).

26. A. Iyer, W. Willis, S. Frueh, W. Nickerson, A. Fowler, J. Bames, L. Hagos, J. Escarsega, J. La Scala, and S. L. Suib, Characterization of NAVAIR Trivalent Chromium Process (TCP) Coatings and Solutions, *Plating and Surface Finishing*, 5, 32 (2010).

27. X. C. Dong, P. Wang, S. Argekar, and D. W. Schaefer, Structure and Composition of Trivalent Chromium Process (TCP) Films on Al Alloy, *Langmuir*, 26, 10833 (2010).

28. S. Dardona and M. Jaworowski, In situ Spectroscopic Ellipsometry Studies of Trivalent Chromium Coating on Aluminum, *Appl. Phys. Lett.*, 97, 181908 (2010).

29. L. L. Li, G. P. Swain, A. Howell, D. Woodbury, and G. M. Swain, The Formation, Structure, Electrochemical Properties and Stability of Trivalent Chrome Process (TCP) Coatings on AA2024, *J. Electrochem. Soc.*, 158, C274 (2011).

30. Y. Guo and G. S. Frankel, Characterization of Trivalent Chromium Process Coating on AA2024-T3, *Surf. Coat. Technol.*, 206, 3895 (2012).

31. Y. Guo and G. S. Frankel, Active Corrosion Inhibition of AA2024-T3 by Trivalent Chrome Process Treatment, *Corrosion*, 68, 045002 (2012).

32. L. L. Li, D. Y. Kim, and G. M. Swain, Transient Formation of Chromate in Trivalent Chromium Process (TCP) Coatings on AA2024 as Probed by Raman Spectroscopy, *J. Electrochem. Soc.*, 159, C326 (2012).

33. L. L. Li and G. M. Swain, Formation and Structure of Trivalent Chromium Process Coatings on Aluminum Alloys 6061 and 7075, *Corrosion*, 69, 1205 (2013).

34. L. L. Li, K. P. Doran, and G. M. Swain, Electrochemical Characterization of Trivalent Chromium Process (TCP) Coatings on Aluminum Alloys 6061 and 7075, *J. Electrochem. Soc.*, 160, C396 (2013).

35. L. L. Li and G. M. Swain, Effects of Aging Temperature and Time on the Corrosion Protection Provided by Trivalent Chromium Process Coatings on AA2024-T3, *ACS Appl. Mater. Interfaces*, 5, 7923 (2013).

36. J. T. Qi, T. Hashimoto, J. R. Walton, X. Zhou, P. Skeldon, and G. E. Thompson, Trivalent Chromium Conversion Coating Formation on Aluminum, *Surf. Coat. Technol.*, 280, 317 (2015).

37. J. Qi, T. Hashimoto, J. Walton, X. Zhou, P. Skeldon, and G. E. Thompson, Formation of a Trivalent Chromium Conversion Coating on AA2024-T351 Alloy, *J. Electrochem. Soc.*, 163, C25 (2016).

38. J. Qi, T. Hashimoto, G. E. Thompson, and J. Carr, Influence of Water Immersion Post-Treatment Parameters on Trivalent Chromium Conversion Coatings Formed on AA2024-T351 Alloy, *J. Electrochem. Soc.*, 163, C131 (2016).

39. X. Verdalet-Guardiola, J. P. Bonio, S. Duluard, B. Pori, and C. Blanc, Influence of the Alloy Microstructure and Surface State on the Protective Properties of Trivalent Chromium Coatings Grown on a 2024 Aluminium Alloy, *Surf. Coat. Technol.*, 344, 276 (2018).

40. T. K. Shruthi and G. M. Swain, Role of Trivalent Chromium on the Anti-Corrosion Properties of a TCP Conversion Coating on Aluminum Alloy 2024-T3, *J. Electrochem. Soc.*, 165, C103 (2018).

41. C. A. Munson and G. M. Swain, Structure and Chemical Composition of Different Variants of a Commercial Trivalent Chromium Process (TCP) Coating on Aluminum Alloy 7075-T6, *Surf. Coat. Technol.*, 315, 150 (2017).

42. C. A. Munson, P. Zutim, and G. M. Swain, Electrochemical Characterization of Different Variants of a Commerical Trivalent Chromium Process (TCP) Coating on Aluminum Alloy 7075-T6, *Corrosion*, 74, 50 (2018).

43. J. Qi, A. Nemcova, J. Walton, X. Zhou, P. Skeldon, and G. E. Thompson, Influence of Pre- and Post-Treatments on Formation of a Trivalent Chromium Conversion Coating on AA2024 Alloy, *Thin Solid Films*, 616, 270 (2016).

44. C. A. Munson, S. A. McFall-Boegeman, and G. M. Swain, Cross Comparison of TCP Conversion Coating Performance on Aluminum Alloys During Neutral Salt-Spray and Thin-Layer Mist Accelerated Degradation Testing, *Electrochim. Acta*, 282, 171 (2018).

45. L. L. Li, A. L. Desouza, and G. M. Swain, In situ pH Measurement During the Formation of Conversion Coatings on an Aluminum Alloy (AA2024), *Analyst*, 138, 4398 (2013).

46. X. Verdalet-Guardiola, J. P. Bonino, S. Duluard, B. Pori, and C. Blanc, Influence of the Alloy Microstructure and Surface State on the Protective Properties of Trivalent Chromium Coatings Grown on a 2024 Aluminium Alloy, *Surf. Coat. Technol.*, 344, 276 (2018).

47. Q. Boyer, M. R. O. Vega, C. D. Malfatti, S. Duluard, and F. Ansart, Correlation Between Morphology and Electrochemical Behavior of Chromium-Free Conversion Coatings foor Aluminum Alloys Corrosion Protection, *Surf. Coat. Technol.*, 351, 115 (2018).

48. A. Bund and S. Hesamedini, Trivalent Chromium Conversion Coatings, *J. Coat. Technol. Res.*, 16, 623 (2019).

49. T. K. Shruthi and G. M. Swain, Detection of $H_2O_2$ from the Reduction of Dissolved Oxygen on TCP-Coated AA2024—T3: Impact on the Transient Formation of Cr(VI), *J. Electrochem. Soc.*, 166, C3284 (2019).

# CHAPTER 4 -The Electrochemical Behavior of As-Prepared Aluminum Alloy A360 Produced by Selective Laser Melting Fabrication with and without a Trivalent Chromium Process Conversion Coating

Chapter adapted from *J. Electrochem. Soc.*, **169**, 121501 (2022), Copyright 2022, The Electrochemical Society

*Article: Jack W. Walton, Lucas Rice, Sarah McFall-Boegeman, and Greg M. Swain- The Electrochemical Behavior of As-Prepared Aluminum Alloy A360 Produced by Selective Laser Melting Fabrication with and without a Trivalent Chromium Process Conversion Coating*

## 4.1 Abstract

We report herein on the electrochemical behavior and corrosion resistance of as-prepared aluminum alloy, A360 ($AlSi_{10}Mg$), fabricated by additive manufacturing, with and without a trivalent chromium process conversion coating. Selective laser melting was the 3D printing process used for the alloy build. The corrosion suppression provided by the coating system was assessed through electrochemical measurements and accelerated degradation testing during a 14-day continuous neutral salt-spray exposure. The results indicate that the conversion coating can be formed by solution pretreating (degreasing and deoxidation) the alloy (X-Z plane perpendicular to the build plane) with its native surface roughness (as-prepared) followed by immersion for 10, 15 or 20 min in the coating bath. All three immersion times provide an equivalent level of corrosion protection to the alloy. The conversion coating suppresses both anodic and cathodic currents, increases the polarization resistance, and provides both anodic and cathodic corrosion protection to the as-prepared alloy. The conversion-coated specimens exhibit good stand-alone corrosion resistance during a 14-day neutral salt-spray exposure with corrosion

intensity values (g/m$^2$-year) ∼10× lower than values for the uncoated, as-prepared alloy specimens.

## 4.2 Introduction

Metal-based additive manufacturing (AM) technology enables the resource-efficient generation of lightweight components in a variety of geometric shapes from the bottom up. The manufacturing technology enables more efficient use of raw materials with less waste than traditionally machined parts. The layer-by-layer fabrication can, in principle, lead to materials with unique properties. Laser-power bed fusion, often referred to as selective laser melting (SLM), is commonly employed because of increased geometrical freedom as well as rapid near net shape production with acceptable roughness.[1–5] The SLM process can produce material densities of almost 100%.[5] Key material parameters to control for printing alloys by this method are the property profile of the feedstock powder (chemical composition, particle microstructure, and particle size) and the processing parameters (powder feed rate and layer thickness, laser scan speed and laser energy density).

Several types of metals in powder form can be used to create component parts by SLM. Fabricating metal components layer-by-layer increases design freedom and manufacturing flexibility, thereby enabling complex geometries and increased part customization. The mechanical properties as well as the corrosion resistance of these AM alloys are important to assess and control. It is also important to determine how these properties correlate with the density, microstructure, and elemental distribution of the material. In theory, superior strength and improved corrosion resistance can be imparted to AM alloys by virtue of the layer-by-layer build and control over the addition of alloying elements into the base metal matrix, as compared with the strength and corrosion resistance of the alloys prepared by traditional mixing in the molten state followed by heat treatment or cold working.[1–5]

Aluminum alloys are challenging to fabricate by SLM because of the high reflectivity of the metal.[6] This means greater laser energy is required to melt the metal. Additionally, the high reactivity of the metal with oxygen means the specimens must be fabricated in an inert environment of argon or nitrogen gas. In the family of aluminum alloys, A360 ($AlSi_{10}Mg$) is the one most often prepared by AM methods.[6–14] The traditional method for preparing this alloy is by die casting. There has been some published work describing the microstructure and mechanical strength of A360 alloys prepared by SLM in comparison with die-cast materials, but comparatively little research has been reported on the electrochemical behavior of these SLM alloys as-prepared and after surface finishing with coating systems.[8–10,13,14] Generally, the microstructure of alloys produced by different AM methods are distinct from those of alloys prepared by conventional methods such as wrought processing and die casting.[4] The AM processing variables control the material microstructure, density, and defect density (e.g., microvoids, pores and cracks). A360 has applications in aerospace due to its light weight, low thermal expansion coefficient, decent corrosion resistance and mechanical strength.[13] The mechanical hardness and tensile strength are largely controlled by the material density, which is influenced by the fluidity of the liquid and the depth of the melt pool (density) and the grain refinement strengthening that develops due to Si precipitation from the α-Al matrix.[6,13,14]

Metal alloys prepared by SLM processing possess a bumpy surface texture with roughness values in the tens of micrometer range. This is primarily due to balling and dross formation in the melt pool as well as surface artifacts from poorly sintered particles.[15] Since metal AM processes produce rough surfaces, secondary post-processing is required which increases production cost and time. Surface roughness can detrimentally affect appearance and mechanical behavior (e.g., fatigue life, wear resistance, etc.). The surface roughness of SLM-prepared materials can be minimized through proper selection of the processing parameters. These parameters include the laser power, laser scan speed (i.e., local heating and cooling rates), source powder composition, and powder layer thickness.

Aerospace aluminum alloys are commonly placed in service with a multilayer coating system (conversion coating + primer + topcoat) applied for corrosion mitigation. There is a technological need to fully transition away from legacy chromate-containing coatings to more environmentally friendly replacements. The leading replacement for the chromate conversion coating is the trivalent chromium process (TCP) conversion coating, originally developed by the Naval Air Systems Command (NAVAIR).[15–30] The coating consists of a biphasic structure when formed on various wrought aluminum alloys with a mixed $ZrO_2 \cdot nH_2O$ and $Cr(OH)_3$ outer layer and an aluminofluoride-rich interfacial layer.[17–19,22–24,26–30] Coating thicknesses when formed by immersion range from 100–300 nm. Little work, to date, has been performed to understand the electrochemical property differences between SLM processed and die-cast aluminum alloy A360 [8–10,31,32] and no research reported on how the electrochemical behavior of the SLM alloy is altered by a TCP conversion coating. There has been one recent publication by Revilla et al. describing the electrochemical behavior of AM A360 with and without a Zr-based conversion coating.[13] We address this knowledge gap and report herein on the electrochemical behavior and corrosion resistance of AM A360 alloy specimens with and without a TCP conversion coating. Electrochemical measurements and a 14-day neutral salt-spray exposure were used to evaluate the corrosion resistance. A goal of the work was to assess how effectively the conversion coating forms on and protects the as-prepared alloy specimens with their native surface roughness.

## 4.3 Experimental

### *AM metal fabrication*

The aluminum alloy A360 specimens used in the work were fabricated at Honeywell FM&T (KCNSC) by selective laser melting using a SLM®500 industrial 3D printer (SLM Solutions, Germany). The specimens were printed from a $AlSi_{10}Mg$ source alloy powder with a diameter ranging from 25–65 µm. Specifically, 10% of the particles were less in diameter than 26 µm, 50% less than 40 µm, and 90% less than 63 µm. According to ASTM B85 (Standard Specification for Aluminum Alloy Die Castings), A360 alloy has the following elemental composition (wt%): Cu (0.6), Mg (0.4–0.6), Fe (≤1.3), Sn (≤0.10), Ni (≤0.5), Zn (≤0.5), Mn (≤0.35), Si (9.0–10.0) and Al (balance).[32] The SLM processing involves melting and fusing metallic powders with a high-power laser beam scanned across the build surface. Once a layer of solid metal is created, the tray holding the specimen is lowered and powder is layered on top. This is followed by the laser-assisted melting and fusing of the particles in the build plane to form the new layer. The specimens used in this work were fabricated with two dimensions: 2.54 cm × 2.54 cm × 0.635 cm (thickness) and 5.08 cm × 5.08 cm × 0.635 cm (thickness). The feedstock metal powder was procured from a commercial source and possessed the following elemental composition (wt%): Si (9.86%); Mg (0.38%); Fe (0.10%); Ti, Ni, Cu, Pb, Sn and Cr (0.01%); and Zn and Mn (<0.1%). The SLM system uses 3D optics and four lasers (350 W and 1070 nm) to produce parts with a maximum build space of 500 × 250 × 365 mm. The inert gas used in the chamber during the specimen builds was argon for the purpose of limiting oxygen reactivity with the heated aluminum. The following parameters were used for part fabrication:

laser power = 350 W, hatch spacing = 130 μm, powder layer thickness = 30 μm, and laser scan velocity = 1650 mm/s. These parameters were selected based on prior work at KCNSC. No parameter variation was investigated in this study.

Post processing of the specimens consisted of wire electric discharge machining (EDM), media blasting, and cleaning. No thermal annealing was applied to the fabricated specimens. The wire EDM step removes the parts from the build plate. The media blast step helps remove semi-sintered particles from the specimen surface and provides a matte finish to the exterior. The A360 specimens were sand blasted at a pressure from 50–70 psi. Cleaning was then performed internally according to KCNSC standard practice in a spray booth. This consisted of five steps: (i) high pressure spray with detergent and rinse with water, (ii) ultrasonication in detergent followed by a water rinse, (iii) ultrasonication in detergent followed by a water rinse and then drying with a stream of nitrogen gas, (iv) vacuum oven drying, and (v) packaging the cooled specimens into nylon bag for shipment to MSU. Throughout the manuscript, we refer to these specimens as "as-prepared."

*Chemical reagents*

Turco 6849 (20% v/v, Henkel Corp., Madison Heights, MI) was the commercial degreasing solution used. Turco Liquid Smut-Go (20% v/v, Henkel Corp., Madison Heights, MI) served as the deoxidizing solution. Bonderite T-5900 RTU (Henkel Corp., Madison Heights, MI) was the commercial TCP coating bath studied. Sodium sulfate ($Na_2SO_4$), sodium chloride (NaCl), sodium permanganate ($KMnO_4$) and sodium hydroxide (NaOH) were procured from Sigma Adrich (St. Louis, MO). All chemicals were technical or reagent grade quality, or better, and used without additional purification. All solutions were prepared with ultrapure water (Barnstead E-Pure) having a resistivity of >17 MΩ-cm.

*Vickers hardness measurements*

For microhardness testing, a specimen was smoothed by abrading on wet 1500 grit $Al_2O_3$ grinding paper followed by polishing with 0.3 μm alumina powder (Buehler) slurried in ultrapure water on a felt pad. Each step was followed by copious rinsing with and ultrasonic cleaning in ultrapure water for 20 min to remove polishing debris. The microhardness test was performed according to ASTM E384–17 (Standard Test Method for Microindentation Hardness of Materials).[33] A diamond pyramid tip indenter was used to apply indentations at five different spots across a representative specimen using a load of 0.5 kg. The indentation time was 15 s. Each indentation was evaluated for symmetry and defects. The diagonals of the indentation were measured, and the hardness was calculated.

*Surface pretreatment*

As-prepared A360 alloy specimens were pretreated prior to the electrochemical testing and microscopy measurements by solution processing in two steps. The specimens were first cleaned by immersion in an alkaline degreaser (Henkel Turco 6849) for 10 min at 55 °C followed by a 2-min flowing city tap water rinse. The degreased specimens were then deoxidized (Henkel Turco Liquid Smut-Go NC) by immersion for 2 min at room temperature. The samples were rinsed again in flowing city tap water for 2 min, dried with a low pressure nitrogen gas flow, and tested immediately thereafter. These degreasing and deoxidizing industrial solutions were selected based on prior work in our laboratory with their use to pretreat other wrought aluminum alloys.[19,23,25,29] In most cases, no abrading or polishing was performed to smooth the surface texture prior to the solution processing.

For the conversion coating with TCP, the A360 specimens were first cleaned and deoxidized, as described above. The specimens were then immersion coated in a TCP bath

(Bonderite T-5900 RTU) for 10, 15, or 20 min at room temperature. After immersion coating, the specimens were immersed in city tap water for 2 min followed by a 30 s immersion rinse in ultrapure water (>17 MΩ-cm). Finally, the TCP-coated specimens were aged in the ambient laboratory air for at least 24 h before any follow-up testing.

For some microscopy studies, the as-prepared A360 alloy specimens were abraded and polished to smooth the surface making for easier visualization of features, such as microvoids, cracks, pores, grain boundaries, and second-phase particles. These specimens were first mechanically abraded by hand on wet 1500 grit $Al_2O_3$ grinding paper and then hand polished with 0.3 μm alumina powder slurried in ultrapure water on a felt pad. Both steps were followed by rinsing with and ultrasonic cleaning in ultrapure water for 20 min to remove polishing debris. The polished specimens were then solution processed by degreasing in Turco 6849 for 10 min at 55 °C and rinsing in flowing city tap water for 2 min As a final step, the smoothed and cleaned specimens were tint etched by immersion in Weck's reagent for 30 s at room temperature followed by rinsing with ultrapure water. 34,35 The Weck's reagent used consisted of 4 wt% $KMnO_4$ and 1 wt% NaOH.

### *Digital optical microscopy*

The surface texture of the as-prepared A360 specimens, after surface treatment, after TCP coating, and after neutral salt-spray exposure was assessed using a Keyence VHX-6000 digital optical microscope. Low resolution images were collected with a 20–200× zoom lens (VH-Z20). Images of different regions and focal planes were stitched together to produce a 3D profile of the entire specimen surface. High resolution images were collected with a 500–5000× zoom lens (VH-Z500) and used to quantitatively assess the surface texture and other structural features. The topographical data were analyzed to calculate the surface roughness and maximum peak-to-valley distance. For this analysis, five spots were randomly selected on any one specimen in a grid pattern. At least five different as-prepared specimens were used in the measurements.

*Scanning electron microscopy/energy dispersive X-ray spectroscopy*

Scanning electron microscopy (SEM) and energy dispersive X-ray spectroscopy (EDS) were performed using a field emission electron microscope (JOEL 7500F) equipped with an Oxford EDS system for elemental analysis. The measurements were performed to assess the elemental composition across the alloy surface (locations of Si and Mg) and the location of TCP coating elements (Zr, Cr, F, and O). The secondary and backscattered electron micrographs were collected using an accelerating voltage of 15 kV, and a probe current of 10 pA, and a working distance between 8 and 10 mm. The EDS analysis was performed using the same accelerating voltage and working distance used to collect the electron micrographs. The measurements were performed using microscopes at the Center for Advanced Microscopy (MSU).

*Electrochemical measurements*

The uncoated and TCP-coated alloy specimens were electrochemically characterized using open circuit potential (OCP) measurements, full frequency electrochemical impedance spectroscopy (EIS) measurements at the OCP, linear polarization resistance (LPR) measurements, and potentiodynamic polarization curves. The electrolyte used in all the measurements was naturally aerated 0.5 M $Na_2SO_4$ + 0.01 M NaCl at room temperature. All electrochemical measurements were conducted in a 1 $cm^2$ flat cell (Biologic Science Instruments) using a computer-controlled electrochemical workstation (Gamry Instruments, Inc., Reference 600, Warminster, PA). An aluminum alloy specimen was mounted in the cell against a Viton® O-ring that defined the exposed geometric area, 1 $cm^2$. All currents reported herein are normalized to this geometric area. The counter electrode was a Pt flag, and the reference was a home-made Ag/AgCl electrode (4 M KCl, $E^0$ = +0.197 V vs NHE) housed in a Luggin capillary with a cracked glass tip. The OCP was measured for 1 h prior to the potentiodynamic and EIS measurements. EIS data were recorded at the stable OCP using a 10 mV sine wave with 7 points per frequency decade collected. A range from $10^5$ to $10^{-2}$ Hz was employed to determine the frequency dependence of the real (ohmic) and imaginary (capacitive) components of the total impedance. The experimental data were fit to an appropriate equivalent circuit using ZView software (version 3.5 h) to determine the numerical magnitudes of the circuit components (i.e., the electrochemical parameters). The measurements were generally repeated with at least 3 specimens of each type (uncoated and TCP-coated) to assess reproducibility.

Linear polarization resistance (LPR) measurements were performed using linear sweep voltammetry over a potential range of ±10 mV vs OCP. The scan rate was 1 mV/s. The reciprocal slope of the i-E curves is the polarization resistance, $R_p$ $\left(R_p = \frac{\Delta E}{\Delta i} \text{ as } \Delta E \rightarrow 0\right)$. Potentiodynamic polarization curves were recorded from ±0.020 V vs OCP to either a positive limit of 0.5 V for the anodic curves or to a negative limit of −1.2 V for the cathodic curves. The scan rate was 1 mV/s[1]. These curves provide insight on the anodic (oxide formation and localized pitting) and cathodic (oxygen reduction) reaction rates as a function of electrode potential around the OCP. The EIS data were fit using the equivalent electrical circuit presented in Figure 4.1.[22] The two RC components are nested one within the other to represent a defective coating. $R_e$ is the equivalent series resistance dominated by the bulk electrolyte solution resistance. $R_{po}$ and $R_p$ represent the resistance of the electrolyte movement in the pores and the polarization resistance of the metal to interfacial electron-transfer reactions. $CPE_{co}$ is a constant phase element that represents the potential-dependent coating capacitance, and $CPE_{dl}$ represents the potential-dependent electrolyte-metal interfacial capacitance in the coating defects and pores.

The CPE components are expressed by mathematical parameters, Q, and α. Q is the quasi-capacitance and α is the so-called homogeneity factor (α = 1 for an ideal capacitor).

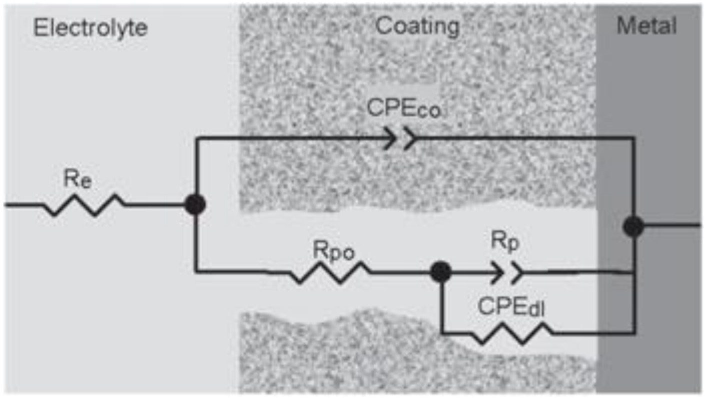

**Figure 4.1.** Equivalent circuit used for fitting the full frequency electrochemical impedance data for the A360 specimens with and without a TCP conversion coating.[22] The coating refers to the oxide layer on the unmodified and the conversion coating on the TCP-modified alloys.

The impedance of a constant phase element, CPE-Q, is given by the following equation,[36]

$$Z_{CPE} = \frac{1}{\left(Q(j\omega)\right)^{n}} \tag{9}$$

in which Q is the CPE constant, j is the imaginary unit $(j = \sqrt{-1})$, ω is the angular frequency (rad/s) and n is known as the dispersion coefficient of the CPE. The CPE is an element that accounts for the non-ideal capacitance of the native oxide or the TCP coating surface layer. Mathematically, an ideally behaved capacitance would have a value of $n = 1$, and a capacitance with nonideal behavior would have values $n < 1$. Statistical analysis was performed using replicate ($n = 3$ for each) measurements of uncoated and TCP-coated alloy specimens.

### *Neutral salt-spray test*

The uncoated and TCP-coated A360 specimens were exposed to a continuous salt spray for 14 days according to ASTM B117 (Standard Practice for Operating Salt Spray (Fog) Apparatus).[37] A 5 wt% NaCl salt solution was continuously sprayed in the test chamber to create a saturated fog at 35 ± 1 °C. The specimens were positioned at an angle of 20° relative to the normal axis. The specimens were subjected to the fog for up to 14 days, or until surface pitting was visually observed. Specimens were inspected visually each day for corrosion damage. The specimens were weighed prior to salt fog exposure. After the test, the specimens were ultrasonically cleaned in ultrapure $H_2O$ for 30 min to remove salt deposits. They were then ultrasonically cleaned in concentrated $HNO_3$ for 10 min to dissolve corrosion product, dried thoroughly with nitrogen gas, and reweighed once again. Ultrasonic cleaning in $HNO_3$ was then repeated in 1-min increments until the mass change of a specimen was negligible ($\leq$0.002 g).[38] The cleaned specimens were then analyzed by optical and scanning electron microscopy to determine the surface texture, pit depth and size, and other corrosion damage.

### *Corrosion evaluation*

The following scale, developed by the U.S. Army Material Command, was used to grade the specimens after the neutral salt-spray exposure: Stage 0—shows no visible corrosion; Stage 1—sample discoloration and staining; Stage 2—loose isolated rust or corrosion product and early stage pitting of the surface along with minor etching; Stage 3—more extensive rust or corrosion product, minor etching, pitting and more extensive surface damage; Stage 4—extensive rust or corrosion product formation, extensive etching, blistering, deadhesion, and pitting that has progressed to the point where the life of the specimen has been affected.

## 4.4 Results

### *Microhardness measurements*

Microhardness measurements were performed to assess the SLM material strength. The Vickers microhardness for a typical as-prepared A360 specimen was 137 ± 1 HV (1 specimen and 5 spots). This value compares favorably with hardness values reported in the literature for this AM alloy that range from 110–150 HV.[6,39] The relatively high hardness value suggests the material is approaching full densification using the SLM fabrication parameters employed. X-ray computed microtomography images (data not shown) revealed a fully dense material with no detectable internal micropores or voids. Published data indicate the microhardness increases linearly with the alloy density and, based on such data (see Fig. 5B of Ref. 6), the density of the A360 specimens used herein appears to be ca. 2.68 g/cm$^3$.[6] This value is similar to the density of 2.62 g/cm$^3$ that was calculated for multiple specimens based on weight and volume measurements. The density of die-cast A360 is reported as 2.63 g/cm$^3$. During the SLM process, the specimen density is primarily controlled by the fluidity of the molten liquid and the depth of the molten pool.[6,39] The higher the temperature of the molten pool, the lower the viscosity and the better the fluidity.[6,39] The depth of the molten pool determines the degree of metallurgic bonding between adjacent powder layers.[6,39]

### *Specimen texture and morphology of uncoated alloy specimens*

Figure 4.2A presents a digital optical micrograph of a typical SLM A360 specimen as-prepared (the full specimen). This specimen is 2.54 cm × 2.54 cm in dimension with a thickness of 0.635 cm. The blue arrow in the micrograph shows the build direction (Z direction). Therefore, the micrograph shows the X-Z plane surface orthogonal to the build surface. This is the long axis in the "stand up" orientation of the build. The as-prepared specimen has a rough surface texture on the planar faces as well as the build edges. No additional surface pretreatment was applied to abrade or smooth the specimen before obtaining the micrographs.

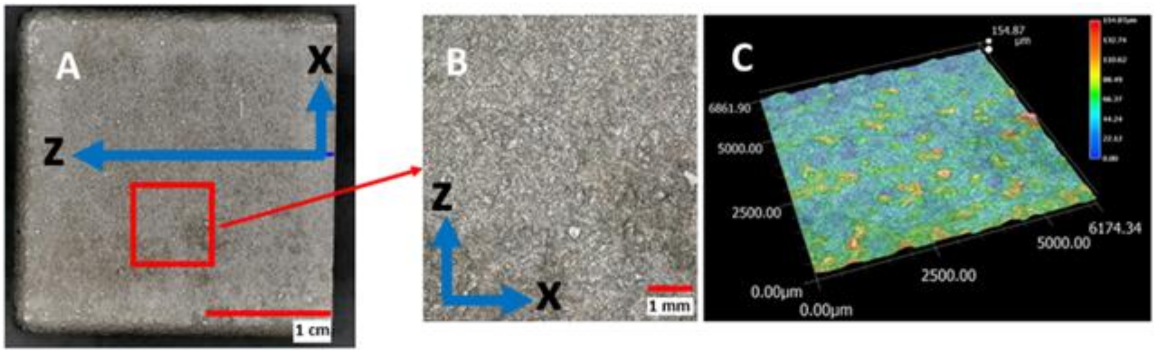

**Figure 4.2.** (A) Optical micrograph of an as-prepared A360 aluminum alloy specimen (X-Z plane). The blue arrow shows the build direction. The specimen is 2.54 cm × 2.54 cm × 0.635 cm thick. (B) Higher magnification optical micrograph (ca. 0.6 cm × 0.6 cm) of the red boxed area in the plan-view micrograph presented in A. (C) A 3D representation of the surface texture over the area in B. The surface plot is ca. 0.6 cm × 0.6 cm with a z-axis height scale from 0 to 155 µm.

Figure 4.2B shows a higher magnification (ca. 0.6 cm × 0.6 cm), plan-view digital optical micrograph of the red boxed area in Figure 4.2A. The rough surface texture is more apparent. Figure 4.2C presents a 3D surface contour plot (stitched image) of the specimen area presented in Figure 4.2B. Clearly, the as prepared specimens possess a wavy surface texture with feature heights of tens of micrometers. Over the 43 $mm^2$ area displayed in the contour plot, the measured surface roughness, $S_q$, is 18 µm with a maximum peak-to-valley height, $S_z$, of 155 µm.

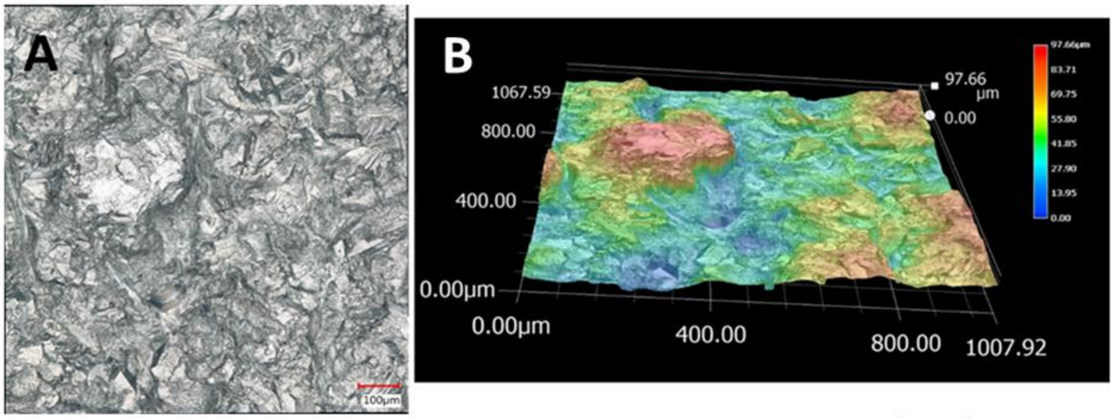

**Figure 4.3.** (A) Plan-view digital optical micrograph (1100 × 1000 μm$^2$) of an as-prepared A360 aluminum alloy specimen (X-Z plane). (B) A 3D contour profile of the surface texture over the area in A. The red scale bar in A is 100 μm. The surface plot is ca. 1100 × 1000 μm$^2$ with a z-axis heigh scale from 0 to 98 μm.

Figure 4.3 presents another visual perspective of the surface texture of the as-prepared A360 aluminum alloy specimen. Figure 4.3A shows a plan-view digital optical micrograph of the surface (0.1 cm × 0.1 cm) and Figure 4.3B shows a 3D surface contour plot of the same area. The specimen consists of a wavy surface texture with elongated ridge-like features randomly oriented. The surface plot reveals raised domains that are a few hundred micrometers in dimension, and these are separated by lower regions and valleys. Based on the analysis of 5 spots (grid pattern and image size of 106 μm$^2$) across the specimen, the surface roughness $S_q$, over this geometric area was found to be 18 ± 2 μm with a maximum peak-to-valley dimension, $S_z$, of 105 ± 12 μm.

Figure 4.4 presents plan-view scanning electron micrographs of an A360 alloy specimen (X-Z plane) after abrading and polishing at two different magnifications. The micrographs reveal a common surface feature found on most of the A360 specimens examined in this work. The lower magnification electron micrograph on the left (A) reveals multiple micrometer-sized "white" particulates decorating areas of the alloy surface. These are generally Si particles, as confirmed by EDS analysis. The higher magnification micrograph on the right (B) shows a larger flake feature that is several micrometers in dimension in the long direction. EDS analysis confirmed this feature to also be Si-rich. In (C), EDS X-ray signal intensities are presented for Al, Si and O that were recorded along the red line in (B).

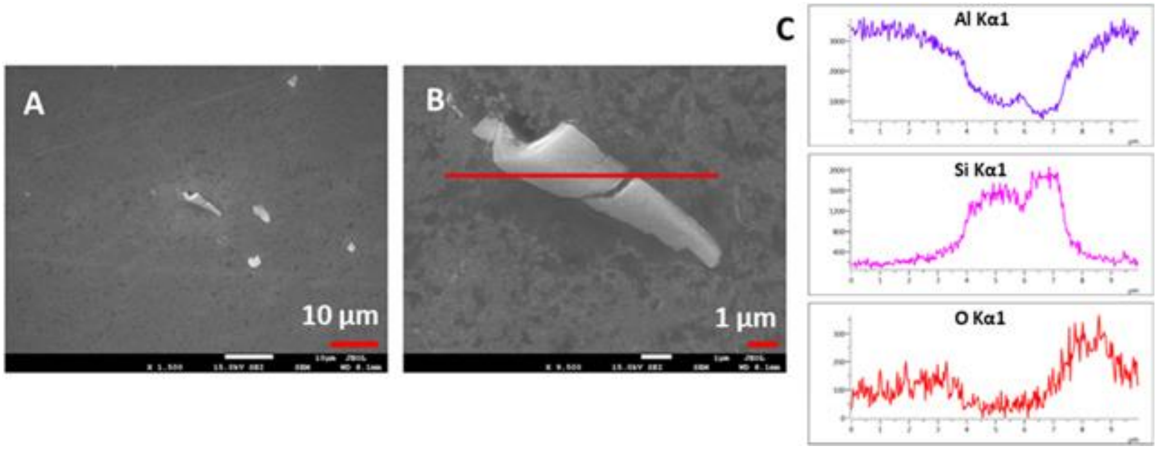

**Figure 4.4.** Scanning electron micrographs of an abraded and polished A360 aluminum alloy specimen (X-Z plane) at (A) a lower (1500×) and (B) a higher (9500×) magnification. Both micrographs are secondary electron images. Both micrographs shown also reveal the common kind of surface artifact found on the specimens, the Si-rich flakes. Prior to acquiring the micrographs, the specimens were degreased and deoxidized after the abrading and polishing steps. (C) Energy dispersive X-ray spectroscopic (EDS) signal intensities for Al, Si and O recorded along the linear distance (red line) shown in B.

Figure 4.5 presents plan-view scanning electron micrographs of an A360 alloy specimen (X-Z plane) after abrading and polishing, as well as degreasing and deoxidation. Such surface smoothing made for easier visualization of the native surface features. Secondary (A, left) and backscattered (B, right) electron micrographs are compared for the same region of the specimen surface. The micrographs reveal some larger Si flakes (white features) in different locations, like those seen in Figure 4.4. Such coarse Si particles are more typical of the die-cast A360 ($AlSi_{10}Mg$) microstructure.[10] Some microvoids (yellow circles) and pits (white arrows) are also evident. Such features have been observed on A360 specimens produced by SLM.[39] The microvoids could arise from loosely bound power particles removed during the abrading and polishing steps.

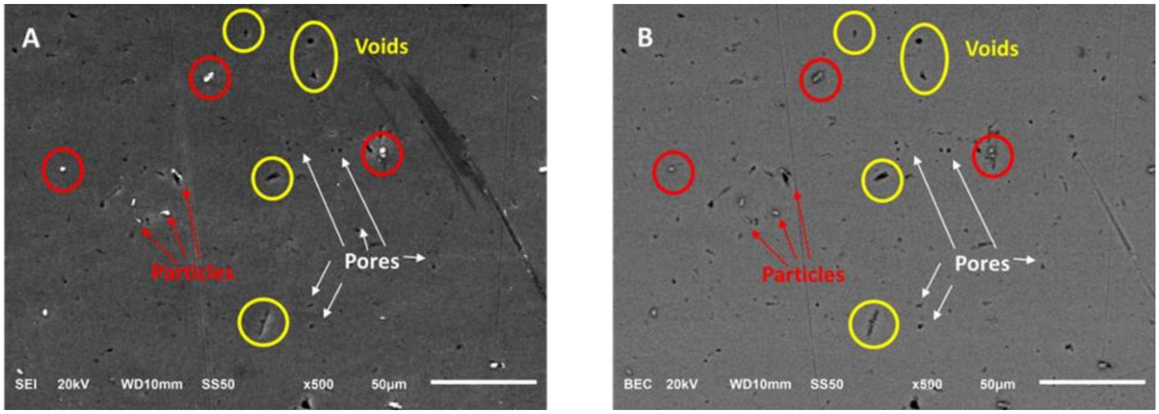

**Figure 4.5.** Plan-view scanning electron micrographs of an A360 aluminum alloy specimen (X-Z plane) after abrading, polishing, degreasing, and deoxidizing. The micrograph on the left (A) is the secondary electron image while the micrograph on the right (B) is the backscattered electron image of the same area in (A). Second-phase particles are identified with red circles and arrows, micro voids are shown in yellow circles, and native pores indicated by white arrows.

The Si particles are phase separated from the aluminum matrix. Their dimensions are a few micrometers or smaller. Several are indicated with the red arrows and circles. The pores or pits seen tend to be circular in shape while the microvoids possess a more irregular, elongated shape. Aboulkhair et al. has referred to these two types of surface defects as metallurgical pores and keyhole pores, respectively.[39] The circular pores likely arise from moisture and ambient gas trapped in the melt pool during the build.[39] The microvoids likely result from incomplete fusion and sintering of the metal powder particles during the laser scan across the build.[39] The dimensions of the pores and microvoids are in the range of hundreds of nanometers to a few micrometers and are confined to the surface region. These microvoids do not significantly lower the density of the material or reduce the hardness. It is likely that some of the pits are introduced during the deoxidation surface pretreatment step, and are not native to the material.[40] The hardness of 137 HV measured for the SLM specimens used in this work suggests that the existing microvoids and pores do not significantly reduce the overall specimen density. For comparison, the Vickers hardness of aged die-cast A360 has been reported to be 130–133 HV.[41]

Figure 4.6 reveals more about the microstructure of a typical SLM A360 specimen (X-Z and X-Y planes) after abrading, polishing and tint etching. As indicated in the Experimental section, the mechanical polishing was performed with 0.3 μm diam. alumina powder slurry as the final step. This was followed by tint etching with Weck's reagent.[34,35] The micrograph of the X-Z surface shows the characteristic layering morphology characteristic of SLM fabrication.[6–14,41] The layer-to-layer and melt tracks visible are stacked to form good metallurgical bonding. In this micrograph, the boundaries of the melt pool are visible with a few identified by dashed lines. The micrograph (X-Y) of the build surface more clearly reveals the elongated cellular network typical of A360 prepared by SLM.[6–14,41] Based on published work, the cells consist of Al grains surrounded by a hexagonal network of Si phase.[6–14,41] The coarse grains seen in the micrograph for the X-Y plane are several hundred micrometers in long dimension.

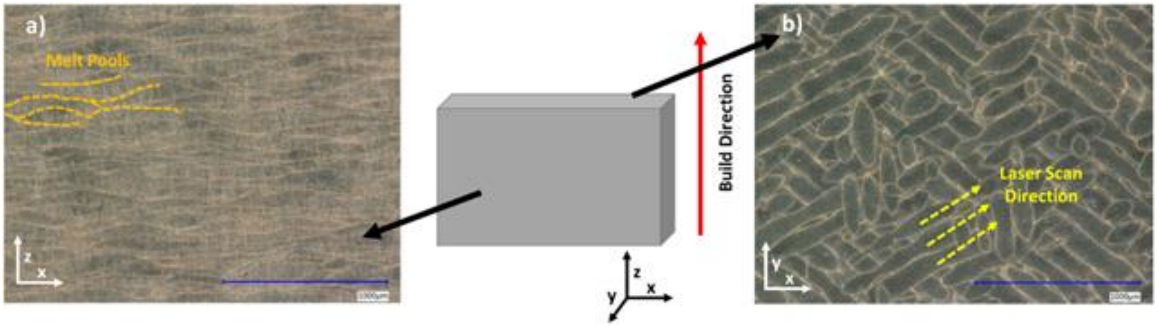

**Figure 4.6.** Scanning electron micrographs of an SLM A360 aluminum alloy specimen after abrading, polishing, degreasing, and deoxidizing. As a final step, specimens were tint etched with Weck's reagent. Shown are micrographs for the (a) X-Z and (b) X-Y (build surface) planes.

Figure 4.7 presents additional scanning electron micrographs that reveal the typical microstructure found in SLM manufactured A360. Shown is the surface of the X-Z plane. A dendritic α-Al phase is encased in a cellular Si network. Layers of fine and coarse cells are oriented horizontally. The fusion of melt pools (MP) creates layers of fine and coarse cells, and an intermediate area known as the HAZ (heat affected zone). The fine and coarse cell structures are controlled by the solidification rate and temperature gradient within the melt pool. The edge of the melt pool experiences a high temperature gradient and low solidification rate, which leads to larger crystals. The opposite is experienced in the center of the melt pool, where a rapid cooling rate and low temperature gradient bearing small crystals packed tightly together. The HAZ occurs at the interface of the previously fused layer. The Si phase amalgamates into larger clusters and breaks apart the fine cellular network. The EDS X-ray intensity maps reveals the cellular network of Al phase segregated by the Si network. The finer elongated Al grains or cells are on the order of 2 µm in the long direction and a little less than 1 µm in width. Secondary phases of Mg or Si-Mg particles, segregated from the Al phase, were not detected on any of the SLM A360 specimens examined. This is a common difference between cast and SLM prepared alloys.[4,12,42,43] The absence of these segregated particles reduces the number of galvanic couples present on the SLM alloy and generally leads to better corrosion resistance of the SLM as compared to the cast alloy.[4,12,31,42,43]

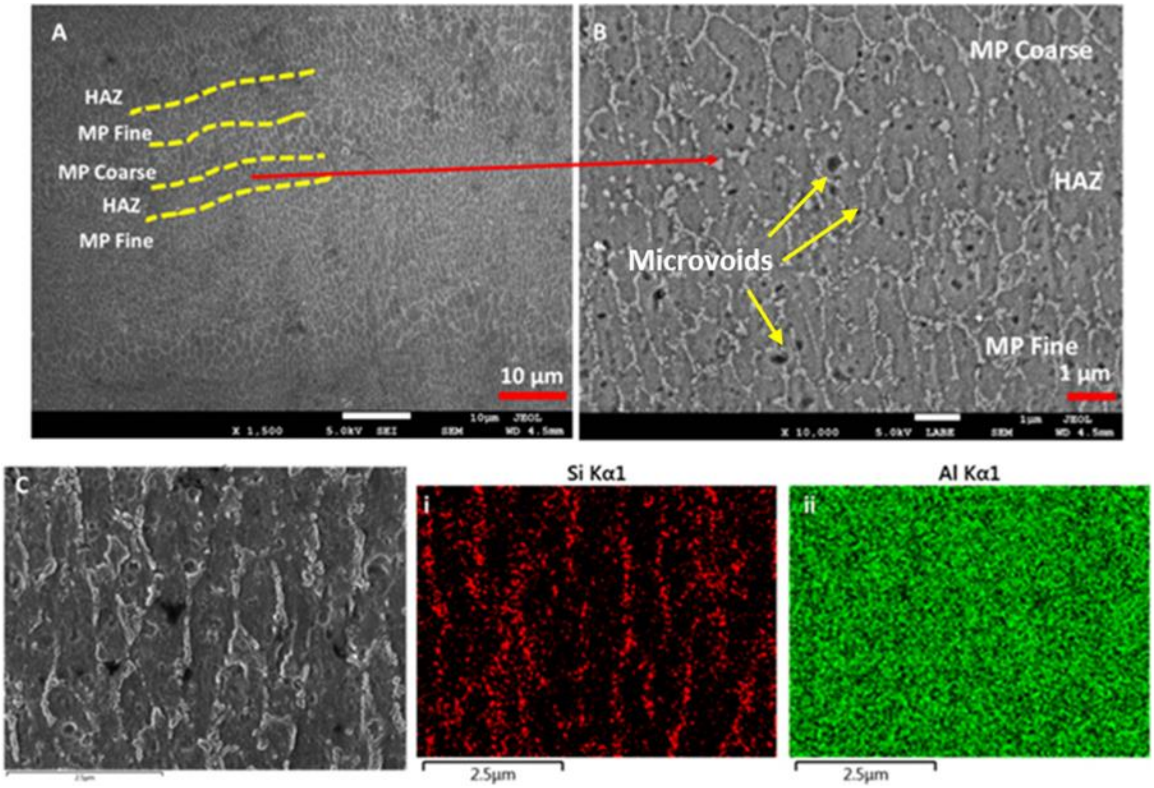

**Figure 4.7.** Plan-view scanning electron micrographs (A-C) of an SLM A360 aluminum alloy specimen after abrading, polishing, degreasing, and deoxidizing. Specimens were also tint etched with Weck's reagent. Shown are micrographs for the X-Z plane. (A) secondary electron image, 1500×, (B) increased mangnification of the melt pool border, backscattered electron image, 10,000×, (C)) secondary electron image, 10,000× along with corresponding EDS X-ray intensity maps for (i) Si and (ii) Al. Abbreviations- MP (melt pool), and HAZ (heat affected zone).

*Specimen texture and morphology of TCP-coated alloy specimens*

Figure 4.8A presents a series of scanning electron micrographs of a TCP-coated A360 alloy. The alloy was abraded, polished, degreased, deoxidized, and immersion coated with TCP at room temperature for 10 min In the center of the micrograph in Figure 4.8A, a red boxed area reveals a typical alloy surface feature, as described above, and that is a Si flake exposed adjacent to a microvoid. The TCP coating has a nodular surface texture. There are also characteristic elongated "white" particulates decorating the surface. An example of one of these is shown in the red boxed area in the upper left. These are so-called nodular particles of the TCP coating that typically decorate the immersion-coated aluminum alloy surface. Their presence, without any coating bath filtration prior to formation, provides qualitative evidence for the formation of the conversion coating.[19,20,23,25,27,29,40] Based on prior work with wrought aluminum alloys, the conversion coating formed by immersion under these conditions is thin and on the order of 100–300 nm. [16,18–20,25,27,29,40,44] We did not make any measurements of the TCP coating thickness on the A360 specimens.

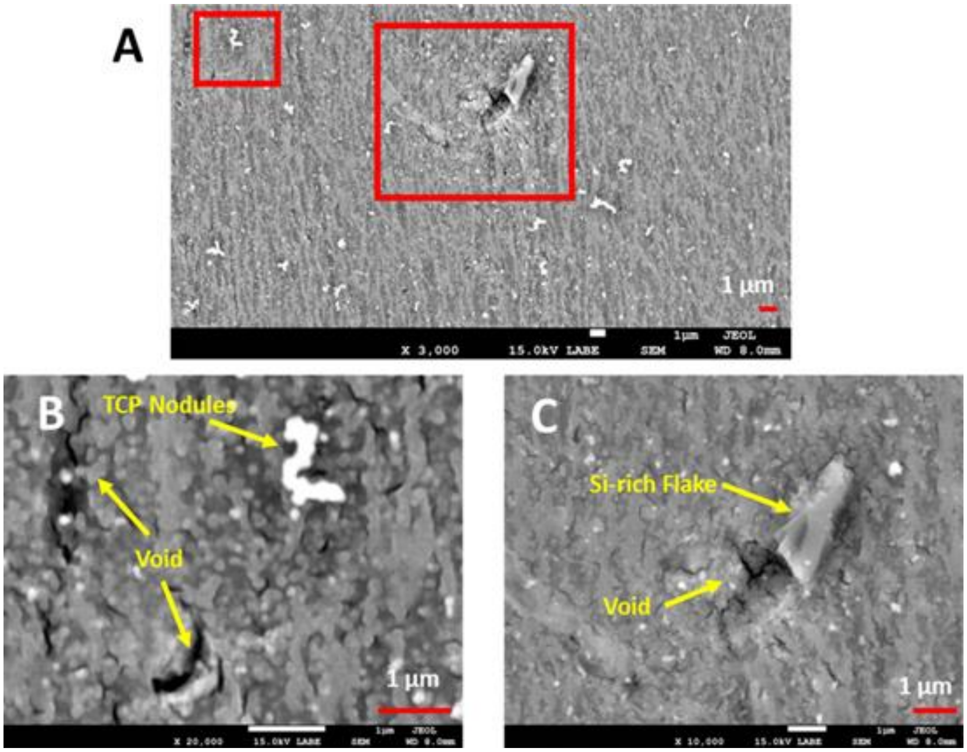

**Figure 4.8.** (A) Backscattered electron micrograph (3000×) of an abraded and polished A360 aluminum alloy specimen (X-Z plane) after formation of a TCP conversion coating by a 10-min immersion. The smoothed specimen was degreased and deoxidized prior to coating formation. The presence of the TCP coating is evidenced in A by the white coating nodules and particles that decorate the entire surface. (B) Backscattered electron micrograph (20,000×) of the upper left boxed area in A. (C) Backscattered electron micrograph (10,000×) of the center boxed area in A.

Enlarged backscattered electron micrographs of the boxed regions in Figure 4.8A are presented in Figure 4.8B and C. In Figure 4.8B (the left boxed area in Figure 4.8A), the nodular morphology of the TCP coating is evident, along with one of the aggregate TCP particles. There is also a microvoid and small crack present in this region of the alloy, as indicated by the yellow arrows. It is unclear how conformally the TCP coating forms across such surface defects. Our supposition is that there is incomplete conversion coating formation on and around such defects, and are the locations of initial corrosion attack.[40,44] Figure 4.8C (the center boxed area in Figure 4.8A) shows a typical Si-rich flake surface feature. These become visible only after abrading and polishing followed by ultrasonic cleaning. There is evidence for the nodular TCP coating around the flake and across the surface based on the presence of the coating precipitate particles.

Figure 4.9 presents an SEM micrograph of a TCP-coated A360 specimen (X-Z plane), and corresponding EDS elemental profiles recorded along the line scan shown in the micrograph. The specimen was abraded and polished, degreased, deoxidized, and immersion coated with TCP for 10 min. The micrograph reveals a common Si-rich surface feature found on the A360 alloy. The particle is about 2 μm in long dimension. Evidence that the particle is composed of Si is the increase in the EDS Si X-ray intensity seen across the feature. The corresponding X-ray intensity for Al decreases in the region of the Si particle as the underlying Al phase is buried. Surrounding the Si particle, the TCP coating forms as evidenced by the elevated Zr, F, and O X-ray intensities. All three elements are components of the conversion coating. Cr was often detected and the intensity correlated with the Zr signal intensity. When formed by immersion, the coating consists of an outer layer of hydrated zirconia, $ZrO_2 \cdot nH_2O$, and interfacial layer of hexafluoroaluminate, $K_xAlF_{x+3}$, as has been reported on previously.[18–20,23–25,27–30,45] It looks as though for this surface feature, the TCP coating is not present. However, elevated levels of Zr and F are observed around the Si feature providing clear evidence for the coating formation across the alloy surface.

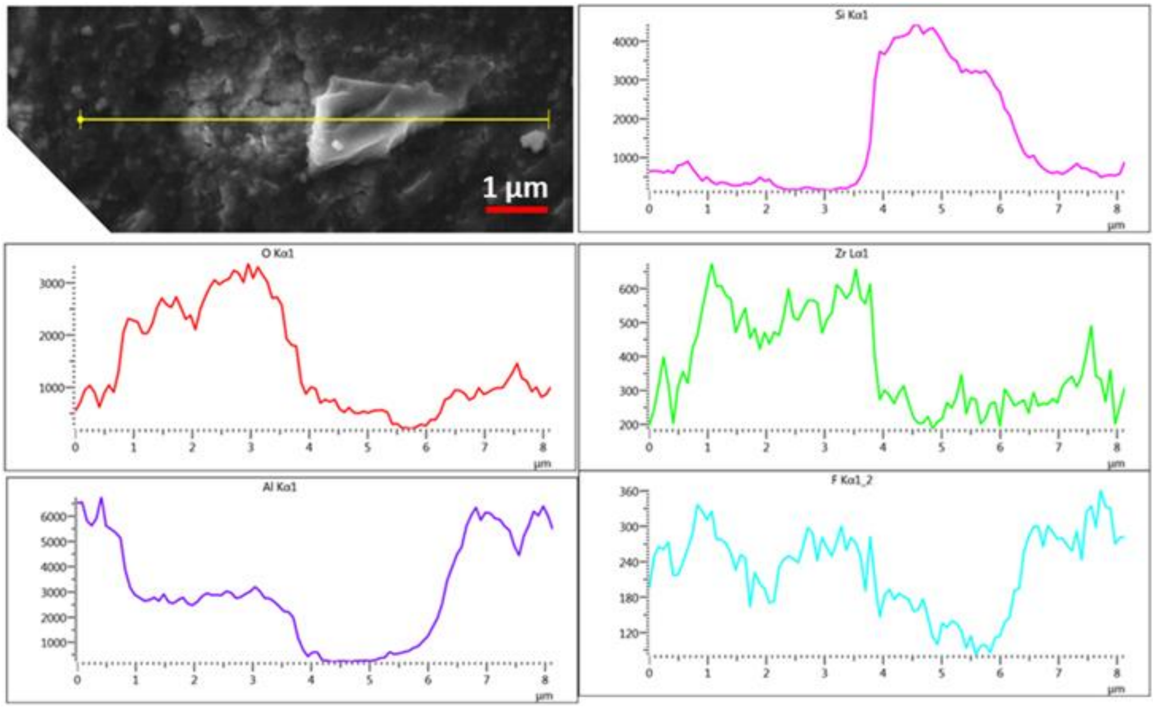

**Figure 4.9.** Scanning electron micrograph of a TCP-coated A360 aluminum alloy specimen (X-Z plane). The coating was formed on specimens after abrading and polishing, degreasing, and deoxidizing. The TCP coating was formed by a 10-min immersion. The electron micrograph shows a Si-rich surface feature. X-ray data for different elements were recorded by EDS along the yellow line. Kα and Lα X-ray emission intensity profiles for Si, O, Zr, Al and F are presented.

Figure 4.11 presents an SEM micrograph of a different region of the same TCP-coated A360 specimen as in Figure 4.9 and corresponding EDS elemental profiles recorded along the line scan shown in the micrograph. The micrograph reveals a TCP coating aggregate formed on the surface. The EDS X-ray intensities along the line profile reveal increases in Zr, F and O signals for the aggregate. X-ray signal intensity was also detected for Cr (data not shown). There is also intensity for these elements on the alloy surface surrounding the aggregate confirming that

TCP coating forms across the alloy surface. Evidence for the presence of Cr in the TCP coating is provided in the SEM and EDS data presented in Figure 4.10 and Table 4.1.

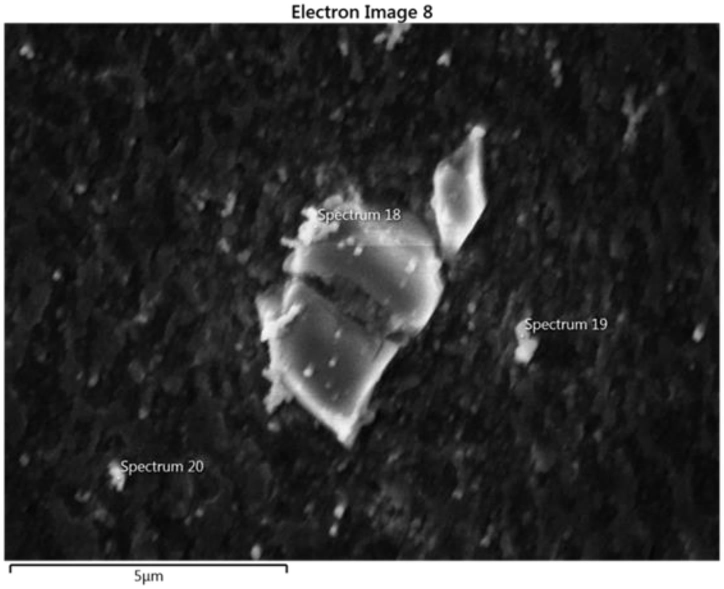

**Figure 4.10.** SEM micrograph of a TCP-coated A360 specimen. The TCP coating was formed by immersion for 15 min. The micrograph was collected using a 7 kV accelerating voltage and an 8 mm working distance. EDS X-ray spectra were recorded at three different locations on the image: Spectrum 18, 19 and 20.

**Table 4.1.** Elemental weight percent of EDS point spectra of 15-minute TCP coated A360 specimen using a 7 kV accelerating voltage and 8 mm working distance.

| | Spectrum 18 | Spectrum 19 | Spectrum 20 |
|---|---|---|---|
| Element | wt.% | wt.% | wt.% |
| C | 9.4 | 4.6 | 4.4 |
| O | 29.2 | 21.6 | 25.7 |
| F | 5.5 | 4.7 | 4.8 |
| Al | 9.2 | 35.9 | 30.7 |
| Si | 5.3 | 4.2 | 3.4 |
| Cr | 14.5 | 9.9 | 9.1 |
| Zr | 26.9 | 19.1 | 21.9 |
| Total | 100 | 100 | 100 |

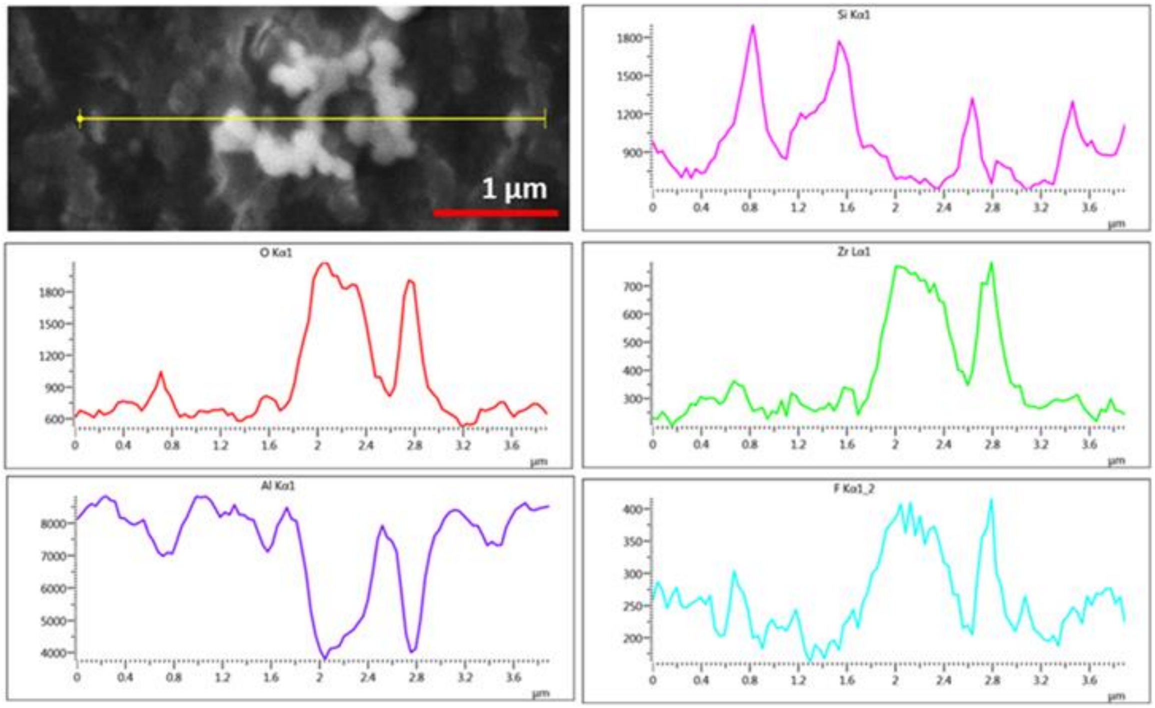

**Figure 4.11.** Scanning electron micrograph of a TCP-coated A360 aluminum alloy specimen (X-Z plane) showing a nodular TCP coating deposit. The coating was formed on specimens after

**Figure 4.11 (cont'd)**

abrading and polishing, degreasing, and deoxidizing. The TCP coating was formed by a 10-min immersion. X-ray data for different elements were recorded by EDS along the yellow line. Kα and Lα X-ray emission intensity profiles for Si, O, Zr, Al and F are presented.

Multiple regions of different TCP-coated specimens were analyzed in this manner to confirm that there is widespread coating formation across the as-prepared alloy. There is also some evidence in the Si X-ray intensity profile for smaller Si phases on the alloy surface. The corresponding X-ray intensity for Al decreases in the region where the Si particle is located. Surrounding the Si particle, the TCP coating forms as evidenced by the elevated Zr, F and O X-ray intensities. Interestingly, the X-ray intensity for Si has four spiked regions across the line profile, all spaced about 0.8 μm apart. The X-ray intensity for Al also reveals a spiked profile with a similar spacing. The spikes in Al X-ray intensity, however, correlate with regions of minimum Si intensity. This pattern reflects the honeycomb network of Si phase that surrounds the Al grains, as is revealed in Figure 4.7.[6–14,39,41,46]

*Electrochemical properties of uncoated and TCP-coated alloy specimens*

As mentioned above, a primary goal of this work was to learn about the electrochemical behavior of as-prepared A360 alloys with and without a TCP conversion coating**.** Figure 4.12 presents potentiodynamic polarization curves for representative as-prepared A360 specimens. The specimens were pretreated by solution processing (degreasing and deoxidation) only before the electrochemical measurements. No abrading or polishing was applied to smooth the rough surface texture. The curves were recorded at room temperature in naturally aerated 0.5 M $Na_2SO_4$ + 0.01 M NaCl. Anodic curves are presented for three different specimens and cathodic curves are presented for two different specimens. It can be seen that the OCP for all five specimens ranges between −0.5 and −0.6 V vs Ag/AgCl. The cathodic polarization curves for these two, and multiple other specimens not presented, were reproducible in terms of the current magnitude over the potential range probed. The current at potentials negative of ca. −0.8 V is attributed to the diffusion-limited reduction of dissolved oxygen. This was verified by the decreased current observed at these potentials when the solution was deaerated by nitrogen gas purging. The current at −0.8 V, for example, is near $10^{-5}$ A/cm$^2$, or 10 μA/cm$^2$, for both specimens The redox reaction at this pH (5–6) is presumed to be the $4e^-/4H^+$ reduction of $O_2$ to $OH^-$ according to,

$$O_2 + 2H_2O + 4^{e-} \rightarrow 4OH^- \qquad (10)$$

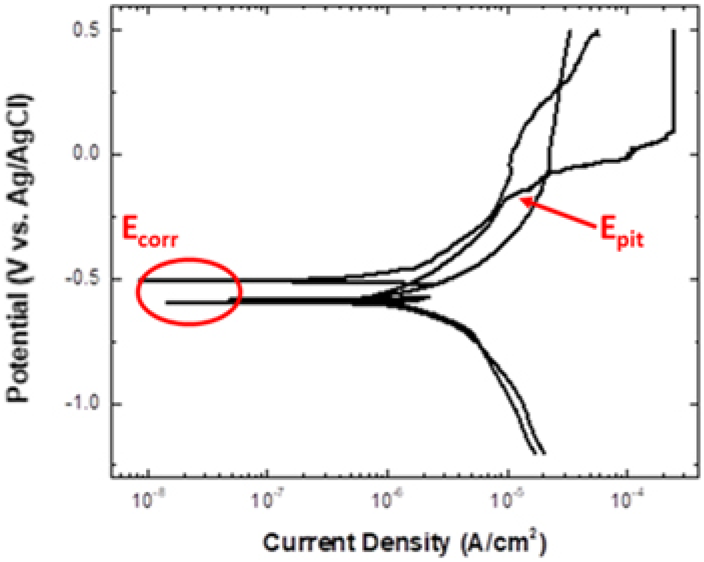

**Figure 4.12.** Potentiodynamic polarization curves recorded in naturally aerated 0.5 M $Na_2SO_4$ + 0.01 M NaCl for as-prepared A360 specimens (X-Z plane) after degreasing and deoxidation. Scan rate = 1 mV/s. The measurements were made at room temperature. Three separate specimens were used for the anodic and two specimens were used for the cathodic polarization curves.

In contrast, there was more variability observed in the anodic polarization curves for the three specimens. One of the specimens exhibited a near steady-state passivation current for aluminum hydroxide/oxide formation out to 0.5 V vs Ag/AgCl with no evidence of oxide film breakdown or onset of pitting corrosion. Another specimen showed the passivating oxide formation current only out to 0.2 V at which oxide film breakdown and localized pitting corrosion initiated. This behavior was the exception rather than the rule for the as-prepared specimens. Another specimen showed stable oxide formation current only out to −0.2 V before oxide film breakdown and onset of localized pitting corrosion. The potential for breakdown is demarked as $E_{pit}$ in the figure. The oxide formation currents for all three specimens were variable but in the range of $10^{-5}$ A/cm$^2$. For example, the anodic current for these three specimens at −0.1 V approached 20 µA/cm$^2$. The oxide film formation involves the following redox reaction,

$$Al + 2H_2O \rightarrow AlOOH + 3H^+ + 3e^- \qquad (11)$$

The variability in the passivation current magnitude, stability with potential, and onset potential for breakdown and localized pitting corrosion indicates the oxide film formation is complex on the as-prepared alloy surface and the oxide film integrity (i.e., completeness of formation, defects and imperfections) depends on the alloy specimen-specific surface condition. The real surface area or surface texture differences in the as-prepared specimens affects the magnitude of the oxide formation current and the oxide layer integrity as does the fraction of Si phase present and the integrity of the interface with the Al grains. The electrochemical data reveal that there can be considerable variability in the anodic polarization curves for the as-prepared alloys.

Figure 4.13 presents a characteristic OCP versus time curve recorded for an as-prepared alloy specimen during a 20-min TCP immersion coating. The as-prepared alloy was degreased and deoxidized.[21] These curves provide qualitative insight on the condition of the alloy surface and the dynamics of coating formation during the immersion process. The curve shape for this as-prepared A360 specimen very much resembles the curve shapes reported and discussed for other wrought aluminum alloys.[16–30,40,44,45] Immersion times of 10 and 15 min were also investigated. The OCP versus time curves for the other two immersion periods resembled the one shown here. The OCP of the alloy shifts negatively by some 700 mV during the first 3–4 min of immersion. This shift reflects the dissolution of the native passivating oxide that exists on the Al phase of the alloy. The TCP bath is acidic at ~pH 3.8 and contains 23.6 ± 0.1 ppm of fluoride.[28] The negative potential shift is caused by the increased rate of dissolved oxygen reduction and or hydrogen evolution needed to counterbalance the increased rate of aluminum oxidation after dissolution of the passivating oxide layer. Clearly, the alloy is corroding during the TCP coating formation and this leads to the formation of an aluminofluoride interfacial layer, as has been discussed previously for the TCP formation on wrought aluminum alloys.[16–30,40,44,45] After 5 min, the potential trends toward a stable value in the −1.1 to −1.2 V range as the oxide layer gets fully dissolved. At this potential, the following primary cathodic reaction is occurring is likely:

$$2H_2O + 2e^- \rightarrow 2OH^- + H_2(g) \tag{12}$$

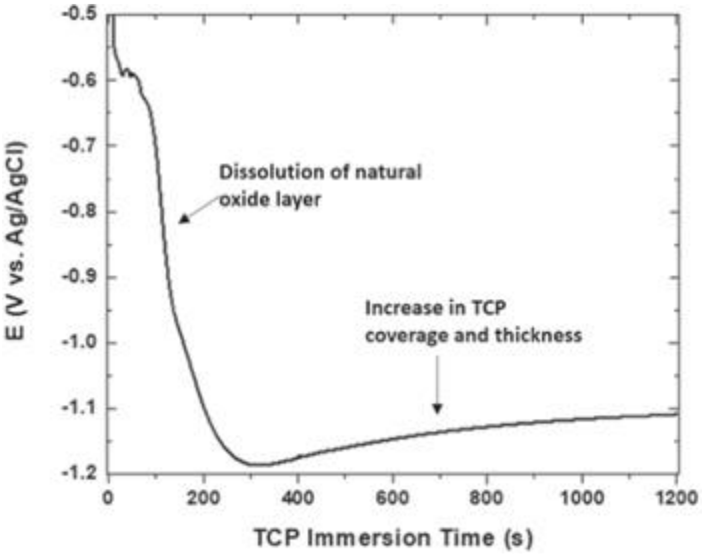

**Figure 4.13.** In-situ formation of the TCP conversion coating as followed through an OCP versus time measurement for a degreased and deoxidized A360 aluminum alloy specimen (X-Z plane) during immersion in the TCP (Bonderite T5900 RTU) coating bath. The immersion time was 20 min.

This reaction, as well as the reduction of dissolved oxygen which is also occurring, causes a pH increase in the interfacial region, which leads to hydrolysis of the coating bath precursors and formation of the low solubility precipitates that constitue the outer layer of the conversion coating [19–22,29,30]:

$$ZrF_6^{2-} + 4OH^- \rightarrow ZrO_2 \cdot 2H_2O + 6F^- \tag{13}$$

$$Cr^{3+} + 3OH^- \rightarrow Cr(OH)_3 \tag{14}$$

The dissolution of the native oxide and oxidation of the underlying aluminum in the acidic fluoride medium occurs according to the following two reactions:

$$\mathrm{Al}(OH)_3 + 3H^+ + 6F^- \rightarrow AlF_6^{3-} + 3H_2O \tag{15}$$

$$\mathrm{Al} + 6\,F^- \rightarrow AlF_6^{3-} \tag{16}$$

The $AlF_6^{3-}$ produced forms the $K_xAlF_{3+x}$ interfacial layer on which the TCP coating deposits.[18–20,24,25,27,29,45] Our group, and others, have previously reported on the formation mechanism and electrochemical properties of TCP formed on wrought AA2024-T3, AA6061-T6 and AA7075-T6 aluminum alloys.[16–30,40,44,45] The formation mechanism on this SLM aluminum A360 alloy appears similar. The TCP coating thickness on the A360 alloys was not measured, but past work with other wrought aluminum alloys revealed immersion times of 10–20 min produce conversion coating thicknesses of 100–300 nm, depending on the TCP coating bath composition. [16,20,25,27,29,44,45]

Figure 4.14 presents typical potentiodynamic polarization curves for as-prepared A360 aluminum alloy specimens in naturally aerated 0.5 M $Na_2SO_4$ + 0.01 M NaCl before and after TCP coating. The specimens were degreased and deoxidized with no abrading or polishing to smooth the surface texture. Separate coated and uncoated specimens were used for the anodic and cathodic curves, respectively. The OCP was allowed to stabilize for 1 h before the start of the measurements. The uncoated specimens exhibit the largest anodic and cathodic currents at all potentials. Both the anodic and cathodic currents are suppressed by the presence of the TCP coating (formed by a 15-min immersion) in much the same way both currents are suppressed on TCP-coated AA2024-T3,[18–21,28,40,44,45] 6061-T6[23,45] and 7075-T6[23,25,27,29,45] alloys. The suppressed currents for both aluminum oxidation and dissolved oxygen reduction are consistent with the conversion coating providing both anodic and cathodic protection to this SLM AM alloy. Figure 4.15 presents a comparison of potentiodynamic polarization curves for as-prepared alloy specimens before and after TCP coating for immersion times of 10, 15, and 20 min.

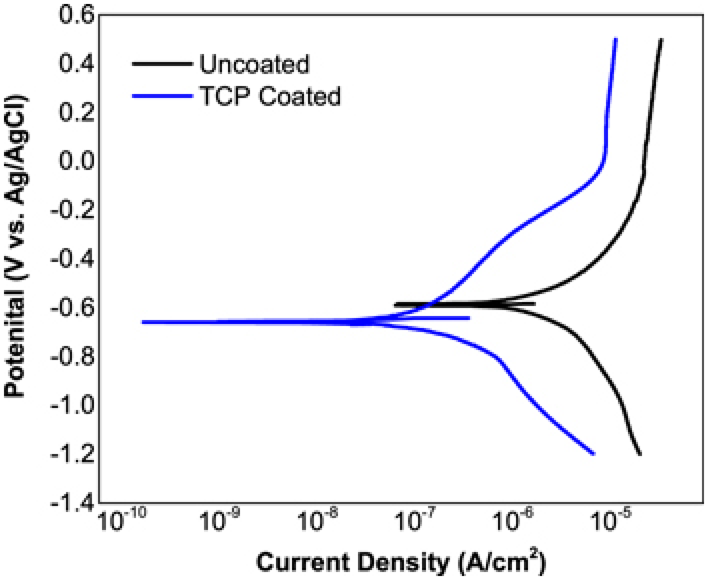

**Figure 4.14.** Potentiodynamic polarization curves for degreased and deoxidized A360 aluminum alloy specimens (X-Z plane) uncoated and after TCP coating by immersion for 15 min at room temperature. The measurements were made in naturally aerated 0.5 M $Na_2SO_4$ + 0.01M NaCl. Scan rate = 1 mV/s. Separate specimens were used for the anodic and cathodic curves.

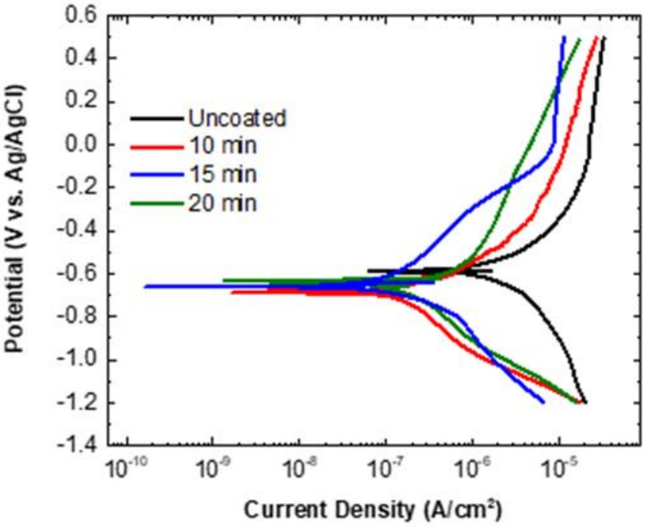

**Figure 4.15.** Potentiodynamic polarization curves for degreased and deoxidized A360 aluminum alloy specimens (X-Z plane) uncoated and after TCP coating by immersion for 10, 15,

**Figure 4.15 (cont'd)**

and 20 min at room temperature in naturally aerated 0.5 M $Na_2SO_4$ + 0.01 M NaCl. Scan rate = 1 mV/s. Separate specimens were used for the anodic and cathodic curves.

Table 4.2 summarizes some numerical electrochemical data for the uncoated and TCP-coated A360 specimens. Data are presented for TCP coating times of 10, 15 and 20 min, and were obtained from OCP and LPR measurements, potentiodynamic polarization curves, and EIS data recorded at the OCP. It can be seen that the nominal OCP for the uncoated specimen is −580 ± 17 mV while the nominal values for the TCP-coated specimens are slightly more negative ranging from −617 to −661 mV. The OCP values for all the TCP-coated specimens are more negative than the values for the uncoated specimens. This indicates the TCP coating has a slightly greater effect decreasing the cathodic than the anodic reaction kinetics.

**Table 4.2.** Numerical electrochemical data for the uncoated and TCP-coated A360 aluminum alloy specimens formed by immersion for different times (10–20 min). Data are reported as mean ± standard error of the mean for n = 3 measurements with separate specimens. *Statistically significant difference between the uncoated and each TCP-coated sample data at the 95% confidence interval. Statistical significance was assessed using an unpaired, two-tailed Student's t-test with the uncoated data serving as the control.

| | Uncoated | 10 min | 15 min | 20 min |
|---|---|---|---|---|
| OCP (mV) | −580 ± 17 | −640 ± 17* | −661 ± 12* | −617 ± 12 |
| LPR (kΩ·cm$^2$) | 8.11 ± 0.95 | 242 ± 55* | 212 ± 40* | 306 ± 124* |
| $i_{corr}$ (μA/cm$^2$) | 5.63 ± 0.57 | 0.203 ± 0.054* | 0.219 ± 0.052* | 0.337 ± 0.117* |
| j @ − 0.1 V (μA/cm$^2$) | 16.8 ± 3.29 | 7.37 ± 3.25 | 4.61 ± 1.37* | 1.49 ± 0.98* |
| j @ −0.8 V (μA/cm$^2$) | −5.58 ± 1.06 | −0.38 ± 0.04* | −0.48 ± 0.15* | −1.77 ± 1.06* |
| $Z_{0.01\ Hz}$ (kΩ·cm$^2$) | 15 ± 1 | 162 ± 15* | 174 ± 62* | 155 ± 42* |

Data are also presented for the linear polarization resistance (LPR). The nominal value for the uncoated specimens is 8.11 ± 0.95 kΩ·cm$^2$ while the nominal values for the TCP-coated specimens are all significantly larger by a factor of 25–40× ranging from 212 − 306 kΩ·cm$^2$. This is the resistance to current flow (anodic and cathodic reactions) when the specimen is polarized away from the OCP. Anodic and cathodic current densities measured from the potentiodynamic polarization curves at −0.1 and −0.8 V, respectively, reveal that the TCP conversion coating suppresses both, consistent with the coating providing both anodic and cathodic corrosion protection. The nominal anodic current for the uncoated specimens at −0.1 V is 16.8 ± 3.3 μA/cm$^2$ and is lower by a factor of 2–11× for the TCP-coated specimens ranging from 1.5 − 7.4 μA/cm$^2$. The nominal cathodic current for the uncoated specimens at −0.8 V is −5.6 ± 1.1 μA/cm$^2$ and is lower by a factor of 3–14× for the TCP-coated specimens ranging from −0.38 to −1.7 μA/cm$^2$. Finally, the impedance modulus at 0.01 Hz, $Z_{0.01\text{ Hz}}$, is 10–12× larger for the TCP-coated specimens than for the uncoated controls. The trend in $Z_{0.01\text{Hz}}$ values, which are reflective of the polarization resistance ($R_p$), are in agreement with the trend in the LPR values, although the increase is less (10–12× vs 25–40×). Taken together, the electrochemical data indicate that conversion coatings formed for all three times provide an equivalent level of corrosion suppression to the alloy. The 15-min immersion time was used to form the TCP coating on specimens subjected to the salt spray accelerated degradation test discussed below.

Figure 4.16 presents Bode plots of the total impedance (absolute value) and phase shift as a function of frequency for the uncoated and TCP-coated A360 specimens (X-Z plane). These curves were analyzed to determine the $Z_{0.01\text{Hz}}$ values in Table 4.2. Figure 4.17 presents Nyquist plots of the data along with the curve fitting. The specimens were degreased and deoxidized prior to conversion coating formation but not abraded or polished to smooth the rough surface texture. The measurements were made at the OCP with an AC sine wave amplitude of ±10 mV in naturally aerated 0.5 M $Na_2SO_4$ + 0.01 M NaCl. The OCP was allowed to stabilize for 1 h before the start of the EIS measurements. In the high frequency range, the impedance values for the uncoated and TCP-coated specimens all converge on the same value of about 15 Ω·cm$^2$. The phase angle is near zero degrees in this range. This value primarily reflects the ohmic resistance of the electrolyte solution ($R_e$).

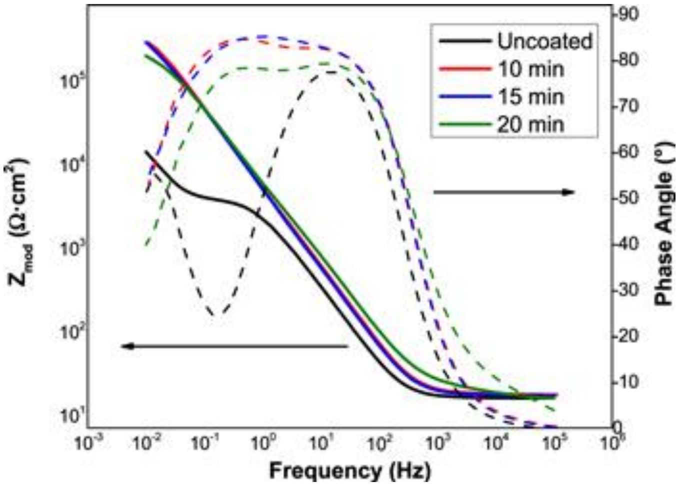

**Figure 4.16.** Bode plots of the impedance modulus (solid lines) and phase angle (dashed lines) versus the frequency for degreased and deoxidized A360 aluminum alloy specimens (X-Z plane) uncoated and TCP-coated by immersion for 10, 15 and 20 min at room temperature. The measurements were made at the OCP in naturally aerated 0.5 M $Na_2SO_4$ + 0.01 M NaCl. AC amplitude = 10 mV.

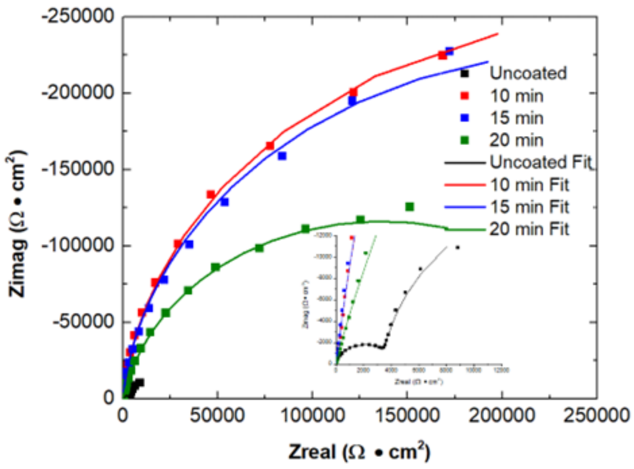

**Figure 4.17.** Nyquist plots of the impedance modulus versus the frequency for degreased and deoxidized A360 aluminum alloy specimens (X-Z plane) uncoated and TCP-coated by immersion

**Figure 4.17 (cont'd)**

for 10, 15 and 20 min at room temperature. The measurements were made at the OCP in naturally aerated 0.5 M $Na_2SO_4$ + 0.01 M NaCl. AC amplitude = 10 mV.

Transitioning into the mid-frequency region, the total impedance increases linearly with decreasing frequency. This arises from the capacitance associated with the hydrated oxide layer or the oxide layer and the biphasic TCP coating on the alloy surface. The slopes of the curves are similar in the region from $10^0$ to $10^2$ Hz. The phase angle is near −90 degrees in this frequency region reflective of the capacitive nature of the oxide and the oxide + TCP coating on the uncoated and TCP-coated specimens, respectively. Finally, in the low frequency region, the plots show significantly higher impedance values for the TCP-coated specimens than for the uncoated control. This is attributable mainly to the polarization resistance across the alloy-solution interface for the anodic and cathodic reactions occurring at the OCP. The low frequency impedance is 10–12× larger for the TCP-coated alloy specimens ($10^5$ $\Omega\cdot cm^2$) as compared to the uncoated alloy ($10^4$ $\Omega\cdot cm^2$). This is consistent with the reduced anodic and cathodic currents in the potentiodynamic polarization curves and the increased $R_p$ values determined from the LPR measurements. Interestingly, the low frequency impedance for the uncoated alloy plateaus and then shows an increase in impedance with decreasing frequency. The physical origin of this behavior is unclear. It should be noted that this behavior was not observed on all uncoated specimens.

In the low-frequency range, the phase angle profile for the uncoated alloy exhibits characteristics of two RC time constants as reflected by the two capacitive peaks at $\sim 10^1$ and $10^{-2}$ Hz. This is also seen in the Nyquist plots in Figure 4.17. In contrast, the phase angle for the

TCP-coated specimens remains near −90 degrees at lower frequencies consistent with single capacitive peak extending to lower frequencies. The larger $Z_{0.01\ \mathrm{Hz}}$ values and more negative phase angles extended to lower frequencies for the TCP-coated specimens are consistent with increased corrosion suppression provided by TCP coating as compared to the uncoated, as-prepared specimens. The TCP coating serves as a barrier layer between the solution and underlying alloy surface, which reduces the rate of aluminum oxidation as well as the rate of oxygen reduction at potentials around the OCP.

The electrochemical impedance data recorded at the OCP were fit to the equivalent circuit presented in Figure 4.1. The summarized data in Table 4.3 are the numerical values for $R_e$, $CPE_{co}$ -Q, $n_{co}$, $R_{po}$, $CPE_{dl}$ -Q, $n_{dl}$ and $R_p$ returned from the fitting. The $R_e$ values are essentially the same for all the specimen types, as expected, at 16–19 $\Omega\cdot cm^2$. The native oxide or the TCP/oxide coating acts as a nonideal capacitor, which is modeled by a constant phase element, $CPE_{co}$. Actual capacitance values were not calculated, but the smaller $CPE_{co}$ -Q values for the TCP-coated specimens are consistent with a lower capacitance and a thicker and less permeable barrier layer than is provided by the native oxide layer on the as-prepared specimens. Pores and other defects in the coating provide channels for electrolyte solution to reach the underlying metal alloy substrate. The resistance of electrolyte ion movement within the defects, pores and channels of the coating is given by $R_{po}$. The data reveal the nominal value for the TCP/oxide coating is 2–3× greater than the value for the native oxide, consistent with improved barrier layer properties provided by TCP. Finally, the polarization resistance, $R_p$, which is the kinetic resistance to the anodic and cathodic reactions happening at the OCP, is 3–5× greater for the TCP-coated than for the uncoated as-prepared specimens. Taken together, the EIS electrochemical data indicate that conversion coatings formed for all three times provide an equivalent level of corrosion protection to the alloy. The values for $n_{co}$ were greater than 0.90 for all the uncoated and TCP-coated specimens and $n_{dl}$ values were greater than 0.83 for all the specimens.

**Table 4.3.** EIS data recorded at the OCP for uncoated and TCP-coated A360 specimens with parameters determined from equivalent circuit analysis. The TCP conversion coating was formed by immersion for 10, 15 and 20 min. N ≥ 3 statistical values reported as mean ± standard error of the mean. *Statistical significance was assessed using an unpaired, one-tailed Student's t-test ($P < 0.05$) with the uncoated data serving as the control.

| | $R_e$ (kΩ·cm$^2$) | $CPE_{co}$ -Q ($\times10^{-6}$) $s^n/(\Omega\cdot cm^2)$ | $n_{co}$ | $R_{po}$ (kΩ·cm$^2$) | $CPE_{dl}$ -Q ($\times10^{-6}$) $s^n/(\Omega\cdot cm^2)$ | $n_{dl}$ | $R_p$ (kΩ·cm$^2$) |
|---|---|---|---|---|---|---|---|
| Uncoated | 16.5 ± 0.6 | 54.24 ± 7.24 | 0.94 ± 0.01 | 4.0 ± 0.4 | (1.11 ± 0.05) ×10$^3$ | 0.98 ± 0.01 | 64 ± 21 |
| 10 min | 17.6 ± 0.2 | 32.41 ± 3.71 | 0.95 ± 0.00 | 7.8 ± 1.5 | 3.64 ± 1.06* | 0.89 ± 0.06 | 319 ± 112* |
| 15 min | 17.8 ± 0.4 | 38.41 ± 7.35 | 0.93 ± 0.01 | 12.2 ± 3.0 | 43.87 ± 38.44* | 0.83 ± 0.08 | 287 ± 99* |
| 20 min | 19.5 ± 0.8 | 30.49 ± 6.64 | 0.92 ± 0.01 | 9.9 ± 0.8 | 6.73 ± 2.11* | 0.87 ± 0.04 | 193 ± 61* |

### *Specimen degradation during anodic polarization*

Experiments were performed to investigate the initial oxidative degradation of a smoothed and tint etched A360 specimen. While the electrochemical measurements were performed on rough as-prepared specimens, some microscopy was performed on smoothed specimens because it makes visualization of early-stage corrosion damage easier. It should be noted that the smooth SLM A360 specimens are generally more corrosion resistant than the as-prepared specimens because (i) the increased surface roughness of the latter leads to more surface area susceptible to corrosion and (ii) the integrity of the passivating surface oxide layer is superior on the smoother surface.[4,31,42] The alloy specimen was subjected to a single potentiodynamic polarization scan starting at 20 mV negative of the OCP out to 1.0 V vs Ag/AgCl at 1 mV/s. The specimen was then ultrasonically cleaned in ultrapure $H_2O$ for 20 min to remove salt deposits and corrosion product. This positive potential limit is well into the region where passivation layer breakdown occurs, and localized pitting commences (see Figure 4.12). In general, the impact of the SLM A360 microstructure on the corrosion behavior is not yet well established. Figure 4.18A presents a lower-magnification scanning electron micrograph of the surface where two overlapping melt pools exist. The top and bottom regions of the surface in the micrograph exhibit a finer Al cellular network. The middle region has a coarser Al cells and larger conglomerates of the Si phase. The localized corrosion damage (Figure 4.18A) reflects what appears to be preferential attack in the region of the coarse Al phase cells and the heat affected zone (HAZ). The largest pit (1–2 μm diam.) is seen in the center that was formed from the dissolution of several of the coarse Al cells leaving behind a separated Si phase network. The red boxed area in (A) is shown at higher magnification in (B). Investigation of the damage in this region leads to the conclusion that the initial degradation starts with solution penetration at the interface between the Al cell and the Si network. Initial degradation leads to detachment of the Si phase thus exposing more Al for dissolution. Progressively, the bulk Al becomes susceptible to further corrosion. Within the pit, there are remnants of the Si network exposed by the preferential dissolution of Al. A trail of corrosion damage to the right of the pit is shown in greater detail in (C). Trenching along the Si network goes from left to right across the micrograph and then turns downward. The features in (C) reveal the early stages of intergranular alloy attack at the interface between the Al cell and the surrounding Si network. Similar corrosion patterns have been reported for this alloy in a different electrolyte solution.[6,31,42] The fact that the SLM-prepared alloys do not consist of distinct segregated Si-Mg phases, as is the case for the die cast alloy, is a reason the former are more corrosion resistant.[6,31,42,47]

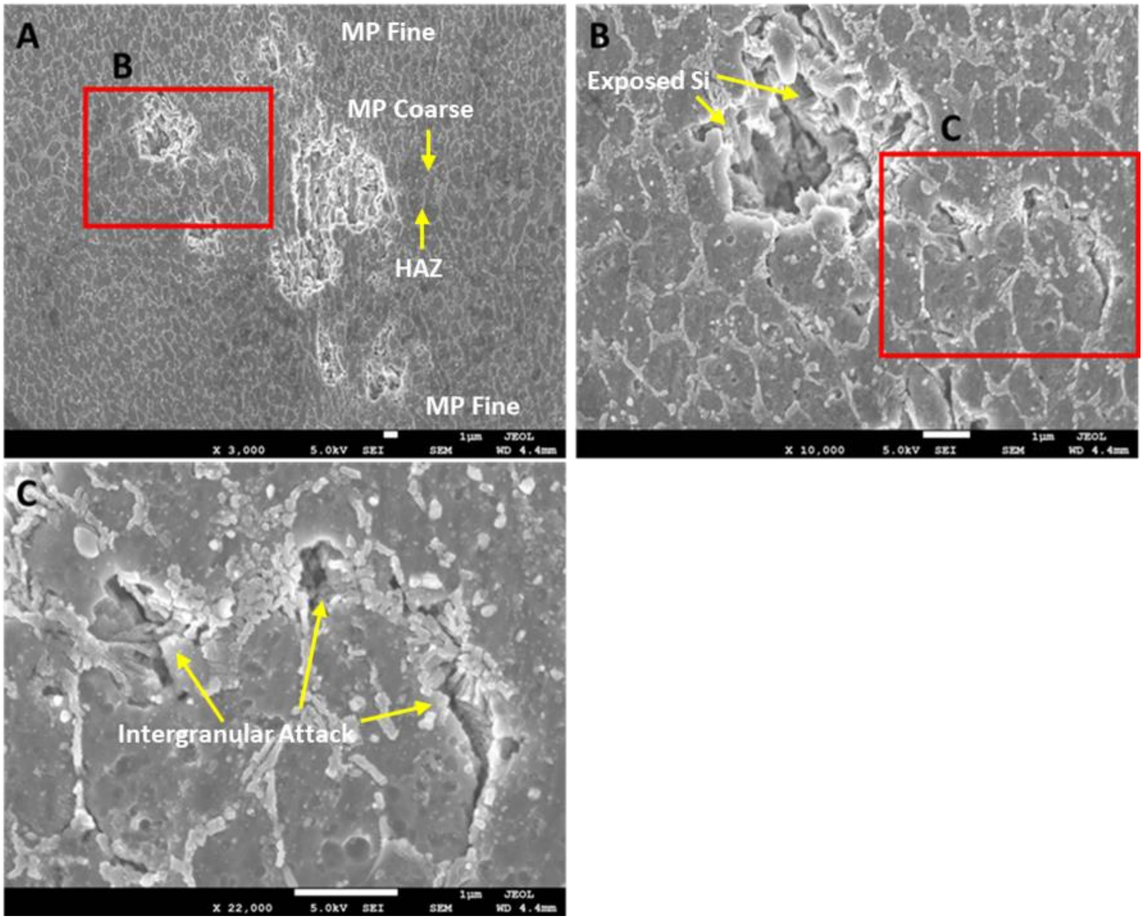

**Figure 4.18.** Scanning electron micrographs (A) of a smoothed and etched A360 aluminum alloy specimen (X-Z plane) after one anodic polarization scan from 0.02 V negative of the OCP to 1.0 V vs Ag/AgCl in naturally aerated 0.5 M $Na_2SO_4$ + 0.01 M NaCl. Scan rate = 1 mV/s. (B) Electron micrograph of the boxed region in (A), 10,000×, showing pitting corrosion and Si exposure. (C) Electron micrograph of the boxed region in (B), 22,000×, showing intergranular corrosion along the Si network. Abbreviations- MP (melt pool), and HAZ (heat affected zone).

Figure 4.19 shows scanning electron micrographs for a more advanced case of corrosion damage after a single anodic polarization scan to 1.0 V. Corrosion has spread across the edge of the melt pool in the coarse grain structure. The deepest part of the pit is in the middle of the damaged area. The darker regions on the right side of the micrograph adjacent to the damaged area may be remnants of corrosion product not fully removed by the ultrasonic cleaning. A micrograph of the red boxed area in (A) is presented in (B). The image is blurry in the bottom corner because the features are below the focal plane. Spreading from the lower left to the upper right is intergranular damage with trenches opening into deeper pits. The Al phase dissolution occurs at the interface with the Si phase network.

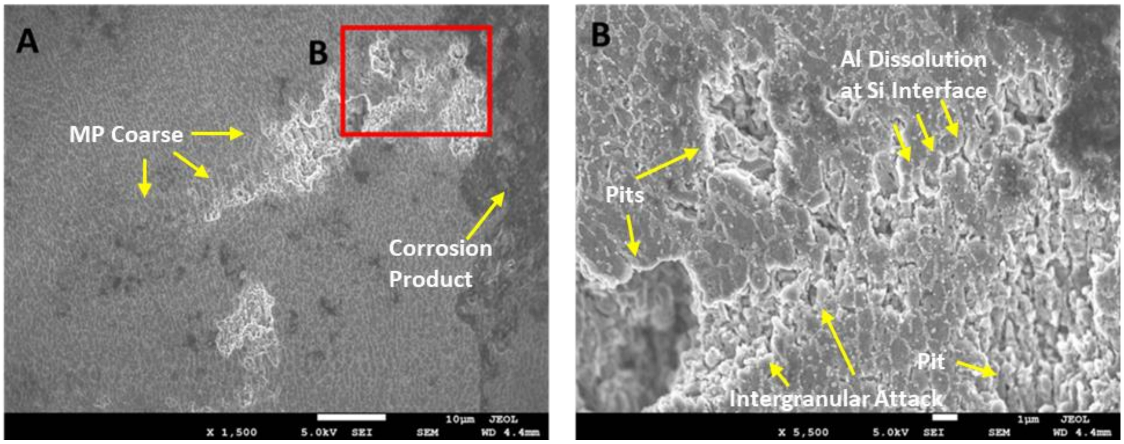

**Figure 4.19.** Scanning electron micrographs (A) of a smoothed and etched A360 aluminum alloy specimen (X-Z plane) after one anodic polarization scan from 0.02 V negative of the OCP to 1.0 V vs Ag/AgCl in naturally aerated 0.5 M $Na_2SO_4$ + 0.01 M NaCl. Scan rate = 1 mV/s. (B) Electron micrograph of the boxed region in (A) at 5,500×, showing enhanced corrosion damage along the MP coarse region. Abbreviation- MP (melt pool).

*Neutral salt spray testing of uncoated and TCP-coated alloy specimens*

The corrosion resistance of uncoated and TCP-coated A360 specimens was assessed during a 14-day neutral salt-spray exposure performed according to ASTM B117.[37] The TCP-coated specimens were first degreased and deoxidized and then surface finished with a TCP coating formed by a 15-min immersion at room temperature. No abrading or polishing was used to smooth the surface prior to conversion coating. The uncoated specimens were pulled from the test after just 7 days due to the extensive and widespread degradation that developed across the surface in the form of localized pitting corrosion. Figure 4.20 presents digital optical micrographs of a 2 × 2 $in^2$ A360 specimen (A) before and (B) after 7 days. The optical micrographs of both exhibit light and dark areas due to reflection differences caused by the rough surface texture. The lighter areas are generally raised features, while the darker areas are depressed. For the salt-spray exposed specimens, some of the darker regions are associated with corrosion damage caused by localized pitting and alloy dissolution. There is an increase in the number of these darker areas across the entire alloy specimen after exposure to the salt environment. A few of these localized areas of pitting corrosion have been identified with arrows in Figure 4.20B. Widespread corrosion damage and discoloration over the full surface, consistent with Stage 3 corrosion damage, was observed on all uncoated specimens by the 7-day mark. Where the corrosion damage tends to initiate on this alloy surface has not yet been ascertained, but it is expected that these sites are associated with microvoids or cracks in the alloy and or the tranistion zones between the melt pools.[4,8–10,13] Furthermore the corrosion damage may initiate at the interface between the aluminum grains and the continuous Si phase network that forms around the grains. This is because of a more defective and discontinuous oxide layer formed on the aluminum near this interface.

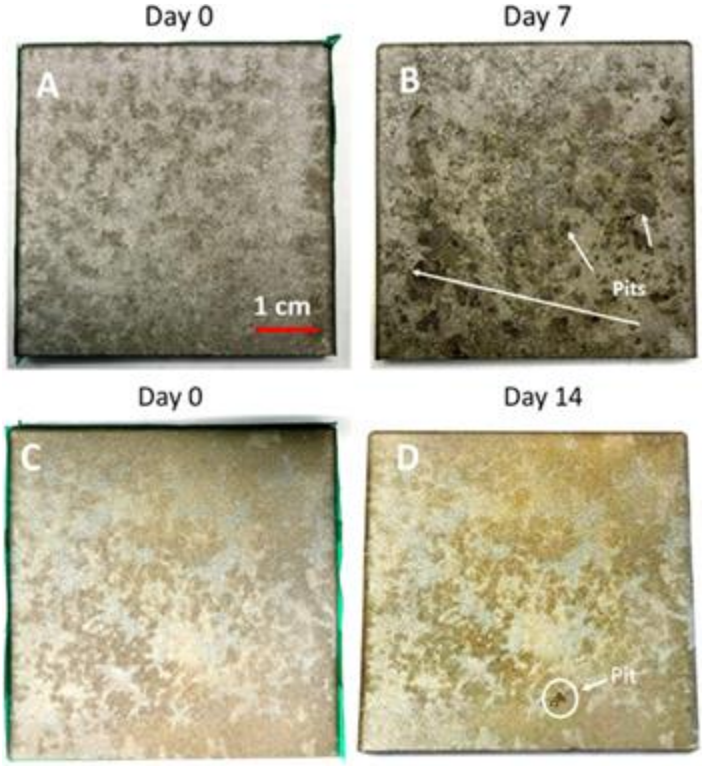

**Figure 4.20.** Digital optical micrographs of a 2 × 2 in Ref. 2 uncoated A360 aluminum alloy specimen (X-Z plane) (A) before and (B) after 7 days of neutral salt-spray exposure according to ASTM B117. Micrographs are also presented for a TCP-coated specimen (C) before and (D) after 14 days of salt-spray exposure. The TCP coating was formed by a 15 min immersion in the coating bath at room temperature.

Figure 4.20C and D are digital optical micrographs of a 2 × 2 in$^2$ TCP-coated A360 specimen before and after 14 days of salt spray exposure. The light reflection pattern off the TCP-coated specimen before exposure is distinctly different from that of the uncoated specimen. The lighter, more reflective areas are more widespread due to the presence of the conversion coating. The conversion coating appears to form over most regions of the alloy surface based on the reflection pattern. Importantly, there is little difference in the optical micrographs before and after the 14-day exposure. The key finding is that the TCP coating provides good stand-alone corrosion resistance to the alloy, consistent with the electrochemical data. Exposure times longer than 14 days were not studied. For this specimen, only three corrosion pits were detected with one of these damage areas circled in white in Figure 4.20D. The very minor surface degradation is consistent with Stage 1 or very early Stage 2 corrosion damage (U.S. Army Material Command scale). The sides and back of the specimens were taped so all corrosion damage and mass loss occurred only on the exposed surface.

Table 4.4 summarizes weight loss data for the uncoated and TCP-coated alloy specimens after the salt spray exposure. The uncoated specimen data are for a 7-day exposure while the TCP-coated specimen data are for a 14-day exposure. All weight loss metrics are significantly lower for the TCP-coated specimens indicative of the corrosion resistance provided by the coating. The nominal weight loss, based as a percentage of the initial specimen weight, for the TCP-coated specimens was a factor of 6× lower. The weight loss represented as the weight change normalized to the area of the exposed surface (2 in. × 2 in. = 25.8 $cm^2$) is 6.5× lower for the TCP-coated specimens. The corrosion intensity, which takes into account the salt-spray exposure time, is 12.5× lower for the TCP-coated specimen. The 3D contour plots of the digital micrographs allows for pit depths to be estimated. This kind of image analysis is challenging since the surface texture of the SLM alloys as-prepared is quite rough. Even so, the estimated nominal pit depth for the uncoated specimens was 27 μm and was 20 μm for the TCP-coated specimens, again consistent with the corrosion resistance provided by the TCP coating. The overall corrosion damage is Stage 3 for the uncoated specimens and Stage 1–2 for the TCP-coated specimens (U.S. Army Material Command scale).

**Table 4.4.** Summary of weight loss data for the uncoated (7 days) and TCP-coated (14 days) A360 alloy specimens after neutral salt spray exposure. Values reported as mean ± standard error of the mean. Statistical significance was assessed using an unpaired, one-tailed Student's t-test ($P < 0.01$) with the uncoated data serving as the control.

| | Uncoated | 15 min TCP |
|---|---|---|
| Weight loss (%) | 0.036 ± 0.004% | 0.006 ± 0.001%* |
| Weight loss (μg/cm$^2$) | 588 ± 59 | 91 ± 9* (6× lower) |
| Corrosion intensity (g/m$^2$-year) | 310 ± 31 | 24 ± 2* (13× lower) |
| Estimated pit depth | 26.9 ± 2.0 | 20.2 ± 1.3* |
| Corrosion damage | Stage 3 | Stage 1-2 |

## 4.5 Discussion

The results reported herein reveal that the as-prepared A360 aluminum alloy specimens fabricated by SLM possess a rough surface texture, even after the mechanical (sand blasting) and solution cleaning that was applied before the specimens arrived at MSU. The surface roughness of the specimens, $S_q$, was 18 ± 2 μm with a peak-to-valley maximum height, $S_z$, of 105 ± 12 μm. The property profile of the feedstock powder (chemical composition, particle microstructure, and particle size), the powder feed rate and layer thickness, laser scan speed, and laser energy density control the surface texture and microstructure of the SLM alloys. The specimen density correlates with the mechanical properties (microhardness and tensile strength) and is controlled by how well the metal particles fuse together during the build and the number of resulting micro voids and pores. A mechanical property of the A360 specimens assessed was the Vickers microhardness. A nominal hardness of 137 ± 1 VH (1 specimen and 5 spots) was observed for a typical SLM A360 specimen. This nominal value compares favorably with hardness values reported in the literature for other SLM-prepared A360 alloys ranging from 110–150 VH.[6,39] The microhardness increases linearly with the alloy density and, based on published data (see Fig. 5B of Ref. 6), the density of the A360 specimens used herein is on the order of 2.68 g/cm$^3$.[6] This density was confirmed by our own measurements. The reported density of die-cast A360 is 2.63 g/cm$^3$. Therefore, the specimen build conditions used herein (laser, hatch spacing, powder layer thickness, and laser scan velocity) are optimum for forming a near-fully dense alloy. X-ray computed microtomography images (data not presented) of the specimens revealed a fully dense material with no internal voids or pores.

The microstructures of die-cast and SLM A360 aluminum alloys are quite distinct.[4,9,39,41,46] The microstructure of the SLM prepared specimens discussed herein, as well as A360 alloy specimens produced by SLM reported on in the literature, consist of a cellular dendritic organization with α-Al cellular grains (1–2 μm diam. in long dimension) and a continuous Si phase formed at the intercellular regions. This microstructure is revealed only with polishing and tint etching. There are no distinct Mg or Si-Mg secondary phases detected. The Mg appears to fully dissolve in the Al matrix and does not form secondary phases with other elements. Some course flakes of Si were detected on the surface after abrading and polishing. We did not study die cast alloys, but in the literature, it has been reported that such alloys possess a microstructure consisting of an α-Al matrix, coarse Si flakes, and second-phase particles including β-AlFeSi, α-AlFeSiMg and AlMgSiCu.[9]

A primary goal of this work was to evaluate the electrochemical properties of as-prepared A360 alloy surfaces with and without a trivalent chromium process (TCP) conversion coating. The electrochemical data reveal that the OCP of the uncoated specimens in naturally aerated 0.5

M $Na_2SO_4$ + 0.01 M NaCl is nominally −580 ± 17 mV vs Ag/AgCl. This nominal value is about the same as the OCP for AA2024-T3 (−495 ± 7 mV) in naturally aerated 0.5 M $Na_2SO_4$ + 0.05 M NaCl and a little more positive of the values for AA6061-T6 (−616 ± 7 mV) and AA7075-T6 (613 ± 6 mV).[22,45] The polarization resistance ($R_p$) for the as-prepared A360 specimens (8 × 104 $\Omega\cdot cm^2$) is similar the values for AA2024-T3, AA6061-T6 and AA7075-T6 in the same electrolyte solution, 3–6 × $10^4$ $\Omega\cdot cm^2$.[22,45]

The TCP coating formed by immersion on as-prepared A360 alloy specimens provides corrosion suppression like that observed for other wrought aluminum alloys.[18–22,24–30,40,44,45] The formation can be tracked temporally in situ by measuring the OCP of the alloy during the immersion formation. Based on the data in hand currently, mechanistically the coating appears to form on A360 in a manner like wrought alloys. During immersion, the native oxide layer is initially dissolved exposing the underlying metal. The OCP of the specimen during this process is well positive of the $E^0$ value for $Al/Al^{+3}$, so the metal begins oxidizing at a higher rate. To compensate for the increased anodic reaction rate, the OCP of the specimen shifts toward more negative potentials to increase the rate(s) of the counter-balancing cathodic reactions, dissolved oxygen reduction and water reduction; both of which lead to more alkaline conditions in the interfacial region. This leads to the precipitation of the conversion coating ($ZrO_2\cdot nH_2O$ and $Cr(OH)_3$) over an aluminofluoride-rich interfacial layer. XPS survey scans and depth profiling need to be performed to investigate the coating thickness and elemental composition spatially and with depth.

Electrochemically, the TCP conversion coating formed on A360 suppresses both anodic and cathodic currents but has a slightly greater effect on inhibiting the cathodic reaction(s) kinetics as the OCP shifts negative by 40–80 mV after coating. This is similar to the literature reports showing the TCP conversion coating provides both anodic and cathodic corrosion protection to aluminum alloys including the AlSi10Mg alloy used herein.[18–22,24–30,40,44,45] Taken together, the electrochemical data reported herein reveal the degree of corrosion suppression is similar for TCP formed at all three immersion times studied (10, 15 and 20 min). The anodic and cathodic current densities measured in potentiodynamic polarization curves at −0.1 and −0.8 V vs Ag/AgCl, respectively, were 2–14× lower for all the TCP-coated alloys, as compared to the uncoated as-prepared alloy. The $R_p$ values, determined from LPR measurements, were higher by 25–40× for all the TCP-coated alloys, as compared to the uncoated alloy. The $R_p$ values for the TCP-coated $AlSi_{10}Mg$ alloys, 212–306 $k\Omega\cdot cm^2$, agree with the values for TCP-coated AA2024-T3, AA6061-T6 and AA7075-T6 in 0.5 M $Na_2SO_4$ + 0.05 M NaCl, which are in the high $10^5$ to low $10^6$ $\Omega\cdot cm^2$ range.[22,45] TCP increases $R_p$ on the wrought allows by 10–100×, depending on the alloy. The lesser increase seen for the $AlSi_{10}Mg$ alloys maybe be due to the surface roughness that affects the integrity of the coating across the surface. The values reported for the wrought alloys are for specimens pretreated by abrading and polishing as well as solution processing. A rough surface will be less effectively coating with a continuous and low defect coating than a smooth surface will be. Therefore, improved corrosion suppression is expected for alloys with a smoother surface texture.

Uncoated AlSi10Mg specimens were examined after a single potentiodynamic polarization scan from the OCP to 1.0 V vs Ag/AgCl, which is well into the region where the oxide passivation layer breaks down occurs, and localized pitting commences. SEM micrographs indicate the corrosion degradation commences with solution penetration at the interface between the Al cells and the surrounding Si phase network. This leads to dissolution of the Al and separation of the Si phase, thus exposing more Al surface area for dissolution. Trenching occurs by dissolution of the along the Si phase network. Neutral salt-spray exposure for 14-days was used to assess the stand-alone corrosion resistance of the TCP-coated and uncoated as-prepared specimens. Digital optical microscopy revealed clear regions of localized damage on the uncoated AlSi10Mg alloy after just 7 days of exposure. Significantly less damage was observed on the TCP-coated specimens after a 14-day exposure. The percent weight loss for the TCP-coated specimens was 6× lower after 14 days than the weight loss for the uncoated specimens after just 7 days. The weight loss normalized to the specimen area exposed (μg/cm$^2$) is 6–7× lower for the TCP-coated specimens. The corrosion intensity (g/m$^2$-year) for the TCP-coated specimens is 10–11× lower than the values for the uncoated control specimens. Taken together, these metrics of corrosion are consistent with the electrochemical data, and all indicate TCP coatings form on the rough, as-prepared $AlSi_{10}Mg$ SLM alloys and provide good stand-alone corrosion resistance. The corrosion damage on the as-prepared specimens was rated Stage 3 after 7 days of salt spray exposure while the damage on the TCP-coated specimens was Stage 1 or very early Stage 2. The degree of corrosion suppression was similar for all the TCP-coated specimens regardless of the immersion time.

## 4.6 Conclusions

This work reports on the surface texture and microstructure of as-prepared $AlSi_{10}Mg$ (A360) alloys prepared by selective laser melting (SLM). The electrochemical properties of the as-prepared alloys were investigated in naturally-aerated 0.5 M $Na_2SO_4$ + 0.01 M NaCl. The effect of a TCP conversion coating on the electrochemical properties of the alloy was studied in the same electrolyte to learn how much corrosion suppression is provided by the surface treatment. Finally, the oxidative degradation of uncoated as-prepared and TCP-coated specimens was examined by microscopy after a single potentiodynamic scan to a potential at which the passivating oxide layer breaks down and localized pitting corrosion occurs and by microscopy and weight loss metrics before and after a 14-day neutral salt-spray exposure. The key findings from the work are summarized as follows:

1. The as-prepared alloys possess a rough surface texture. Based on the analysis of 5 spots (grid pattern and image size of $10^6$ $\mu m^2$) of a single specimen, the surface roughness was found to be 18 ± 2 μm with a maximum peak-to-valley dimension of 105 ± 12 μm.
2. The microhardness measurements of the as-prepared specimen is 137 ± 1 HV. This nominal value was obtained over five spots on one polished specimen. The density is 2.63 $g/cm^3$. The hardness values are consistent with other hardness data reported in the literature for this AM alloy. The low variability across the specimens suggests that the alloys are fully dense and that the density is uniform throughout the part.
3. Immersion times of 10, 15 and 20 min produced TCP coatings on the as-prepared alloy surface that provide equivalent levels of corrosion suppression.
4. Open circuit potential (OCP) values for the as-prepared alloy specimens are similar or slightly negative (−40 to −80 mV) after TCP coating. This means that the conversion coating has a slightly greater effect on inhibiting the cathodic (oxygen reduction) than the anodic (aluminum oxidation) reaction kinetics.
5. Anodic and cathodic currents in potentiodynamic polarization curves were recorded in naturally-aerated 0.5 M $Na_2SO_4$ + 0.01 NaCl. The measurments reveal a nominal anodic current for the uncoated specimens at –0.1 V of 16.8 ± 3.3 $\mu A/cm^2$. The current for the TCP-coated specimens is lower by a factor of 2–11× ranging from 1.5 − 7.4 $\mu A/cm^2$. The

nominal cathodic current for the uncoated specimens at –0.8 V is –5.6 ± 1.1 μA/cm$^2$ and is lower by a factor of 3–14× ranging from –0.38 – –1.7 μA/cm$^2$ for the TCP-coated specimens. Similar levels of anodic and cathodic current reduction are observed for TCP coatings formed at all three immersion times (10, 15 and 20 min). This means the conversion coating suppresses both the anodic and cathodic reaction kinetics, as is the case for other wrought aluminum alloys.

6. Polarization resistance values, $R_p$, determined from linear polarization curves are 8.11 ± 0.95 kΩ·cm$^2$ before and increase by a factor of 25–40× ranging from 212 − 306 kΩ·cm$^2$ after TCP coating. Similar increases in $R_p$ are observed for the TCP coatings formed at all three immersion times. These data indicate the TCP coating reduces the rate of alloy corrosion.
7. Studies of the early stages of electrochemical corrosion under controlled potential polarization to a positive limit of 1.0 V vs Ag/AgCl on the uncoated alloy reveal degradation proceeding initially through an inner granular mechanism with chemical attack at the interface between the Al cells and the surrounding Si-phase network.
8. Weight loss metrics all indicate corrosion suppression by the TCP conversion coating during exposure to a neutral salt-spray environment. The weight loss normalized to the specimen area exposed (μg/cm$^2$) is 6–7× lower for the TCP-coated specimens. The corrosion intensity (g/m$^2$-year) for the TCP-coated specimens is 10–11× lower than the values for the uncoated control specimens after neutral salt spray exposure. TCP coatings formed at all three immersion times yielded similar results. It appears the corrosion damage on the uncoated specimens initiates at the interface between the aluminum grains and the continuous Si phase network that forms around the grains. This is because of a

more defective and discontinuous oxide layer formed on the aluminum near this interface.

## 4.7 Acknowledgements

This research was generously supported by the Department of Energy's Kansas City National Security Campus managed by Honeywell FM&T through contract # N000380317. The authors would like to thank Dr Carl Boehlert and his graduate student, Sujoy Saha, in the Department of Chemical Engineering and Materials Science at MSU for their assistance with the microindentation hardness and density measurements, and some of the scanning electron microscopy.

# REFERENCES

1. Zhang H., Zhu H., Qi T., Hu Z. and Zeng Z., Selective Laser Melting o High Strength Al-Cu-Mg Alloys: Processing, Microstructure and Mechanical Properties, *Mater. Sci. Engr. A*, 656, 47 (2016).

2. Gorsse S., Hutchinson C., Gouné M. and Banerjee R., Additive Manufacturing of Metals: A Briev Review of the Characteristic Microstructures and Properties of Steels, Ti-6Al-4V and High-entropy Alloys, *Sci. Technol. Adv. Mater.*, 18, 584, (2017).

3. Martin J. H., Yahata B. D., Hundley J. M., Mayer J. A., Schaedler T. A. and Pollock T. M., 3D Printing of High-Strength Aluminium Alloys, *Nature*, 549, 366, (2017).

4. Sander G., Tan J., Balan P., Gharbi O., Feenstra D. R., Singer L., Thomas S., Kelly R. G., Scully J. R. and Birbilis N., Corrosion of Additively Manufactured Alloys: A Review, *Corrosion*, 74, 1318, (2018).

5. Zhang D., Sun S., Qiu D., Gibson M. A., Dargusch M. S., Brandt M., Qian M. and Easton M., Metal Alloys for Fusion-Baed Additive Manufacturing, *Adv. Engr. Mater.*, 20, 1700592 (2018).

6. Teng X., Zhang G., Liang J., Li H., Liu Q., Cui Y., Cui T. and Jiang L., Parameter Optimization and Microhardness Experiment of AlSi10Mg Alloy Prepared by Selective Laser Melting, *Mater. Res. Express*, 6, 086592, (2019).

7. Zhang C., Zhu H., Qi Y. and Zeng X., The Effect of Annealing on Microstructure and Mechanical Properties of Selective Laser Melting AlSi10Mg, *IOP Conf. Series: Mater. Sci. Engr.*, 538, 012023, (2019).

8. Fathi P., Rafieazada M., Duana X., Mohammadi M. and Nasiri A. M., On Microstructure and Corrosion behaviour of AlSi10Mg Alloy with Low Surface Roughness Fabricated by Direct Metal Laser Sintering, *Corros. Sci.*, 157, 126, (2019).

9. Fathi P., Mohammadi M., Duan X. and Nasiri A. M., A Comparative Study on Corrosion and Microstructure of Direct Metal Laser Sintered AlSi10Mg_200C and Die Cast A360.1 Aluminum, *J. Mater. Proc. Technol.*, 259, 1, (2018).

10. Asgari H., Baxter C., Hosseinkhani K. and Mohammadi M., On Microstructure and Mechanical Propterties of Additively Manufactured AlSi10Mg_200C Using Recycled Powder, *Mater. Sci. Eng. A*, 707, 148, (2017).

11. Tang M. and Pistorius P. C., Oxides, Porosity and Fatigue Performance of AlSi10Mg Parts Produced by Selective Laser Melting, *Int. J. Fatigue*, 94, 192, (2017).

12. Rafieazad M., Fathi P., Mohammadi M. and Nasiri A., Effects of Laser-Powder Bed Fusion Process Parameters on the Microstructure and Corrosion Properties of AlSi10Mg Alloy, *J. Electrochem. Soc.*, 168, 021505, (2021).

13. Revilla R. I., Rybin C. A. and De Graeve I., On the Zr Electrochemical Conversion of Additively Manufactured AlSi10Mg: The Role of the Microstructure, *J. Electrochem. Soc.*, 168, 121502, (2021).

14. Townsend A., Senin N., Blunt L., Leach R. K. and Taylor J. S., Surface Texture Metrology for Metal Additive Manufacturing: A Review, *Precis. Eng.*, 46, 34, (2016).

15. Dardona S., Chen L., Kryzman M. and Jaworowski M., Polarization Controlled Kinetics and Composition of Trivalent Chromium Coatings on Aluminum, *Anal. Chem.*, 83, 6127, (2011).

16. Iyer A., Willis W., Frueh S., Nickerson W., Fowler A., Bames J., Hagos L., Escarsega J., La Scala J. and Suib S. L., Characterization of NAVAIR Trivalent Chromium Process (TCP) Coatings and Solutions, *Plat. Surf. Finish.*, 5, 32, (2010).

17. Dong X. C., Wang P., Argekar S. and Schaefer D. W., Structure and Composition of Trivalent Chromium Process (TCP) Films on Al Alloy, *Langmuir*, 26, 10833, (2010).

18. Li L. L., Swain G. P., Howell A., Woodbury D. and Swain G. M., The Formation, Structure, Electrochemical Properties and Stability of Trivalent Chrome Process (TCP) Coatings on AA2024, *J. Electrochem. Soc.*, 158, C274, (2011).

19. Guo Y. and Frankel G. S., Characterization of Trivalent Chromium Process Coatings on AA2024-T3, *Surf. Coat. Technol.*, 206, 3895, (2012).

20. Guo Y. and Frankel G. S., Active Corrosion Inhibition of AA2024-T3 by Trivalent Chrome Process Treatment, *Corrosion*, 68, 045002, (2012).

21. Li L., Desouza A. L. and Swain G. M., In situ pH Measurement During the Formation of Conversion Coatings on an Aluminum Alloy (AA2024), *Analyst*, 138, 4398, (2013).

22. Li L., Doran K. P. and Swain G. M., Electrochemical Characterization of Trivalent chromium Process (TCP) Coatings on Aluminum Alloys 6061 and 7075, *J. Electrochem. Soc.*, 160, C396, (2013).

23. Qi J., Walton J., Thompson G. E., Albu S. P. and Carr J., Spectroscopic Studies of Chromium VI Formed in the Trivalent Chromium Conversion Coatings on Aluminum, *J. Electrochem. Soc.*, 163 C367, (2016).

24. Munson C. A. and Swain G. M., Structure and Chemical Composition of Different Variants of a Commercial Trivalent Chromium Process (TCP) Coating on Aluminum Alloy 7075-T6, *Surf. Coat. Technol.*, 315, 15, (2017).

25. Li L., Whitman B. W. and Swain G. M., Characterization and Performance of a Zr/Ti Pretreatment Conversion Coating on AA2024-T3, *J. Electrochem. Soc.*, 162, C279, (2015).

26. Munson C. A., Zutim P. and Swain G. M., Electrochemical Characterization of Different Variants of a Commercial Trivalent Chromium Process (TCP) Coating on Aluminum Alloy 7075-T6, *Corrosion*, 74, 50, (2018)

27. Qi J., Gao L., Li Y., Wang Z., Thompson G. E. and Skeldon P., An Optimized Trivalent Chromium Conversion Coating Process for AA2024-T351 Alloy, *J. Electrochem. Soc.*, 164, C390, (2017)

28. Munson C. A., McFall-Boegeman S. and Swain G. M., Cross Comparison of TCP Conversion Coating Performance on Aluminum Alloys During Neutral Salt-Spray and Thin-Layer Mist Accelerated Degradation Testing, *Electrochim. Acta*, 282, 171, (2018).

29. Shruthi T. K. and Swain G. M., Role of Trivalent Chromium on the Anti-Corrosion Properties of a TCP Conversion Coating on Aluminum Alloy 2024-T3, *J. Electrochem. Soc.*, 165, C103, (2018).

30. Shruthi T. K. and Swain G. M., Detection of $H_2O_2$ from the Reduction of Dissolved Oxygen on TCP-Coated AA2024-T3: Impact on the Transient Formation of Cr(VI), *J. Electrochem. Soc.*, 166, C3284, (2019).

31. Cabrini M., Calignano F., Fino P., Lorenzi S., Lorusso M., Manfredi D., Testa C. and Pastore T., Corrosion Behavior of Heat-Treated AlSi10Mg Manufactured by Laser Powder Bed Fusion, *Materials*, 11, E1051, (2018).

32. ASTM B85-03 Standard Specification for Aluminum-Alloy Die Castings. Dec 31, 2010.

33. ASTM E384-17 Standard Test Method for Microindentation Hardness of Materials. June 1, 2017.

34. Gao L., Harada Y. and Kumai S., Microstructural Characterization of Aluminum Alloys Using Weck’s Reagent, Part I: Applications, *Mater. Character.*, 107, 426, (2015).

35. Gao L., Harada Y. and Kumai S., Microstructural Characterization of Aluminum Alloys using Weck’s Reagent, Part II: Coloring Mechanism, *Mater. Character.*, 107, 434, (2015).

36. Hirschorn B., Orazem M. E., Tribollet B., Vivier V., Frateur I. and Musiani M., Determination of Effective Capacitance and Film Thickness from Constant-Phase-Element Parameters, *Electrochim. Acta*, 55, 6218, (2010)

37. ASTM B117 Standard Practice for Operating Salt Spray (Fog) Apparatus. Oct. 1, 2011.

38. Ferrer K. and Kelly R., Comparison of Methods for Removal of Corrosion Product from AA2024-T3, *Corrosion*, 57, 110, (2001).

39. Aboulkhair N., Simonelli M., Parry L., Ashcroft I., Tuck C. and Hague R., 3D Printing of Aluminium Alloys: Additive Manufacturing of Aluminium Alloys Using Selective Laser Melting, *Prog. Mater Sci.*, 106, 100578, (2019).

40. Li L., Desouza A. L. and Swain G. M., Effect of Deoxidation Pretreatment on the Corrosion Inhibition Provided by a Trivalent Chromium Process (TCP) Conversion Coating on AA2024-T3, *J. Electrochem. Soc.*, 161, C246, (2014).

41. Aboulkhair N. T., Maskery I., Tuck C., Ashcroft I. and Everitt N. M., The Microstructure and Mechanical Properties o Selectively Laser Melted AlSi10Mg: The Effect of a Conventional T6-Like Heat Treatment, *Mater. Sci. Engr: A*, 667, 139, (2016).

42. Cabrini M., Lorenzi S., Pastore T., Pellegrini S., Ambrosio E. P., Calignano F., Manfredi D., Pavese M. and Fino P., Effect of Heat Treatment on Corrosion Resistance of DMLS AlSi10Mg Alloy, *Electrochim. Acta*, 206, 346, (2016).

43. Rafieazad M., Mohammadi M. and Nasiri A. M., On Microstructure and Early Stage Corrosion Performance of Heat Treated Direct Metal Laser Sintered AlSi10Mg, *Addit. Manuf.*, 28, 107, (2019).

44. Li L. and Swain G. M., Effects of Aging Temperature and Time on the Corrosion Protection Provided by Trivalent Chromium Process Coatings on AA2024-T3, *ACS Appl. Mater. Interfaces*, 5, 7923, (2013).

45. Li L. and Swain G. M., Formation and Structure of Trivalent Chromium Process Coatings on Aluminum Alloys 6061 and 7075, *Corrosion*, 69, 1205, (2013).

46. Kubacki G. W., Brownhill J. P. and Kelly R. G., Comparison of Atmospheric Corrosion of Additively Manufactured and Cast Al-10Si-Mg Over a Range of Heat Treatments, *Corrosion*, 75, 1527, (2019).

47. Zhu Y., Sun K. and Frankel G. S., Intermetallic Phases in Aluminum Alloys and Their Roles in Localized Corrosion, *J. Electrochem. Soc.*, 165 C807, (2018).

# CHAPTER 5 - The Effect of Sulfuric Acid Anodization on the Electrochemical Properties of Aluminum Alloy $AlSi_{10}Mg$ Prepared by Selective Laser Melting

Chapter submitted to *J. Electrochem. Soc.*, August 4, 2023.

*Article: Jack W. Walton, Jonathan H. Dwyer, Lucas Rice, Zachariah Rueger and Greg M. Swain- The Effect of Sulfuric Acid Anodization on the Electrochemical Properties of Aluminum Alloy* $AlSi_{10}Mg$ *Prepared by Selective Laser Melting*

## 5.1 Abstract

Aluminum alloy, $AlSi_{10}Mg$, prepared by selective laser melt (SLM) fabrication was anodized in 9.8 % sulfuric acid (Type II) at 15 V for 23 min. Experiments were performed to study the potentiostatic anodization process and its effects on the oxide coating morphology, thickness, and electrochemical properties of the alloy. Prior to anodization, the alloy microstructure is composed of aluminum cells encapsulated in a silicon network, as commonly reported for the SLM process. Anodizing the abraded and polished AlSi10Mg surface produced a porous oxide layer with a thickness of 5 μm. The oxide coating weight was 698 ± 29 mg/ft$^2$ for the anodization conditions used, as determined by the ASTM B137 method. The oxide coating forms in the aluminum cells that are isolated from one another by the Si phase. In electrochemical tests, the anodic and cathodic potentiodynamic polarization currents were suppressed by factors of 15× and 215×, respectively, as compared to the unanodized controls. The data indicate the anodic oxide coating suppresses the cathodic more than the anodic reaction rate, but generally serves to reduce the active area available for both reactions. Linear polarization resistance ($R_p$) values increased by 279× after anodization. The corrosion current density values ($j_{corr}$) decreased by 133× after anodization. Taken together, the electrochemical

data indicate the anodic oxide coating (unsealed) increases the corrosion resistance of the SLM alloy by two orders of magnitude.

## 5.2 Introduction

There is a growing desire for higher complexity in component design and more efficient use of raw materials with less waste. To this end, additive manufacturing (i.e. 3D printing) is growing in use.[1] Advantages of additive manufacturing are three-fold: (i) bottom-up preparation of components producing less material waste, (ii) production of complex designs in less time than is needed for conventional top-down machining, and (iii) the ability to prepare materials with improved mechanical properties or corrosion resistance through single powder additions and layer-by-layer fabrication.[2] Selective laser melting (SLM, a.k.a. direct metal laser sintering, laser powder bed fusion) is one type of advanced manufacturing method for creating metal parts with a high degree of precision and freedom in design without any subtractive machining.[1–4] SLM uses a high-powered laser to fuse thin layers of pre-alloyed metal powder. After each layer is created (powder applied + laser melting and particle fusion), a new bed of powder is added on top of the build and fused to create near-fully dense parts. Research is needed to understand (i) how the fabrication parameters influence the material density, defect density, microstructure, and corrosion susceptibility and (ii) how different surface pretreatments and finishes are optimally applied to mitigate corrosion most effectively. These structure-function relationships have been established for wrought and die-cast alloys but are still to be determined for additively manufactured materials.

Aluminum alloy, AlSi10Mg (a.k.a. A360), fabricated by SLM is a commonly researched aerospace material.[5–10] The corrosion of SLM A360 tends to initiate at the melt pool boundaries because of the galvanic difference between the electrically connected Al and Si phases.[8] Fathi et al. and Rafieazad et al. have demonstrated that varying the fabrication parameters can be tuned to affect the corrosion behavior.[7,10] Post-fabrication processes are a possible solution to improve the corrosion resistance of the metal. Heat treatments have been studied to show the effect of the microstructure on the corrosion behavior.[9] Likewise, the surface roughness and finishing will affect the corrosion performance.[11] The corrosion damage tends to propagate along the melt pool boundaries. This leads to pitting corrosion that bores below the surface.[7–10] Pitting corrosion is deleterious to part longevity and mechanical strength, so ways of effectively protecting the metal from this type of localized corrosion are needed. Surface finishes (i.e., coatings) are typically applied to mitigate and control corrosion. Solution processing and conversion coating was studied by Revilla et al. wherein the coating provides a thin protective film that increases the corrosion resistance.[12] The authors' previous work and others also reports an increase in corrosion resistance of SLM A360 coated with a conversion coating.[13]

Anodization of aluminum alloy is a surface treatment that can be used to increase the corrosion resistance and add wear resistance.[14] Anodization produces a porous oxide coating that is several micrometers thick. In addition to passivating the alloy surface, the oxide coating provides an efficient base for bonding to primer and paint overlayers (i.e., adhesion promotion). The military standard for anodizing aluminum alloys is MIL-A-8625F.[15] Military specification MIL-A-8265F categorizes anodizing by the acid solution. Type I and Type II are both used for corrosion resistance. Chromic acid (Type I) has been effectively used to produce oxide coatings with a high degree of corrosion resistance.[16] However, chromate is toxic and an environmental hazard, so alternative acids are used including H2SO4 (Type II).[14,17]

Anodizing is performed electrolytically in an acid bath with the aluminum part acting as the anode. An external power source drives the electrochemical oxidation of aluminum and generates an oxide layer that grows into the bulk metal and forms a coating over the surface. The oxide coating functions as a physical barrier to solution contact with the underlying alloy. At the oxide/alloy interface, there is a barrier layer that is comprised of a densely formed aluminum oxide (≈10 nm).[17] Atop the barrier layer is a porous oxide layer that is comprised of nano-scale pores. Throughout the anodizing process, the aluminum matrix is oxidized to $Al^{3+}$ and the ions react with $H_2O$ to form solid, porous $Al_2O_3$. The porous layer grows downward into the alloy during anodization and the structure and pore size is dependent on the anodizing conditions (voltage, time, and current density) and the alloy structure and composition.[26] As the anodizing time increases, the oxide layer grows deeper into the material with the pores acting as channels for oxygen and electrolyte through the oxide and down to the barrier layer.[18] In practice, the pores are then closed, or "sealed" by a chemical soak, conversion coating, or hot water immersion.[19–22] A properly sealed anodized layer provides outstanding corrosion resistance by acting as an inert barrier on the scale of several microns in thickness. Aluminum anodizing and corrosion testing has been researched on 2XXX wrought alloys,[20–23] die-cast Al-Si alloys,[24,26] and other aerospace aluminum alloys.[14,17,19,25]

With the emergence and use of advanced metal manufacturing, it is important to study anodic coating formation on the new generation materials. To the authors' knowledge, the first literature report of Type II anodization of SLM $AlSi_{10}Mg$ was published by Revilla et al. in 2017.[26] They demonstrated that the SLM alloy can be anodized galvanostatically. Subsequent studies focused on understanding the effects of the Si content, the microstructure of the alloy and the effect of heat treatment on the formation and morphology of the oxide coating.[27–29] These studies compared $AlSi_{10}Mg$ specimens prepared by SLM and traditional die casting. A critical review by Revilla and coworkers on the corrosion protection of additively manufactured aluminum alloys calls for additional studies of AlSi10Mg anodizing, namely in the potentiostatic modality.[30]

We report herein on the Type II anodization of SLM $AlSi_{10}Mg$ potentiostatically. We investigated the oxide coating morphology and its effect on the electrochemical properties of the alloy, as compared to the unanodized specimens. The oxide coating morphology and thickness were studied by scanning electron microscopy (SEM) and energy dispersive X-ray spectroscopy (EDXS). The changes in electrochemical properties brought about by the oxide coating were assessed in naturally aerated 0.5 M $Na_2SO_4$ + 0.01 M NaCl.

## 5.3 Experimental

*Specimen Fabrication and Microstructure*

Specimens were fabricated using a SLM*500 industrial 3D printer (SLM Solutions, Germany). The feedstock powder, build parameters, and part cleaning before shipment to MSU have been described in detail in a previous report.[13] The specimens were printed from $AlSi_{10}Mg$ source alloy powder with a diameter ranging from 25-65 μm. In total, 10% of the particles were less in diameter than 26 μm, 50% less than 40 μm, and 90% less than 63 μm. According to ASTM B85 (Standard Specification for Aluminum Alloy Die Castings), this alloy powder has the following elemental composition (wt. %): Cu (0.6), Mg (0.4-0.6), Fe (≤ 1.3), Sn (≤ 0.10), Ni (≤ 0.5), Zn (≤ 0.5), Mn (≤ 0.35), Si (9.0-10.0) and Al (balance). No measurements of the powder were made to determine the elemental composition.

The SLM processing involves melting and fusing metallic powder particles together with a high-power laser beam scanned across the build surface. Once a layer of solid metal is created, the tray holding the specimen is lowered and powder is layered over the top. This is followed by the laser-assisted melting and fusing of the particles to form the new layer. All specimens were prepared with the following dimensions: 2.54 cm (length) × 2.54 cm (height) × 0.635 cm (thickness), such that the large face (length × height) is the XZ plane orthogonal to the build plane. The SLM system uses 3D optics and four lasers (350W and 1070 nm) to produce parts with a maximum build space of 500 × 250 × 365 mm. The inert gas used in the chamber during the specimen builds is Ar to limit oxygen reactivity with the heated aluminum. The following parameters were used for part fabrication: laser power = 350 W, hatch spacing = 130 μm, powder layer thickness = 30 μm, and laser scan velocity = 1650 mm/s.

Specimen post processing consisted of wire electric discharge machining (EDM), media blasting, and cleaning. No thermal annealing was applied to the fabricated specimens. The wire EDM step removes the parts from the build plate. The media blast step helps remove semi-sintered particles from the specimen and provides a matte finish to the exterior. The alloy specimens were blasted with sand at a pressure from 50-70 psi to remove loose powder particles. Cleaning was then performed consisting of the five general steps: (i) high pressure spray with detergent and rinse with water, (ii) ultrasonication in detergent followed by a water rinse, (iii) ultrasonication detergent followed by a rinse and drying with a stream of $N_2$ gas, (iv) vacuum oven drying and (v) packaging the cooled specimens into a nylon bag. This constituted the "as-received" specimens.

### *Specimen Preparation Prior to Anodization*

The as-received specimens were abraded with P1500 grit aluminum oxide grinding paper and polished down with 0.3 μm diam. $Al_2O_3$ powder followed by an ultrasonic cleaning (5 – 15 min) with ultrapure water to remove polishing debris. The specimens were then cleaned by immersion in Turco 6849 (20 vol.%), at 55 °C for 10 min. The specimens were then continuously rinsed with city tap water for 2 min. Deoxidation was then performed by immersion in Turco Smut-Go (20 vol.%) at room temperature for 2 min followed by rinse cleaning in city tap water for 2 min. Afterward, the specimens were dried with low pressure $N_2$ gas. The cleaned and dried specimens were then used shortly thereafter for anodization.

### *Type II Sulfuric Acid Anodization*

Specimens were anodized in 9.8 vol% $H_2SO_4$. A DC power supply (Tenma) was used to control the applied voltage for anodization. The positive terminal was connected to the $AlSi_{10}Mg$ specimen (anode) with a wire and alligator clip. The cathode was a piece of SS304L plate with dimensions of 2.5 cm × 1.7 cm and a 0.1 cm thickness. The electrodes were placed parallel at a fixed distance of 5.7 cm using a clamp secured to a ring stand. Anodization was performed in a 400 mL beaker filled with 9.8 vol.% $H_2SO_4$. The electrodes were lowered into the bath such that approximately 1.9 cm (about 3/4 of the sample height) of each was immersed. The anodizing process began at 0 V ramping to 15 V at a rate of 5 V/min in 1 V steps. After the 3-min ramp, the voltage was held at 15 V for 20 min. These parameters were selected based on prior work anodizing wrought AA2024-T3 to produce an oxide weight of ~1000 mg/ft$^2$.[31] The anodized specimen was removed from the beaker and rinsed with ultrapure water. To fully remove slowly dissolving anodization smut, the specimen was immersed in ultrapure water for at least 20 min with periodic agitation. Finally, the specimen was then dried with a stream of $N_2$ and stored in a covered petri dish in the lab atmosphere for at least 24 h before further testing.

The oxide weight after anodization was determined by an acid stripping method, as described in ASTM B137 (measurement of coating mass per unit area on anodically coated aluminum). The specimen was weighed using an analytical balance (± 10 μg) before and after stripping using a solution of chromic acid anhydride (20 g/L) and orthophosphoric acid (35 mL/L) that was heated to 100 °C. The anodized specimen was immersed in the solution for 5 min, rinsed in ultrapure water, dried with $N_2$, and weighed. The acid dissolution was repeated until the mass loss was negligible (< 10 μg). The weight loss (mg) is attributed to the dissolution of $Al_2O_3$ oxide layer. The oxide weight per unit area is reported in $mg/ft^2$.

### *Scanning Electron Microscopy and Energy Dispersive X-ray Spectroscopy*

A JEOL 7500F scanning electron microscope was used to image the anodized specimens. The XZ surface was imaged using an accelerating voltage of 1 kV in the gentle beam (GB) mode. A cross section of an anodized specimen was prepared by cutting the specimen and hot mounting in conductive resin. The mounted specimen was abraded and polished down with 0.3 μm alumina powder and then ultrasonically cleaned in ultrapure water for 20 min. Following this, tint etching in Weck’s reagent (4 wt.% $KMnO_4$ + 1 wt.% NaOH) was applied for 30 s. For general imaging, an accelerating voltage between 2 – 5 kV, an emission current of 10 μA, and a working distance of 4 mm were used. For energy dispersive x-ray spectroscopy (EDXS) the cross section was analyzed with an accelerating voltage of 10 kV and an emission current of 20 μA for increased signal strength.

### *Electrochemical Properties*

Electrochemical testing was performed using a Gamry Reference 600 potentiostat. Aluminum alloy specimens were mounted in an H-cell (BioLogic, France) by a clamp with a 1 $cm^2$ O-ring used to define the working electrode surface area exposed to the electrolyte solution. A platinum mesh served as the counter electrode and home-made Ag/AgCl (4 M KCl internal solution) was the reference electrode. Naturally aerated 0.5 M $Na_2SO_4$ + 0.01 M NaCl was used as the electrolyte solution, and all measurements were performed under natural aeration conditions at room temperature. The suite of electrochemical measurements started with an open circuit potential (OCP) vs. time recording. After the OCP measurement, three specimens of each type were used for the electrochemical impedance spectroscopy (EIS) and linear polarization resistance ($R_p$) measurements. $R_p$ measurements were made from a positive-going potential sweep starting at −10 mV vs. OCP and scanning to +10 mV vs. OCP at 1 mV/s. The reciprocal of the slope of the linear i-E curve fit was used to calculate $R_p$. Some specimens were subjected to potentiodynamic polarization measurements from the OCP to a positive limit of 0.50 V, or higher. Other specimens were polarized from the OCP to a negative limit of −1.2 V. Separate specimens were used for the anodic and cathodic polarization measurements (N = 3 anodic and N = 3 cathodic each). Tafel analysis of the anodic and cathodic polarization curves were used to extract the kinetic parameters ($\beta$ and $j_{corr}$) for the anodic and cathodic reactions on the anodized alloy relative to the unanodized control. The Tafel slopes, $\beta_a$ and $\beta_c$ were determined by linear approximation between $30 < |E_{corr}| < 100$ mV. The intersection of the anodic and cathodic tangent lines was used to estimate the corrosion current density, $j_{corr}$.

## 5.4 Results

### *AlSi$_{10}$Mg Microstructure Prior to Anodization*

Rapid melting and particle fusion in the SLM process leads to a nonequilibrium microstructure. Studies of the SLM AlSi$_{10}$Mg microstructure have been reported in the literature.[7,10] The SEM micrograph in Figure 5.1 serves as a representative example for the microstructure of the unanodized specimens used in this work. Many small α-Al dendritic cells are encapsulated in a fine network of Si crystals. The Al grain size is smaller in the center of the melt pool (MP fine) and larger at the edges (MP coarse) because of the large thermal gradients and different cooling rates. The oblong Al grains are 1 – 3 μm in the elongated dimension. As each additional powder layer is fused to the previous layer, the Si network at the surface of the build is recrystallized in the heat affected zone (HAZ). Note that the HAZ has a disruption of the cellular Si structure and larger crystals in the Si phase. This is an area reported to have higher galvanic activity and a greater vulnerability to corrosion initiation.[8]

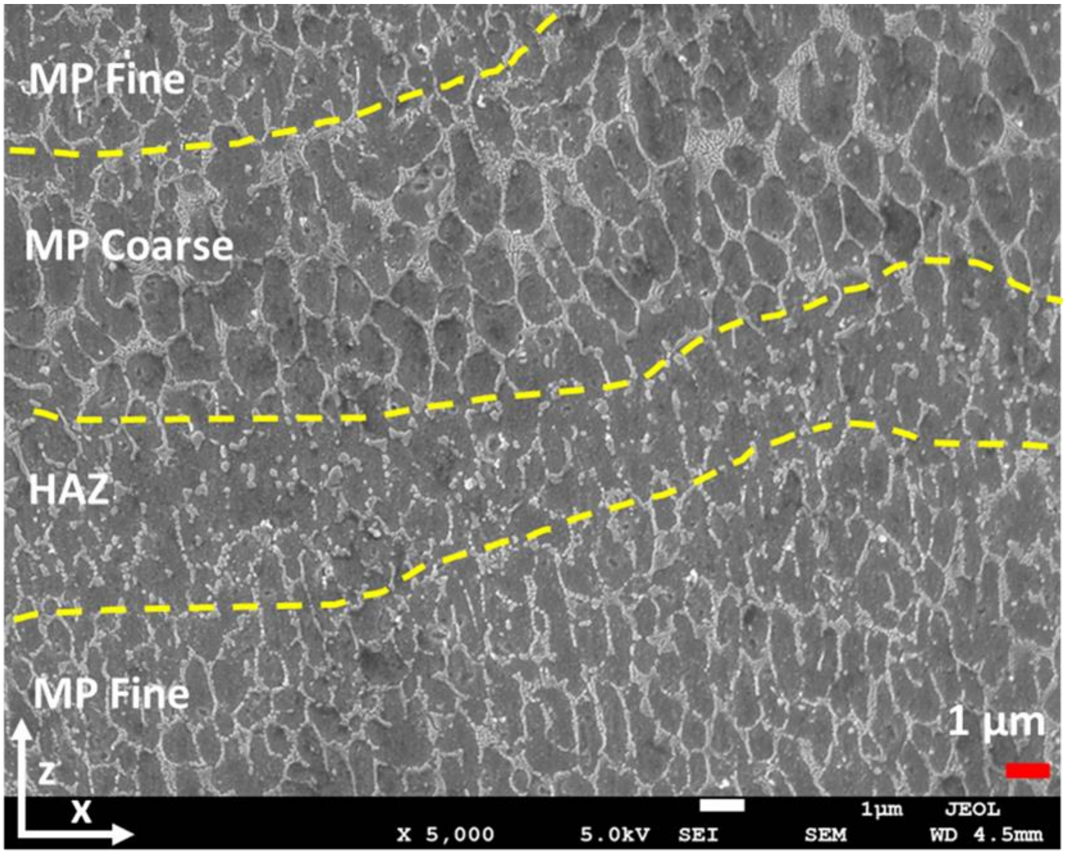

**Figure 5.1.** Unanodized $AlSi_{10}Mg$ specimen after abrading, polishing, degreasing, deoxidation, and wet etching with Weck's reagent for 30 s. The build direction, Z, is shown vertically. The micrograph shows the XZ plane orthogonal to the build direction. Abbreviations- MP (melt pool), and HAZ (heat affected zone).

*Type II Sulfuric Acid Anodization Process*

Three surface pretreated $AlSi_{10}Mg$ alloy specimens were anodized with the current measured at different time points during the potentiostatic process. The current density was calculated by dividing the measured current by the geometric area of the specimen immersed in solution including the edges and rear face. The results are shown in Figure 5.2. The current density increases proportionally to the voltage during the ramp phase. The maximum current density is achieved at the beginning of the hold phase at 15 V of between 12 and 15 mA/cm$^2$.

The current then declines over the next 3 min, trending toward a more constant value of 6 – 7 mA/cm$^2$ for the duration of the anodization. During the ramp, the proportional increase in current density is because of the higher rate of oxidation with increasing voltage. Once the hold begins at 3 min, the current decreases because of the maturing surface coverage and increasing thickness of the oxide. Finally, at times beyond 10 min, the near steady-state current of 6 – 7 mA/cm$^2$ reflects a constant rate of oxide growth.

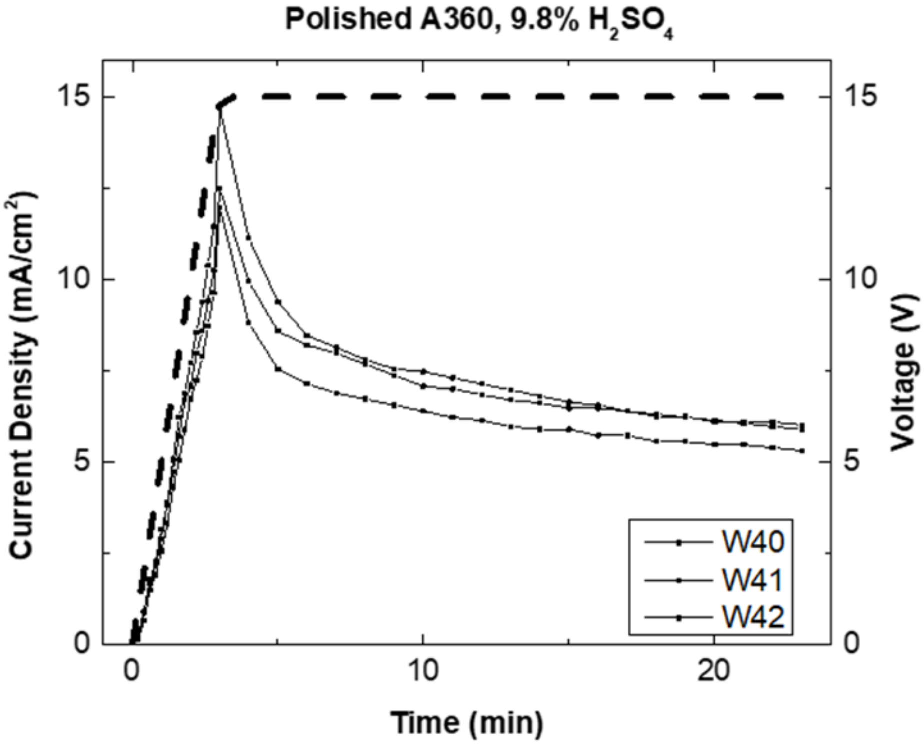

**Figure 5.2.** Measured current-time profiles for three abraded, polished, degreased, and deoxidized AlSi$_{10}$Mg alloy specimens during the sulfuric acid anodization. Current data are shown on the left y-axis and the applied voltage profile versus time is shown on the right y-axis. The anodization was performed in 9.8 vol.% $H_2SO_4$ at 15 V with an initial 3 min voltage ramp at 5 V/min.

The electrochemical formation of aluminum oxide is shown in this redox reaction:

$$2\mathrm{Al_s} + 3\mathrm{H_2O} \rightarrow \mathrm{Al_2O_{3(s)}} + 6\mathrm{H^+_{(aq)}} + 6\mathrm{e^-} \tag{17}$$

The equation indicates 1 mol of oxide is produced for every 6 mol of electrons passed. The theoretical mass of oxide ($m_{ox}$) formed can be estimated from the total charge (Q) passed using Faraday's law in Eq. (2)

$$m_{\mathrm{ox}} = \frac{Q\mathrm{M_{ox}}\eta}{nF} \tag{18}$$

In this equation, $M_{ox}$ is the molar mass of $Al_2O_3$ (102 g/mol), n is the number of electrons to produce one mole of oxide (6), and F is the Faraday constant (96,500 C/mol). To account for other electrochemical reactions, the faradaic efficiency (η) is included in the calculation. A value of $\eta = 0.6$ is commonly assumed, based on previous work by Wu[18] and Veys-Renaux[17]. Dividing the oxide mass by the anodized surface area yields an oxide weight of 918 ± 42 $mg/ft^2$ (mean ± standard error of the mean) for multiple specimens (n = 3). The oxide weight, as measured by the chemical stripping method, was a little lower at 698 ± 29 $mg/ft^2$. The discrepancy between the two values suggests a lower faradaic efficiency than the assumed $\eta = 0.6$ value. If the oxide weight from ASTM B137 is used in Eq. (2), the calculated faradaic efficiency is $\eta = 0.46 \pm 0.03$. The lower η can be explained by some charge being passed for the oxidation of Si to $SiO_2$, which has been reported by Revilla and coworkers.[27] To summarize their work, SLM and the diecast $AlSi_{10}Mg$ alloys were anodized galvanostatically in 9.8 % $H_2SO_4$ followed by characterization using XPS depth profiling. For the SLM prepared alloy, the XPS profiling revealed that $SiO_2$ was present throughout the oxide. In contrast, the die cast alloy contained no subsurface Si oxide. The oxidation of Si in the SLM prepared alloy lowered the faradaic efficiency and is attributed to the fine crystal size of the Si network.

### *Scanning Electron Microscopy - Energy Dispersive X-ray Spectroscopy*

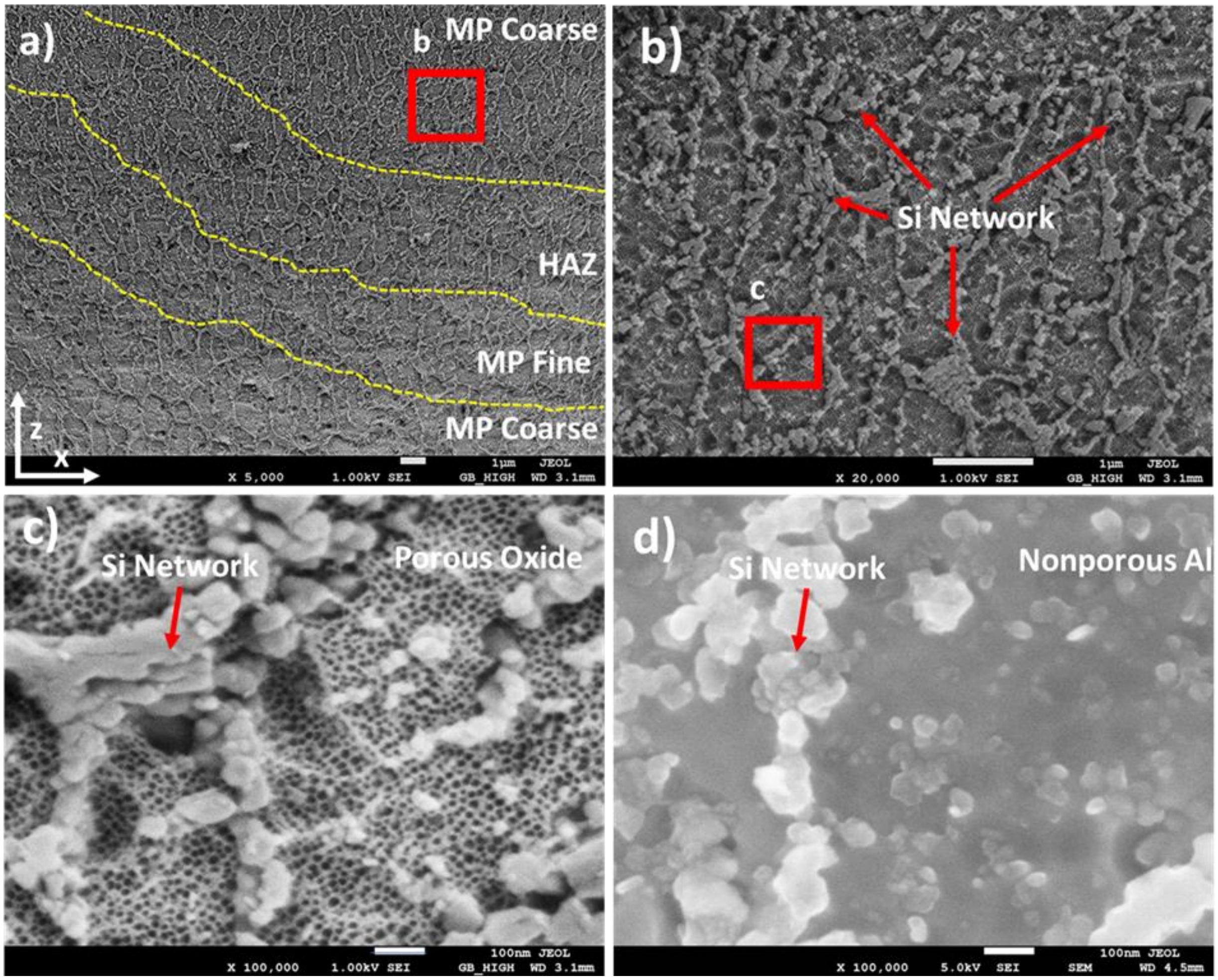

**Figure 5.3.** Scanning electron micrographs of anodized $AlSi_{10}Mg$ (XZ plane) a) at 5000× and higher magnification insets at b) 20,000×, showing the Si network in greater detail and c) 100,000×, showing the porous Al oxide morphology. A micrograph of an unanodized specimen is shown in d) 100,000× for comparison to the porous oxide in c). The anodization was performed in 9.8 vol.% $H_2SO_4$ at 15 V for 23 min with an initial 3 min voltage ramp at 5 V/min.

**Figure 5.3 (cont'd)**

Micrographs shown are secondary electron images. Abbreviations- MP (melt pool), and HAZ (heat affected zone).

SEM micrographs of an anodized specimen taken in the gentle beam (GB) mode are presented in Figure 5.3. In Figure 5.3a, the anodized surface is viewed at the same magnification as in Figure 5.1 for comparison. The Si network and grain structure resembles that of the fine and coarse melt pool regions and the HAZ region in between the sintered layers (yellow dashed lines). A higher magnification micrograph of the red boxed area is shown in Figure 5.3b. On the surface, the Si phase network remains intact within the coarse melt pool region. Closer investigation of the Si/Al structure in Figure 5.3c reveals the porous oxide grown over Al grains that are separated by the Si phase. A uniform oxide pore diameter of ~20 nm is seen. In some places, the Si phase remains intact, but in other places it looks to be oxidatively damaged. This damage is apparent when comparing the anodized surface to the unanodized surface shown in Figure 5.3d. The Al phase in Figure 5.3d is nonporous and is similarly lined by the Si network. However, in some areas where the aluminum is in contact with the Si phase, there are larger defects that extend below the anodized surface in Figure 5.3c, so-called microvoids. This is a notable feature, as large voids along the Si phase would allow for electrolyte solution penetration during anodization (i.e., contact area increase at the Al/Si interface).

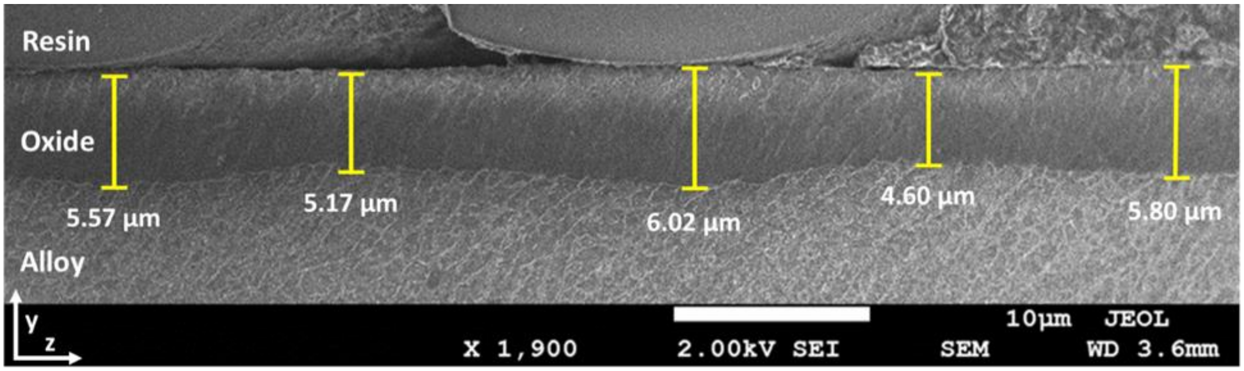

**Figure 5.4.** Secondary electron micrograph of a cross section of an anodized $AlSi_{10}Mg$ specimen showing the continuity and thickness of the oxide layer. The build direction follows the positive z-axis. Oxide thickness measurements shown in yellow were determined using ImageJ software. The anodization was performed in 9.8 vol.% $H_2SO_4$ at 15 V for 23 min with an initial 3 min voltage ramp at 5 V/min.

A SEM micrograph of a cross section of an anodized $AlSi_{10}Mg$ specimen is shown in Figure 5.4. The oxide thickness is indicated by the yellow bars, which values of 4.5 to 6.0 µm over the region probed. The mean ± standard error of the oxide layer thickness is 5.4 ± 0.3 µm (average ± standard error of the mean). Although there is some variation in the oxide thickness, the oxide layer appears continuous across the alloy surface. This indicates that there is good physical and chemical contact between the oxide and the underlying aluminum, and thus effective corrosion protection.

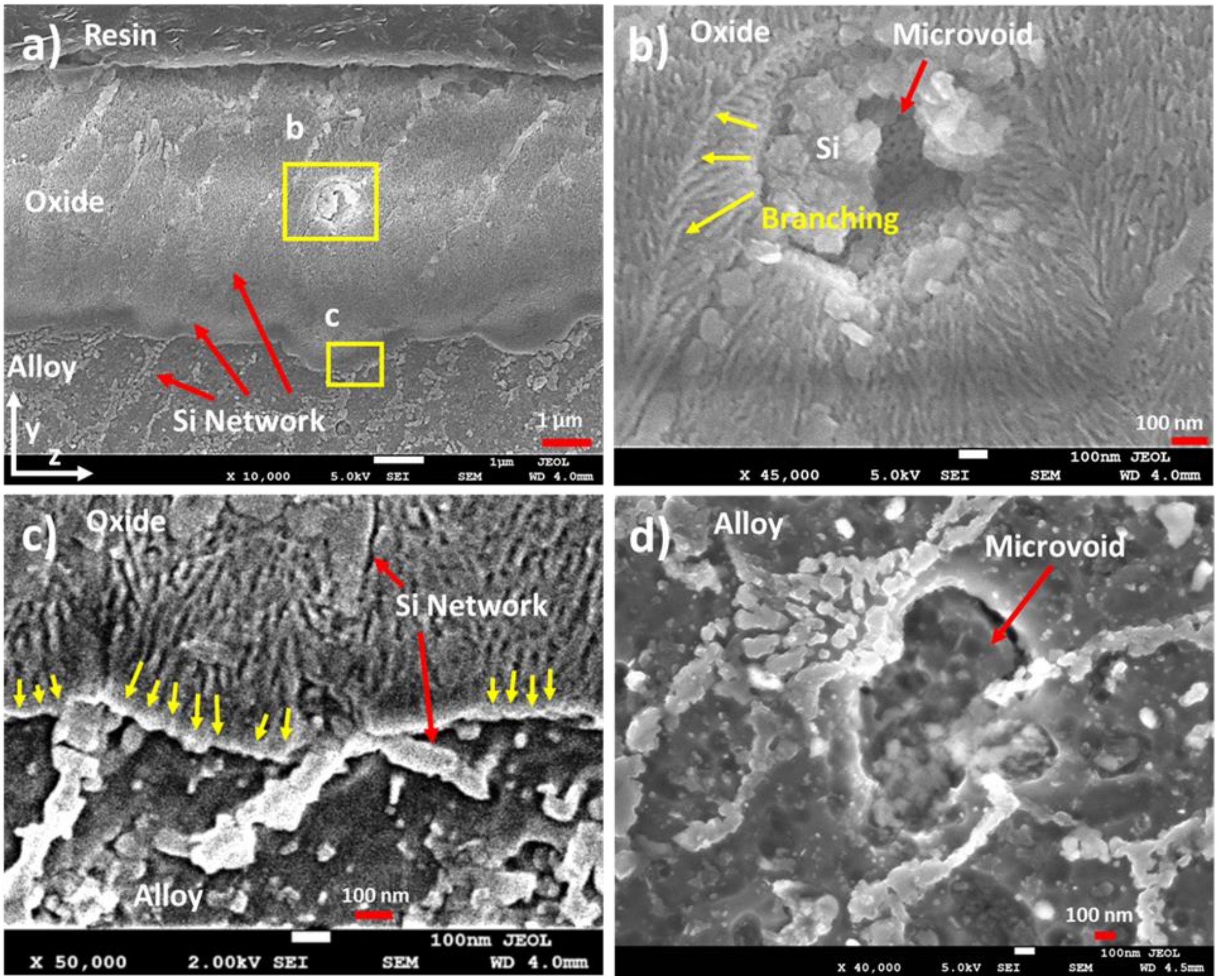

**Figure 5.5.** Secondary electron micrographs of the $AlSi_{10}Mg$ cross section showing the a) oxide layer, b) isolated pore defect in the oxide coating, and c) oxide/alloy interface. d) micro void found in cross section within the alloy bulk. Accelerating voltage and magnification are a) 5 kV and 10,000×; b) 5 kV and 45,000×; and c) 2 kV and 50,000×, d) 5 kV and 40,000×. The anodization was performed in 9.8 vol.% $H_2SO_4$ at 15V for 23 min with an initial 3 min voltage ramp at 5 V/min.

The micrograph in Figure 5.5a shows that large sections of the Si network remain intact through the growing oxide. Near the top of the micrograph, the resin/oxide boundary represents the outer surface of the anodic coating. The anodization of Al does not damage the Si phase, at least in many regions, as the oxide grows downward, thickening with anodization time. An isolated defect in the oxide layer is depicted in greater detail in Figure 5.5b, labeled herein as a microvoid. This is a defect that results from the entrapment of moisture or gas during the fabrication process. Weingarten reports these internal porosity artifacts et al. as hydrogen porosity[32] and are an area of interest in the field of AM.[33] This fabrication defect in the $AlSi_{10}Mg$ specimens used herein and were not often observed. One microvoid was found in the oxide layer (Figure 5.5b), and another in the alloy (Figure 5.5d) for comparison. This gives insight into how the oxide layer formation behaves around fabrication defects. Along the top edge of the microvoid, the aluminum oxide pores branch out horizontally, then turn downward. This was observed previously by Revilla et al. in a study of porosity artifacts in the SLM alloy.[28] The pores grow perpendicular to the walls of the void because the porous oxide layer allows for electrolyte solution penetration into the micro void, filling it. Once the electrolyte contacts the unanodized bottom and sides of the void, the oxide layer grows perpendicular to the interface. Finally, as the entire surface of the void becomes oxidized, the anodizing front (oxide/metal interface) passes below the microvoid, and anodizing continues downward into the alloy. The oxide/metal interface is shown in greater detail in Figure 5.5c. The yellow arrows show the orientation of the pores are not perfectly vertical as would be seen for a cast alloy (i.e. Revilla et al.).[26] In contrast, the observed oxide/metal interface is not uniform in depth, but rather jagged at the high magnification. This can be explained by the tortuous path that the aluminum oxide pores must take through the Si network.

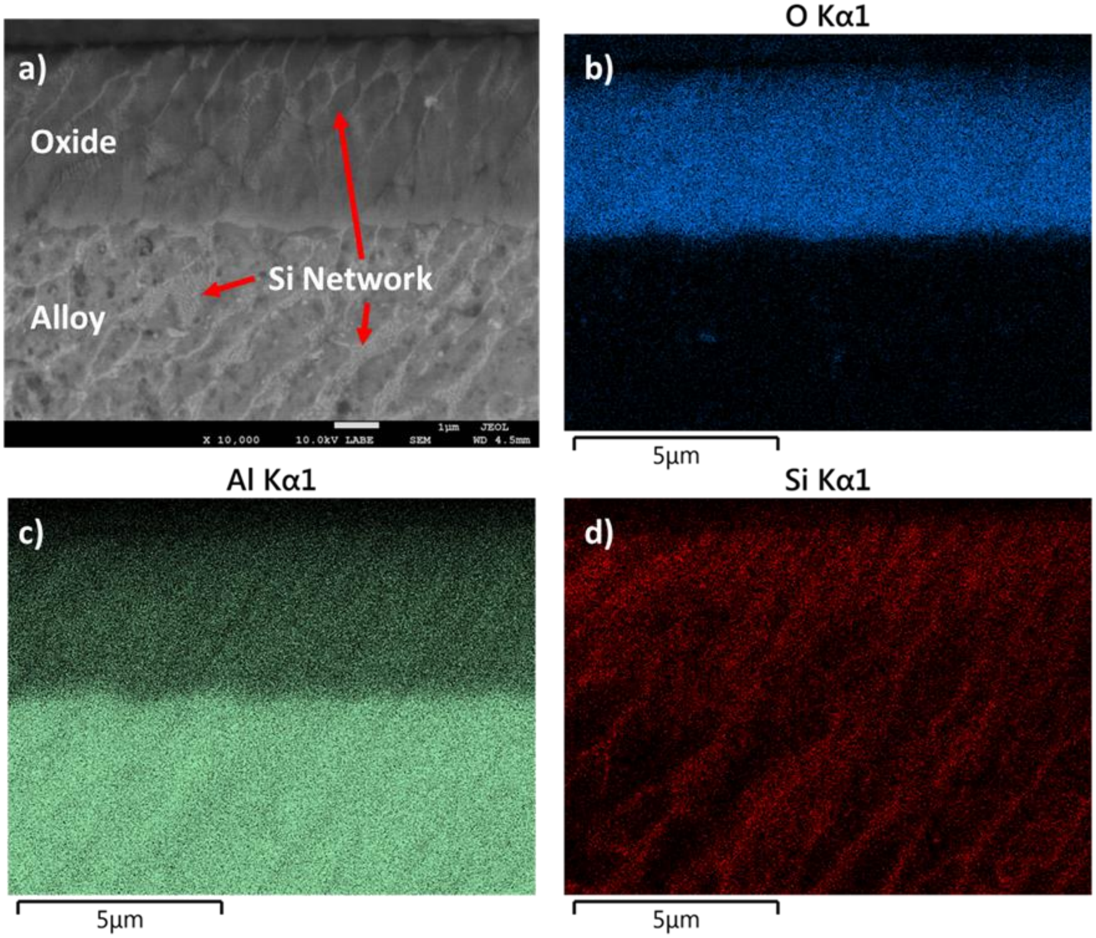

**Figure 5.6.** a) Scanning electron micrographs (backscatter electron mode) of a cross section of an anodized $AlSi_{10}Mg$ specimen at 10,000× magnification. EDXS elemental maps of b) O Kα1, c) Al Kα1, and d) Si Kα1 X-ray intensities in the cross-sectional electron micrograph in a). Accelerating voltage = 10 kV. The anodization was performed in 9.8 vol.% $H_2SO_4$ at 15 V with initial 3 min voltage ramp at 5 V/min.

The backscatter electron micrograph in Figure 5.6a was analyzed using EDXS mapping. Elemental maps for O, Al and Si are depicted in Figure 5.6b-d. The maps provide insight on the location of different elements in the cross section. The O Kα1 intensity dominates the top half of the map where the oxide coating resides. Based on the scale bar and the presence of O, the oxide layer is roughly 5 μm thick. The Al Kα1 signal is present in both the top and bottom halves of Figure 5.6c. The signal for Al is lower in the oxide than in the bulk alloy as expected given the lower density of the former. Likewise, the Si Kα1 intensity is present throughout the fully mapped area, and follows the bright network seen in Figure 5.6a. Results (not presented here) also revealed S, from $SO_4^{-2}$, present throughout the oxide. The element was certainly present in the outer oxide, but the spatial resolution was insufficient to confirm the presence near or within the barrier layer. It has been reported that the barrier region, of relatively pure amorphous anodic alumina, does not contain sulphate ions that are incorporated at the pore base and are subsequently inwardly mobile under the electric field.[34] This is explained by the greater inward mobility of $O_2^-$ ions relative to $SO_4^{-2}$ ions under the field during anodizing. From the microscopy data at hand, we can tell that the oxide coating is ca. 5 μm thick for these anodization conditions, but we cannot determine the thickness of the all-important barrier layer at the base of the oxide coating.

### *Electrochemical Properties*

Various electrochemical measurements were made to investigate the effect of the oxide layer on the electrochemical properties of the $AlSi_{10}Mg$ alloy. The open circuit potential (OCP) vs. time was recorded and example curves are presented in Figure 5.7a. Table 5.1 presents a summary of numerical electrochemical values as determined from replication measurements. The data in Table 5.1 1 reports the stabilized OCP values, which is when the OCP changes by less than ±10 mV over at least 600 s. The nominal value for the anodized specimens is more negative (i.e., more noble) than that for the unanodized specimens by about 150 mV. This trend is reflective of reduced corrosion susceptibility with the anodic coating.

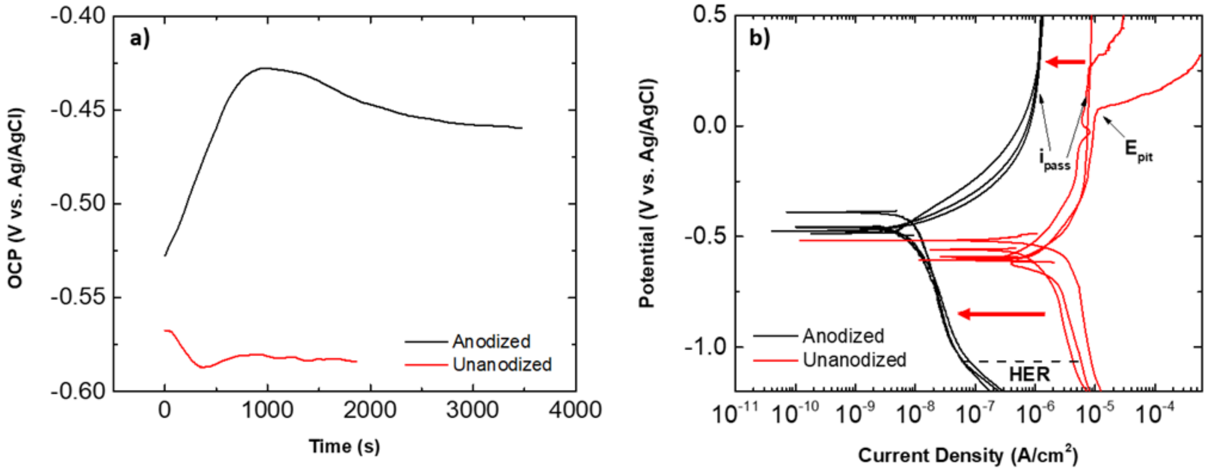

**Figure 5.7.** Data for anodized and unanodized $AlSi_{10}Mg$ specimens in naturally aerated 0.5 M $Na_2SO_4$ + 0.01 M NaCl. a) Open circuit potential (OCP) versus time curve for an anodized and unanodized specimen. b) Potentiodynamic polarization curves are shown for anodized and unanodized specimens (N = 6 anodized and N = 6 unanodized). Potentials below the black dashed line are where the hydrogen evolution reaction (HER) occurs. Red arrows show anodic and cathodic current suppression provided by the anodic coating.

**Table 5.1.** Summary of electrochemical data for anodized and uncoated $AlSi_{10}Mg$ specimens in 0.5 M $Na_2SO_4$ + 0.01 M NaCl. Data are reported as mean ± standard error of the mean. Statistical significance was determined by a two-tailed student's t-test assuming equal variance with $^{**}p < 0.005$.

| | Anodized | Unanodized |
|---|---|---|
| OCP (mV) | −456 ± 14 | −591 ± 8** |
| $E_{pit}$ (mV) | -- | 72, 270 |
| j at −0.1 V (μA/cm²) | 0.469 ± 0.078 | 7.110 ± 0.100** |
| j at −0.8 V (μA/cm²) | −0.026 ± 0.001 | −5.580 ± 1.060** |

Potentiodynamic polarization curves for multiple anodized and unanodized specimens are presented in Figure 5.7b. It is clear from the data that both the anodic and cathodic currents are suppressed by the oxide coating. The anodic current at −0.1 V is suppressed by 15× after anodization while the cathodic current at −0.8 V is suppressed by 215× (see Table 5.1). The data indicate that the oxide coating slows the redox reaction rates for both aluminum oxidation (Eq. 3) and dissolved oxygen reduction (Eq. 4).

$$\mathrm{Al_{(s)}} \rightarrow \mathrm{Al^{3+}_{(aq)}} + 3\mathrm{e^-} \qquad (19)$$

In the anodic polarization curves for the anodized specimens, there is no onset of localized oxide breakdown and stable pit formation and growth out to 0.5 V for any of the specimens, consistent with the oxide coating passivating the underlying surface. Beyond −0.1 V, the specimens exhibit a passivation current density, $j_{pass}$, of ca. 10 μA/cm$^2$. The passivation current density is about 15× lower after anodization (see Table 5.1). While no breakdown was observed on any of the anodized specimens, two of the three unanodized specimens showed signs of native oxide layer breakdown. At high anodic potentials, the chloride-containing electrolyte causes the breakdown of the native oxide layer on aluminum. The breakdown occurs locally, and the active Al oxidizes rapidly forming highly active pits. The pitting potential ($E_{pit}$) marks the potential at which the current increases significantly above the passivation current reflecting stable pit formation. One unanodized specimen exhibited no evidence for stable pit formation out to 0.5 V vs. Ag/AgCl. One specimen, however, exhibited Epit at 72 mV and another at 270 mV. This difference from specimen to specimen is attributed to different integrities of the natural passivating oxide layer on the specimen surfaces.

The oxygen reduction reaction (ORR) is assumed to be the primary cathodic reaction in naturally aerated electrolyte at potentials from the OCP down to −1.1 V vs. Ag/AgCl. The oxygen reduction reaction is shown in Eq. 4.

$$\mathrm{O_2 + 2H_2O + 4e^- \rightarrow 4OH^-} \tag{20}$$

Evidence that this current is due to the diffusion-limited reduction of dissolved oxygen is the attenuation in the current seen with the solution is deaerated. The cathodic scan begins at the OCP and extends out to −1.2 V vs. Ag/AgCl. The current density near the OCP is two orders of magnitude lower for the anodized specimens, as compared to the unanodized control. Table 5.1 reveals the cathodic current density at −0.8 V is 215× lower for the anodized specimens. The current for both specimens, but particularly for the anodized ones, increases negative of −1.1 V vs. Ag/AgCl due to the onset of the hydrogen evolution reaction (HER).

$$\mathrm{2H_2O + 2e^- \rightarrow H_2 + 2OH^-} \tag{21}$$

**Table 5.2.** Summary of the polarization resistance ($R_p$) values obtained from linear polarization curves for anodized and unanodized $AlSi_{10}Mg$ specimens. Note that $R_p$ is measured in $M\Omega \cdot cm^2$ for the anodized and $k\Omega \cdot cm^2$ for the unanodized specimens. Statistically significant differences were determined using the two-sample one-tail student's t-test with a confidence interval of $^{**}p < 0.005$. $R^2$ values for the i-E plots from which the $R_p$ values were calculated are also presented.

| | Anodized | | Unanodized | |
|---|---|---|---|---|
| Sample | $R_p$ ($M\Omega \cdot cm^2$) | $R^2$ | $R_p$ ($k\Omega \cdot cm^2$) | $R^2$ |
| 1 | 2.51 | 0.962 | 12.9 | 0.903 |
| 2 | 2.80 | 0.924 | 6.68 | 0.917 |
| 3 | 3.91 | 0.828 | 2.79 | 0.876 |
| Average ± SEM | 3.07 ± 0.43 | | 9.99 ± 2.69** | |

Table 5.2 summarizes linear polarization resistance ($R_p$) values for anodized and unanodized specimens. $R_p$ increases nominally to 3.07 (± 0.43) $\times 10^6$ $\Omega\cdot cm^2$ after anodization from 9.99 (± 2.69) $\times 10^3$ $\Omega\cdot cm^2$. This is an increase of 279× and reflects increased corrosion resistance provided by the oxide coating. The most significant effect of the oxide layer is on suppression of the oxygen reduction reaction current based on the polarization curve data in Figure 5.7. The 279× increase in $R_p$ after anodization is therefore largely attributed to inhibition of the cathodic reaction.

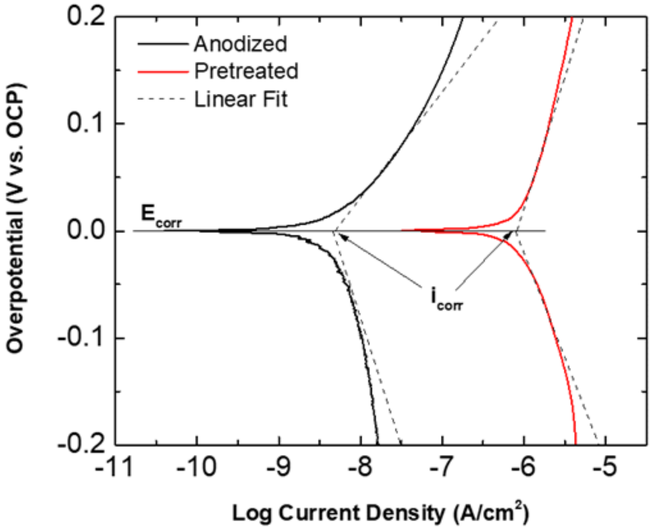

**Figure 5.8.** Tafel plots of anodic and cathodic polarization curve currents plotted as η vs. log j for representative anodized and unanodized specimens. Dashed black lines signify the linear fit for the specimens. The measurements were made in naturally aerated 0.5 M $Na_2SO_4$ + 0.01 M NaCl.

Tafel analysis was performed on the potentiodynamic polarization curve data to determine how the Tafel slopes, β (mV/decade of current, reaction mechanism), and corrosion current density, $j_{corr}$ (A/cm$^2$, measure of the corrosion rate) are affected by the oxide coating.

Tafel plot extrapolation was used to extract the $j_{corr}$ and corrosion potential, $E_{corr}$, values. No iR correction was applied to the $\eta$ – log j data. The assumption is that a single cathodic reaction is occurring, namely the reduction of dissolved oxygen.

Table 5.3 presents a summary of the analysis for anodized and unanodized specimens (n=3 of each). Nominally, the Tafel slope is a little lower for the anodic curves and a little higher for the cathodic curves after anodization. The anodization does not significantly alter the over potential-current relationships for the anodic and cathodic reactions. Therefore, the mechanisms for the two reactions are not changed by the oxide coating. However, the oxide coating does significantly decrease the currents for both reactions with the nominal $j_{corr}$ value 133× lower than for the unanodized control specimens. This effectively means a two order of magnitude reduction in the corrosion rate at $E_{corr}$. This decrease in $j_{corr}$ is consistent with the average suppression of the anodic and cathodic potentiodynamic polarization curves (Table 5.1) of 115× and the nominal increase in the $R_p$ value of 279×.

**Table 5.3.** Tafel analysis of the anodic and cathodic potentiodynamic polarization curves. Anodic and cathodic Tafel slopes ($\beta_a$ and $\beta_c$, respectively) were determined from the line of best fit between $|\eta| = 30$ to 100 mV. The $R^2$ value is reported for each line of best fit. The corrosion current density, $j_{corr}$, was determined from the crossing point of the extrapolated Tafel curves at $\eta = 0$. Statistical significance was determined by a one-tailed student's t-test assuming equal variance with $^*p < 0.01$ and $^{**}p < 0.005$.

| | Anodized | | | | Unanodized | | | |
|---|---|---|---|---|---|---|---|---|
| Sample # | $\beta_a$ (mV/dec) | $\beta_c$ (mV/dec) | $j_{corr}$ (μA/cm²) | $R^2$ | $\beta_a$ (mV/dec) | $\beta_c$ (mV/dec) | $j_{corr}$ (μA/cm²) | $R^2$ |
| 1 | 99 | -- | $4.87 \times 10^{-3}$ | 0.993 | 171 | -- | 0.515 | 0.988 |
| 2 | 103 | -- | $3.41 \times 10^{-3}$ | 0.993 | 170 | -- | 0.785 | 0.987 |
| 3 | 182 | -- | $4.33 \times 10^{-3}$ | 0.998 | 245 | -- | 0.546 | 0.982 |
| 4 | -- | −321 | $5.94 \times 10^{-3}$ | 0.953 | -- | −225 | 0.613 | 0.995 |
| 5 | -- | −223 | $3.88 \times 10^{-3}$ | 0.962 | -- | −195 | 0.316 | 0.988 |
| 6 | -- | −241 | $4.60 \times 10^{-3}$ | 0.925 | -- | −197 | 0.820 | 0.993 |
| Average ± SEM | 128 ± 27 | −262 ± 30 | $(4.50 \pm 0.37) \times 10^{-3}$ | | 196 ± 25* | −206 ± 10* | 0.599 ± 0.076** | |

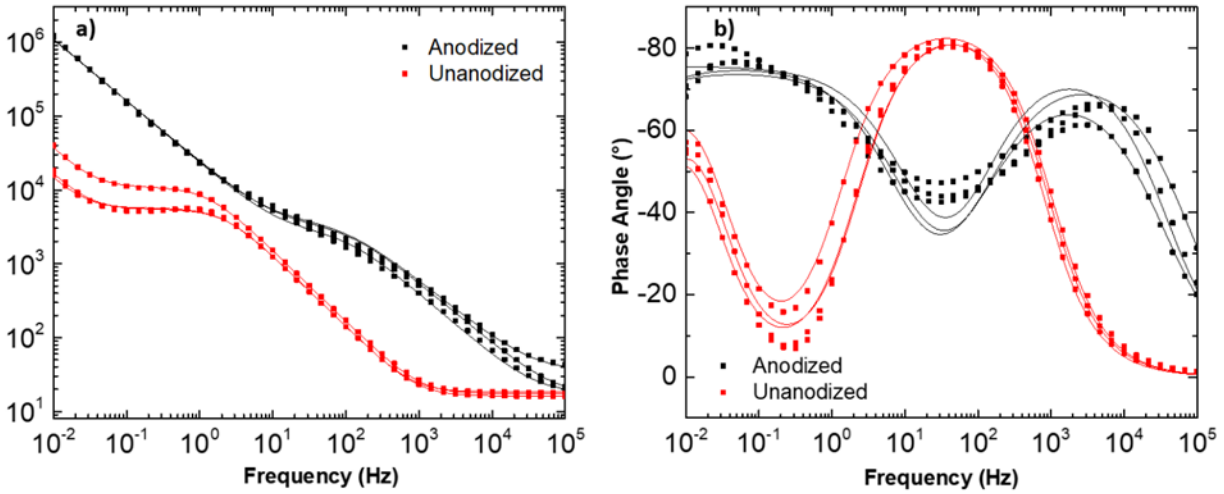

**Figure 5.9.** Bode plots of the total impedance and phase shift versus log frequency for anodized and unanodized AlSi10Mg specimens in naturally aerated 0.5 M $Na_2SO_4$ + 0.01 M NaCl. Measurements were made at the OCP vs Ag/AgCl.

EIS results for multiple anodized and unanodized specimens in 0.5 M $Na_2SO_4$ + 0.01 M NaCl are presented as Bode plots in Figure 5.9. The impedance modulus for both specimen types in Figure 5.9a progressively increases from right to left with decreasing frequency. The plot shows a near straight line and phase angle (Figure 5.9b) approaching −80 degrees for the anodized specimens over the frequency range. This is consistent with the capacitive behavior and barrier properties of the oxide coating.[17,20,31] At the highest frequencies, the impedance is dominated by the equivalent series resistance ($R_{electrode}$ + $R_{solution}$ + $R_{contact}$). Similar values are seen for both specimen types of 10-50 $\Omega$-$cm^2$, as expected. For the anodized specimens, there is a significant increase in the low frequency impedance at $Z_{0.01\ Hz}$ with a value of ca. $10^6$ $\Omega \cdot cm^2$. A value of $10^9$ $\Omega \cdot cm^2$ would be reflective of excellent corrosion protection. The $10^6$ Ω·cm2 value reflects a good level of corrosion protection that could be further improved by sealing. Furthermore, the $10^6$ $\Omega \cdot cm^2$ value is 43× larger than the values of 10-30 $k\Omega \cdot cm^2$ for the unanodized control specimens. The increased $Z_{0.01\ \text{Hz}}$ values are attributed to the suppression of faradaic reactions by the barrier layer formed at the base of the oxide coating. The unanodized specimens begin with a low impedance in the high frequency regime. The impedance starts to increase at frequencies below $10^3$ Hz. At about 1 Hz, the unanodized specimens exhibit a plateau in impedance around $10^4$ $\Omega\cdot\text{cm}^2$. At $10^{-2}$ Hz, the impedance rises to a final value 28.3 ± 7.0 $\text{k}\Omega\cdot\text{cm}^2$. The capacitive behavior, or phase angle shift, is shown in Figure 5.9b. The anodized specimens have peaks in the phase angle at $10^4$ Hz (high frequency) and around $10^{-1}$ Hz (low frequency). The high frequency peak represents the capacitive charging and resistance of species moving through the outer porous oxide coating.[17,23] The low frequency loop represents the interfacial barrier layer charging and resistance to polarization.[17,23] The unanodized surface also has two capacitive peaks, at characteristically different frequencies. The anodized specimens behave more like a capacitor over much of the frequency range as indicated by the high phase angle approaching −80 degrees.

## 5.5 Discussion

Anodizing is an electrochemical process in which the aluminum surface serves as the anode of an electrolytic cell and the growth of Al oxide on the metal substrate is artificially induced through the action of an electrical current.[34] During the oxide growth process, the aluminum anode is continuously consumed and the oxide front advances into the substrate, forming new oxide at the metal/oxide interface. The growth of the anodic coating, in terms of the integrity and morphology, is controlled by the microstructure of the substrate.[34]

The growth mechanism of the aluminum anodic oxide coating has been described in the literature and is reviewed by Scampone et al..[35] The formation of the porous oxide coating during the anodizing process occurs in the following stages[18]: (i) aluminum cations ($Al^{+3}$) are formed from the Al substrate at the anode ($2Al \rightarrow 2Al^{+3} + 6e^{-}$) and $H_2$ is generated at the cathode ($6H^{+} + 6e^{-} \rightarrow 3H_2$); (ii) under the influence of a high electric field, aluminum cations migrate toward the cathode (−), while the anions contained in the aqueous solution ($O^{2-}$, $OH^{-}$, and $SO4^{-2}$ anions) move in the opposite direction toward the aluminum-oxide interface (+) where they react with $Al^{+3}$ cations to form aluminum oxide ($Al_2O_3$, see Eq. 1 above); and (3) at the oxide/electrolyte interface, the aluminum oxide can also dissolve in the electrolyte allowing the formation of a porous structure $Al_2O_3 + 6H^{+} \rightarrow 2Al^{+3} + 3H_2O$).. In summary, the corrosion resistance provided by an anodic coating is strongly affected by the selection of the anodizing parameters and the microstructure of the base alloy, as well as treatments performed before and after anodizing.[16,17,19,25,29,34] Pretreatment of the alloy will have a significant impact on the oxide coating during the early stages when the coating forms non-uniformly, especially on a microstructurally heterogeneous alloy like $AlSi_{10}Mg$. In the case of additively manufactured $AlSi_{10}Mg$, the role of the microstructure and the effect of different surface pretreatments have not been comprehensively investigated. Therefore, the research results presented herein are important and address this knowledge gap.

Compared with pure aluminum and wrought aluminum alloys, die cast and 3D printed alloys are more challenging to anodize. This is because the high content of alloying elements and secondary phases prevents uniform growth of the oxide layer.[34] In areas free of second-phase particles, a regular porous anodic coating is formed. Inclusions, intermetallic compounds, precipitates, and other insoluble alloying elements that are incoherent with aluminum microstructure are not anodized.[34,36] Instead, the primary oxidation reaction proceeds around them, embedding them up in the anodic oxide. The oxide coating will be discontinuous and nonuniform near these solid non-Al phases, like Si in $AlSi_{10}Mg$. As shown in Figure 5.3, the alloy consists of an Al matrix surrounded by a course Si particle network. The higher Si amounts with respect to wrought Al alloys lead to the formation of a large volume of Al–Si eutectic structure, which prevents the uniform growth of the anodic layer during the anodizing process,[28−30] Eutectic Si particles have a slower oxidation rate than the surrounding matrix and promote the preferential growth of the oxide front in the α-Al phase.[26,27] The microstructure of the substrate and the anodizing parameters play a key role in the final thickness, morphology and uniformity of the oxide layer. It has been reported that reduced corrosion resistance is observed in surfaces parallel to the build direction (the XZ direction was studied in our work herein) attributed to the higher density of melt pool boarders containing a higher concentration of course Si particles.[5,7] The native passivating oxide is expected to be defective and inhomogeneous at the interface of the Al and Si particles. The same is expected for the anodic oxide coating. The Si phase is more cathodic than the nearby Al matrix leading to a driving force for galvanic corrosion. These sites of imperfection in the oxide coating are sites for corrosion initiation.

The potentiostatic anodization of SLM $AlSi_{10}Mg$ was successfully performed in 9.8 vol% $H_2SO_4$. Reproducible current-time curve shapes were recorded from specimen to specimen during the SA anodization. The current initially surges at the beginning of the 15 V hold and then decreases as the barrier layer is formed. The subsequent current decay and approach to a steady-state value is reflective of a constant rate of the porous outer oxide growth. Using a chemical stripping method, the oxide weight per area was found to be 698 ± 29 $mg/ft^2$. Based on the measurement of the charge passed during the anodization, the Faradaic efficiency was estimated to be η = 0.46 ± 0.03. Lower efficiency is expected due to some fraction of the charge passed going toward oxygen evolution and surface oxidation of the Si eutectic phase to $SiO_2$, consistent with Revilla's finding in galvanostatic anodization of $AlSi_{10}Mg$.[26,27] Our prior work anodizing wrought alloy AA2024-T3 revealed a nominal the oxide weight of 1200 $mg/ft^2$ for the same anodization conditions.[31]

SLM $AlSi_{10}Mg$ has a distinct microstructure due to the rapid heating and fusion that occurs during the fabrication process. The very fine grains of α-Al are surrounded by a eutectic mixture of Al and Si precipitates.[37] The intercellular network is disrupted by a coarsening Si phase that surrounds the Al cells. As such, the expectation is that the oxide will form into the Al cells with some discontinuity at the Al-Si interface. Some surface oxidation of the Si to $SiO_2$ occurs.

High magnification micrographs in Figure 5.5 reveal nanopores in the aluminum oxide coating. Revilla et al. studied the galvanostatic anodization of SLM $AlSi_{10}Mg$.[26,27] Our work and that of Revilla et al. both show the Si network remains largely intact at the oxide interface and through the oxide coating. The cross-sectional micrographs presented in Figure 5.4 are consistent with those reported by Revilla et al. That is, the SLM $AlSi_{10}Mg$ anodized coating is nominally 5 µm using the anodization conditions employed and has a slightly variable thickness due to the effect of the melt pool boundaries.[27]

One of the issues with anodizing $AlSi_{10}Mg$ is the oxide coating defects and flaws that are likely to result near the interface of the aluminum and the solid Si phase. The integrity of the oxide near the Si phase is discontinuous and are locations for solution penetration and attack of the underlying metal. The electrochemical tests give insight into the robustness of the anodic oxide coating. The electrochemical properties indicate the alloy is passivated by the oxide coating, even with the discontinuous nature across the surface. The polarization resistance, $R_p$, is 279× larger for the anodized as compared to the unanodized specimens in the 0.5 M $Na_2SO_4$ + 0.01 M NaCl electrolyte. Further evidence for the passivation is the negative shift in the OCP, the suppressed anodic and cathodic currents in potentiodynamic polarization curves (average of 115×), and the 133× decrease in the $j_{corr}$ values obtained from Tafel analysis. The anodization suppresses the cathodic more than anodic current. The anodic oxide coating exhibited no signs of breakdown and localized pitting in the supporting electrolyte out to 0.5 V vs. Ag/AgCl. We did not investigate the effect of different chloride concentrations (only 0.01 M) on the localized pitting of anodized AlSi10Mg, but the relationship between the chloride concentration and pit growth kinetics of Al-Si alloys has been studied by Rehim et al.[38] To summarize, a greater chloride concentration increased the rate of pit nucleation. Additionally, electrolytes with a low chloride concentration required a higher applied potential to break down the passive film. Cabrini et al. studied the effect of chloride exposure on SLM AlSi10Mg with anodic polarization experiments.[8] The conclusions showed the same effect, with $E_{pit}$ shifting more noble with lower chloride concentration on polished specimens.

There is no literature describing direct comparison of unanodized and anodized $AlSi_{10}Mg$ fabricated by 3D printing. One study of a cast Al-Si alloy was reported by Li et al. for anodizing in a Type II electrolyte.[24] Potentiodynamic testing in 3.5% NaCl lead to $i_{corr}$ = 0.07 μA/cm$^2$ for Type II anodized versus 0.24 μA/cm$^2$ for the unanodized alloy for a 3× decrease by the added protection of the oxide layer.[24] In their work, no breakdown was observed for the anodized surface in the potentiodynamic test with an anodic limit of 0.75 V vs. SCE. It can be that the pitting potential for the anodized samples is beyond the upper limit of the anodic polarization test. For further work on anodized $AlSi_{10}Mg$, the authors suggest that a higher chloride concentration be used for studying passive film breakdown. Tafel analysis of the anodic and cathodic polarization curves from the present work are presented in Table 5.3. The corrosion current density $j_{corr}$ is 133× lower for the anodized as compared to the unanodized alloy. Since the anodic and cathodic Tafel slopes were the same for the anodized and unanodized specimens, it is concluded that the major influence of the oxide coating is to decrease the exchange current for both the anodic and cathodic reactions by reducing the electrochemically active area.

EIS results presented in Figure 5.9 for the anodized and unanodized $AlSi_{10}Mg$ specimens reveal that the anodic oxide coating increases the low frequency impedance, $Z_{0.01\ Hz}$ by 43× to ca. $10^6$ Ω-cm2. The impedance modulus is similar to what was observed for unsealed AA2024-T3 anodized using the same conditions and in the same supporting electrolyte.[31] The increase in $Z_{0.01\ Hz}$ reflects improved barrier properties and passivation of the alloy by the oxide coating. The anodized specimens exhibit a phase angle approaching −80 degrees over a wide frequency range reflective of the capacitive behavior of the oxide coating.

## 5.6 Conclusions

Potentiostatic anodization of SLM $AlSi_{10}Mg$ was successfully carried out in a sulfuric acid electrolyte. The anodic coating forms into the Al cells in the alloy and is defective near the Si phase particles that surround the Al cells. The anodic coating improves the barrier properties of the alloy and increases the corrosion resistance based on electrochemical measurements in naturally aerated 0.5 M $Na_2SO_4$ + 0.01 M NaCl. The key findings of this research are as follows:

1. Anodization in 9.8 wt.% sulfuric acid at 15 V for a total of 23 min produced an oxide coating weight of 698 ± 29 mg/ft$^2$. This is ca. 2× lower than the oxide weight of wrought aluminum alloy 2024-T3 anodized similarly. This is attributed to a lower faradaic efficiency for oxidation on $AlSi_{10}Mg$ due to the presence of Si particles across the surface.
2. The oxide coating is composed of a porous outer layer branching through the Si network with pore diameters of ca. 20 nm. The nominal oxide layer thickness was 5.43 ± 0.25 μm.
3. Electrochemical testing revealed the OCP shifted negative and both anodic and cathodic currents were suppressed by the anodic oxide coating. Anodic currents in potentiodynamic polarization curves at −0.1 V vs. Ag/AgCl were 15× lower and cathodic currents at −0.8 V was 215× lower. The oxide coating has more of an effect of suppressing the cathodic (oxygen reduction) current density.
4. The polarization resistance, $R_p$, determined from linear polarization measurements was 279× larger for the anodized as compared to the unanodized specimens.
5. Tafel analysis of the anodic and cathodic potentiodynamic polarization curves revealed similar Tafel slopes for the anodic and cathodic curves but corrosion current densities, jcorr, 133× lower for the anodized as compared to the unanodized alloy. Since the anodic and cathodic Tafel slopes were the same for the anodized and unanodized specimens, it is concluded that the major influence of the oxide coating is to decrease the exchange current for both the anodic and cathodic reactions by reducing the active area.
6. Impedance spectroscopy revealed the anodic oxide coating increases the low frequency impedance, $Z_{0.01\ Hz}$ by 43× to ca. $10^6$ $\Omega$-cm$^2$. The barrier properties could be improved by sealing.

## 5.7 Acknowledgements

This manuscript has been authored by Honeywell Federal Manufacturing & Technologies; LLC under Contract No. DE-NA-0002839 with the U.S. Department of Energy/National Nuclear Security Administration. The United States Government retains and the publisher, by accepting the article for publication, acknowledges that the United States Government retains a nonexclusive, paid-up, irrevocable, world-wide license to publish or reproduce the published form of this manuscript, or allow others to do so, for United States Government purposes.

# REFERENCES

1. D. Herzog, V. Seyda, E. Wycisk, and C. Emmelmann, Additive Manufacturing of Metals, *Acta Mater.*, **117**, 371–392 (2016).

2. N. T. Aboulkhair, M. Simonelli, L. Parry, I. Ashcroft, C. Tuck, R. Hague, 3D Printing of Aluminium Alloys: Additive Manufacturing of Aluminium Alloys Using Selective Laser Melting, *Prog. Mater. Sci.*, **106**, 100578 (2019).

3. J. H. Martin, B. D. Yahata, J. M. Hundley, J. A. Mayer, T. A. Schaedler, T. M. Pollock, 3D Printing of High-Strength Aluminium Alloys, *Nature*, **549**, 365–369 (2017).

4. L. Hitzler, M. Merkel, W. Hall, and A. Öchsner, Powder-Bed Based Additive Manufacturing Techniques: Process, Nomenclature, Materials, Achievable Properties, and its Utilization in the Medical Sector, *Adv. Eng. Mater.*, **20**, 1700658 (2018).

5. M. Cabrini, S. Lorenzi, T. Pastore, S. Pellegrini, D. Manfredi, P. Fino, S. Biamino, C. Badini, Evaluation of Corrosion Resistance of Al-10Si-Mg Alloy Obtained by Means of Direct Metal Laser Sintering, *J. Mater. Process. Tech.*, **231**, 326–335 (2016).

6. M. Rafieazad, M. Mohammadi, A. Gerlich, and A. Nasiri, Enhancing the Corrosion Properties of Additively Manufactured AlSi10Mg Using Friction Stir Processing, *Corros. Sci.*, **178**, 109073 (2021).

7. P. Fathi, M. Rafieazad, X. Duan, M. Mohammadi, and A. M. Nasiri, On Microstructure and Corrosion Behaviour o AlSi10Mg Alloy with Low Surface Roughness Fabricated by Direct Metal Laser Sintering, *Corros. Sci.*, **157**, 126–145 (2019).

8. M. Cabrini, S. Lorenzi, T. Pastore, C. Testa, D. Manfredi, M. Lorusso, F. Calignano, M. Pavese, F. Andreatta, Corrosion Behavior of AlSi10Mg Alloy Produced by Laser Powder Bed Fusion Under Chloride Exposure, *Corros. Sci.*, **152**, 101–108 (2019).

9. M. Rafieazad, M. Mohammadi, and A. M. Nasiri, On Microstructure and Early Stage Corrosion Performance of Heat Treated Direct Metal Laser Sintered AlSi10Mg, *Addit. Manuf.*, **28**, 107–119 (2019).

10. M. Rafieazad, P. Fathi, M. Mohammadi, and A. Nasiri, Effects of Laser-Powder Bed Fusion Process Parameters on the Microstructure and Corrosion Properties of AlSi10Mg Alloy, *J. Electrochem. Soc.*, **168**, 021505 (2021).

11. P. Fathi, M. Mohammadi, X. Duan, and A. M. Nasiri, Effects of Surface Finishing Procedures on Corrosion Behavior of DMLS-AlSi10Mg_200C Alloy Versus Die-Cast A360.1 Aluminum, *JOM*, **71**, 1748–1759 (2019).

12. R. I. Revilla, C. A. Rybin, and I. De Graeve, On the Zr Electrochemical Conversion of Additively Manufactured AlSi10Mg: The Role of the Microstructure, *J. Electrochem. Soc.*, **168**, 121502 (2021).

13. J. W. Walton, L. Rice, S. McFall-Boegeman, and G. M. Swain, The Electrochemical Behavior of As-Prepared Aluminum Alloy A360 Produced by Selective Laser Melting Fabrication with and without a Trivalent Chromium Process Conversion Coating, *J. Electrochem. Soc.*, **169**, 121501 (2022).

14. Abdel-Gawad, S. A.; Osman, W. M.; Fekry, A. M. Characterization and Corrosion Behavior of Anodized Aluminum Alloys for Military Industries Applications in Artificial Seawater, *Surf. Interfaces*, **14**, 314–323 (2019).

15. Anodic Coatings for Aluminum and Aluminum Alloys, Department of Defense Military Specification: MIL-A-8625F (2003).

16. S. T. Abrahami, J. M. de Kok, H. Terryn, J. M. Mol, Towards Cr(VI)-Free Anodization of Aluminum Alloys for Aerospace Adhesive Bonding Applications: A Review, *Front. Chem. Sci. Eng.* **11**, 465–482 (2017).

17. D. Veys-Renaux, N. Chahboun, and E. Rocca, Anodizing of Multiphase Aluminum Alloys in Sulfuric Acid: In situ Electrochemical Behaviour and Oxide Properties, *Electrochim. Acta*, **211**, 1056–1065 (2016).

18. Z. Wu, C. Richter, and L. Menon, A Study of Anodization Process During Pore Formation in Nanoporous Alumina Templates, *J. Electrochem. Soc.*, **154**, E8-E12 (2007).

19. Y. Zuo, P.-H. Zhao, and J.-M. Zhao, The Influences of Sealing methods on Corrosion Behavior of Anodized Aluminum Alloys in NaCl Solutions, *Surf. Coat. Tech.*, **166**, 237–242 (2003).

20. A. Carangelo, M. Curioni, A. Acquesta, T. Monetta, and F. Bellucci, Application of EIS to In situ Characterization of Hydrothermal Sealing of Anodized Aluminum Alloys: Comparison between Hexavalent Chromium-Based Sealing, Hot Water Sealing and Cerium-Based Sealing, *J. Electrochem. Soc.*, **163**, C619–C626 (2016).

21. J. Yang, Y. Yang, A. Balaskas, and M. Curioni, Development of a Chromium-Free Post-Anodizing Treatment Based on 2-Mercaptobenzothiazole for Corrosion Protection of AA2024T3, *J. Electrochem. Soc.*, **164**, C376–C382 (2017).

22. M. A. Arenas, A. Conde, and J. J. de Damborenea, Effect of Acid Traces on Hydrothermal Sealing of Anodising Layers on 2024 Aluminium Alloy, *Electrochim. Acta*, **55**, 8704–8708 (2010).

23. V. Moutarlier, M. P. Gigandet, B. Normand, and J. Pagetti, EIS Characterisation of Anodic Films Formed on 2024 Aluminium alloy, in Sulphuric Acid Containing Molybdate or Permanganate Species, *Corros. Sci.*, **47**, 937–951 (2005).

24. X. Li, X. Nie, L. Wang, and D. O. Northwood, Corrosion Protection Properties of Anodic Oxide Coatings on an Al-Si Alloy, *Surf. Coat. Tech.*, **200**, 1994–2000 (2005).

25. M. Paz Martínez-Viademonte, S. T. Abrahami, T. Hack, M. Burchardt, and H. Terryn, A Review on Anodizing of Aerospace Aluminum Alloys for Corrosion Protection, *Coatings*, **10**, 1106 (2020).

26. R. I. Revilla, D. Verkens, G. Couturiaux, L. Malet, L. Thijs, S. Godet, I. De Graeve, Galvanostatic Anodizing of Additive Manufactured Al-Si10-Mg Alloy, *J. Electrochem. Soc.*, **164**, C1027–C1034 (2017).

27. R. I. Revilla, H. Terryn, and I. De Graeve, Role of Si in the Anodizing Behavior of Al-Si Alloys; Additive Manufactured and Cast Al-Si10-Mg, *J. Electrochem. Soc.*, **165**, C532–C541 (2018).

28. R. I. Revilla, Y. Rojas, and I. De Graeve, On the Impact of Si Content and Porosity Artifacts on the Anodizing Behavior of Additive Manufactured Al-Si Alloys, *J. Electrochem. Soc.*, **166**, C530–C537 (2019).

29. T. Rubben, R. I. Revilla, and I. De Graeve, Effect of Heat Treatments on the Anodizing Behavior of Additive Manufactured AlSi10Mg, *J. Electrochem. Soc.*, **166**, C42–C48 (2019).

30. R. Revilla, D. Verkens, T. Rubben, and I. De Graeve, Corrosion and Corrosion Protection of Additively Manufactured Aluminium Alloys- A Critical Review, *Materials*, **13**, 4804 (2020).

31. T. K. Shruthi, J. Walton, S. McFall-Boegeman, S. Westre, and G. M. Swain, Investigation of the Trivalent Chromium Process Conversion Coating as a Sealant for Anodized AA2024-T3, *J. Electrochem. Soc.*, **167**, 111504 (2020).

32. C. Weingarten, D. Buchbinder, N. Pirch, W. Meiners, K. Wissenbach, R. Poprawe, Formation and Reduction of Hydrogen Porosity during Selective Laser Melting of AlSi10Mg, *J. Mater. Process. Tech.*, **221**, 112–120 (2015).

33. J. A. Slotwinski, E. J. Garboczi, and K. M. Hebenstreit, *J. Res. Natl. Inst. Stand. Technol.*, **119**, 494 (2014).

34. Fukuda, Y.; Fukushima, T., Behavior of Sulfate Ions during Formation of Anodic Oxide Film on Aluminium, *B. Chem. Soc. Jpn.*, **53**, 3125–3130 (1980).

35. Scampone, G.; Timelli, G. Anodizing Al–Si Foundry Alloys: A Critical Review. *Adv. Eng. Mater.*, **24**, 2101480 (2022).

36. J.M. Runge, L. Chesterfield, The science of successfully anodizing die cast substrates, https://finishingandcoating.com/index.php/anodizing/1415-the -science-of-successfully-anodizing-die-cast-substrats (accessed Jun 23,2023).

37. A. Mertens, J. Delahaye, O. Dedry, B. Vertruyen, J.T. Tchuindjang, A.M. Habraken, Microstructure and Properties of SLM AlSi10Mg: Understanding the Influence of the Local Thermal History, *Procedia Manuf.*, **47**, 1089-1095 (2020).

38. Abdel Rehim, S.S., Hassan, H.H. and Amin, M.A., Chronoamperometric Studies of Pitting Corrosion of Al and (Al-Si) Alloys by Halide Ions in Neutral Sulphate Solutions, *Corros. Sci.*, **46** 1921–1938, (2004).

# CHAPTER 6 – Conclusions and Future Work

## 6.1 Conclusions

Aluminum alloy AA2024-T3 is protected by a TCP coating to protect the underlying metal from corrosion. For conventional TCP coatings, deoxidation pretreatment is critical for the alloy surface activation and proper coating formation.[1] However, there are drawbacks to deoxidation. At longer deoxidation times, pits will form on the metal surface and decreases the corrosion resistance of the TCP-coated metal.[1] In essence, the deoxidation step is precarious. The work reported in Chapter 3 evaluates a possible solution: a new TCP coating that does not require surface deoxidation. The research compared the new TCP coating (TCP-1) to a conventional coating (TCP-2). The difference in the coatings is the surface preparation, where TCP-1 does not require a deoxidation pretreatment prior to coating. In conclusion, the coatings were similar in their formation mechanism, chemistry and morphology, and corrosion behavior. The conclusions of this research highlight that the TCP-1 coating provides excellent corrosion protection. This is a significant finding in the scientific field and holds practical benefits for corrosion protection technologies. This research proves the concept that the deoxidation step can be eliminated by using TCP-1. In practice, TCP-1 offers the benefits of (i) removing a process tank for the deoxidation surface pretreatment, (ii) a reduction in the volume of hazardous waste that must be monitored and disposed of and (iii) a reduction in the overall component processing time.

Advanced manufactured aluminum alloys are a novel interest in the modern age. 3D printing technology, including SLM, has given an increased freedom to create parts with higher complexity and reduced waste. While these are highly desirable for production, the new materials must be rigorously tested before widespread use. One point of concern is the effectiveness of corrosion protection technologies. In Chapter 4 a TCP conversion coating on SLM $AlSi_{10}Mg$ (A360) was studied. The experiments focused on the TCP coating formation and corrosion suppression that it provided to the SLM aluminum alloy. In conclusion, the conversion coating suppresses both the anodic and cathodic reaction kinetics. Additionally, through neutral salt spray testing, TCP-coated specimens reduced the corrosion intensity (g/$m^2$-year) by 10–11×. Furthermore, other corrosion protection technologies must also be evaluated on SLM aluminum alloys. In Chapter 5 the potentiostatic anodization of SLM $AlSi_{10}Mg$ was successfully carried out in a sulfuric acid electrolyte. The anodic coating improves the barrier properties of the alloy and increases the corrosion resistance based on electrochemical measurements. The results of this research show that anodizing SLM $AlSi_{10}Mg$ is highly effective at increasing the corrosion resistance of the alloy. This is a positive message to the scientific community- in this case, the advanced manufactured alloy can be effectively protected by the established corrosion preventative technologies of TCP coating and Type II anodization.

## 6.2 Future Work

As new coating formulas and improved pretreatments are developed, it will always be a necessity to report the findings. TCP coating of SLM $AlSi_{10}Mg$ was successful in providing general corrosion protection to the alloy surface. However, accelerated degradation testing showed that corrosion propagation was possible in isolated areas. It is possible that defects in the coating and the high surface roughness led to poor local formation of the coating. The future work should focus on enhancing the coating surface coverage. Particularly, the work should look at optimizing the pretreatment steps. The anodization of SLM $AlSi_{10}Mg$ has been tested electrochemically and shows outstanding corrosion protection through electrochemical testing.

The next steps of this research are to test the anodic coating through accelerated degradation testing to observe the corrosion failure mechanisms, and to seal the porous oxide using a secondary chemical bath after anodizing.

# REFERENCES

1. L. Li, A. L. Desouza, and G. M. Swain, Effect of Deoxidation Pretreatment on the Corrosion Inhibition Provided by a Trivalent Chromium Process (TCP) Conversion Coating on AA2024-T3, *J. Electrochem. Soc.*, **161**, C246, (2014).